

Lawrence Berkeley National Laboratory

LBL Publications

Title

An international code comparison study on coupled thermal, hydrologic and geomechanical processes of natural gas hydrate-bearing sediments

Permalink

<https://escholarship.org/uc/item/0pz9f20r>

Authors

White, MD

Kneafsey, TJ

Seol, Y

et al.

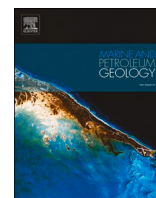
Publication Date

2020-10-01

DOI

10.1016/j.marpetgeo.2020.104566

Peer reviewed



Review article

An international code comparison study on coupled thermal, hydrologic and geomechanical processes of natural gas hydrate-bearing sediments

M.D. White^{a,*}, T.J. Kneafsey^b, Y. Seol^c, W.F. Waite^d, S. Uchida^e, J.S. Lin^f, E.M. Myshakin^c, X. Gai^c, S. Gupta^g, M.T. Reagan^b, A.F. Queiruga^b, S. Kimoto^h, IGHCCS2 Participants

^a Energy and Environment Directorate, Pacific Northwest National Laboratory, Richland, WA, USA

^b Energy Geosciences Division, Lawrence Berkeley National Laboratory, Berkeley, CA, USA

^c Office of Research and Development, National Energy Technology Laboratory, Morgantown, WV, USA

^d U.S. Geological Survey, Woods Hole Coastal and Marine Science Center, Woods Hole, MA, USA

^e Civil and Environmental Engineering, Rensselaer Polytechnic Institute, Troy, NY, USA

^f Civil and Environmental Engineering, University of Pittsburgh, Pittsburgh, PA, USA

^g Marine Geosystems, GEOMAR Helmholtz Center for Ocean Research Kiel, Germany

^h Department of Civil and Earth Resources Engineering, Kyoto University, Kyoto, Japan



ARTICLE INFO

Keywords:

Natural gas hydrates
Numerical simulation
Coupled thermal-hydrological-mechanical (THM) processes
Code comparison
Geomechanics

ABSTRACT

Geologic reservoirs containing gas hydrate occur beneath permafrost environments and within marine continental slope sediments, representing a potentially vast natural gas source. Numerical simulators provide scientists and engineers with tools for understanding how production efficiency depends on the numerous, interdependent (coupled) processes associated with potential production strategies for these gas hydrate reservoirs. Confidence in the modeling and forecasting abilities of these gas hydrate reservoir simulators (GHRs) grows with successful comparisons against laboratory and field test results, but such results are rare, particularly in natural settings. The hydrate community recognized another approach to building confidence in the GHRs: comparing simulation results between independently developed and executed computer codes on structured problems specifically tailored to the interdependent processes relevant for gas hydrate-bearing systems. The United States Department of Energy, National Energy Technology Laboratory, (DOE/NETL), sponsored the first international gas hydrate code comparison study, IGHCCS1, in the early 2000s. IGHCCS1 focused on coupled thermal and hydrologic processes associated with producing gas hydrates from geologic reservoirs via depressurization and thermal stimulation. Subsequently, GHRs have advanced to model more complex production technologies and incorporate geomechanical processes into the existing framework of coupled thermal and hydrologic modeling.

This paper contributes to the validation of these recent GHRs developments by providing results from a second GHRs code comparison study, IGHCCS2, also sponsored by DOE/NETL. IGHCCS2 includes participants from an international collection of universities, research institutes, industry, national laboratories, and national geologic surveys. Study participants developed a series of five benchmark problems principally involving gas hydrate processes with geomechanical components. The five problems range from simple geometries with analytical solutions to a representation of the world's first offshore production test of methane hydrates, which was conducted with the depressurization method off the coast of Japan. To identify strengths and limitations in the various GHRs, study participants submitted solutions for the benchmark problems and discussed differing results via teleconferences. The GHRs evolved over the course of IGHCCS2 as researchers modified their simulators to reflect new insights, lessons learned, and suggested performance enhancements. The five benchmark problems, final sample solutions, and lessons learned that are presented here document the study outcomes and serve as a reference guide for developing and testing gas hydrate reservoir simulators.

* Corresponding author. Staff Engineering, Earth Systems Science Division, P.O. Box 999, MSIN K4-18, Pacific Northwest National Laboratory Richland, WA, 99352, USA.

E-mail address: mark.white@pnnl.gov (M.D. White).

<https://doi.org/10.1016/j.marpetgeo.2020.104566>

Received 24 April 2020; Received in revised form 24 June 2020; Accepted 28 June 2020

Available online 9 July 2020

0264-8172/Published by Elsevier Ltd. This is an open access article under the CC BY-NC-ND license (<http://creativecommons.org/licenses/by-nc-nd/4.0/>).

Nomenclature*Roman Symbols*

a^E	shear/bulk modulus fitting parameter	K_g^H	gas hydraulic conductivity, m/s
A_d	reaction surface area, m ²	K_w^H	water hydraulic conductivity, m/s
A_{rs}	specific reaction surface area, m ² /m ³	L	length, m
c_p	specific heat, J/kg K	\mathcal{L}	time dependent forcing function due to the applied stress, Pa/s
$c_{p,s}$	grain/solid specific heat, J/kg K	m_t	mass of gas hydrate, kg
C	hydrate reaction rate coefficient, 1/Pa s	M	fluid storativity, 1/Pa
C_g	gas compressibility, 1/Pa	M_g	molecular mass of gas, kg/kmol
C_k	material parameter for effective permeability	M_h	molecular mass of gas hydrate, kg/kmol
C_m	compressibility of the bulk porous material, 1/Pa	M_w	molecular mass of water/aqueous, kg/kmol
C_r	reaction parameter, 1/s	n	relative permeability model exponent
C_v	consolidation parameter, m ² /s	\mathbf{n}	unit surface normal vector
C_w	water/aqueous compressibility, 1/Pa	N	exponent for effective permeability
$C_{s,h}$	composite soil-hydrate compressibility, 1/Pa	N_h	hydration number, mol water/mol guest molecule
d	sample height, m	P	pore pressure, Pa
D	diffusion parameter, m ² /s	$P_{analytical}$	pressure from analytical solution, Pa
D_{h0}	proportionality of the elastic stiffness due to hydrate, 1/Pa	P_c	capillary pressure, Pa
D_{hs}	elastic stiffness matrix for hydrate-bearing soil, 1/Pa	$P_{c,o}$	initial capillary pressure, Pa
D_s	elastic stiffness matrix of the host soil (without hydrate), 1/Pa	P_{eq}	hydrate equilibrium pressure, Pa
ΔE_a	activation energy, J/mol	P_g	gas pressure, Pa
$E_1(\xi)$	exponential integral	$P_{g,o}$	initial gas pressure, Pa
f_g	gas fugacity, Pa	$P_{g,out}$	outlet gas pressure, Pa
f_{sh}^k	hydrate saturation component of intrinsic permeability function	P_{init}	initial pressure, Pa
f_{sh}^{Pc}	hydrate saturation component of capillary pressure function	P_{max}	maximum pressure, Pa
f_{ϕ}^{Pc}	porosity component of capillary pressure function	P_o	gas entry pressure, Pa
J_{ϕ}^k	porosity component of intrinsic permeability function	P_w	water/aqueous pressure, Pa
g	acceleration of gravity, m/s ²	$P_{w,o}$	initial water pressure, Pa
\dot{g}_g	volumetric gas generation rate, m ³ gas (methane)/m ³ pore/s	$P_{w,out}$	outlet water pressure, Pa
\dot{g}_h	volumetric hydrate generation rate, m ³ hydrate/m ³ pore/s	Q	mass production rate, kg/s
\dot{g}_w	volumetric water/aqueous generation rate, m ³ aqueous (water)/m ³ pore/s	\dot{Q}_h	heat of hydrate dissociation, W/m ³
G	shear modulus, Pa	Q_s	volumetric injection rate, m ³ /s
G_h	hydrate shear modulus, Pa	r	radius, m
G_o	initial shear modulus, Pa	R	universal gas constant, J/mol K
G_{sh}	composite soil-hydrate shear modulus, Pa	s_g	gas saturation, m ³ gas/m ³ pore
h	height, m	s_g^e	effective gas saturation, m ³ gas/m ³ pore
k	intrinsic permeability, m ²	s_{gr}	residual gas saturation, m ³ gas/m ³ pore
k_g^r	gas relative permeability	s_h	hydrate saturation, m ³ hydrate/m ³ pore
k_{eff}	effective intrinsic permeability, m ²	$s_{h,o}$	initial hydrate saturation, m ³ hydrate/m ³ pore
k_o	initial intrinsic permeability, m ²	s_h^r	is the reference hydrate saturation, m ³ hydrate/m ³ pore
k^r	reaction rate, mol/m ² Pa s	s_w	water/aqueous saturation, m ³ water/m ³ pore
k^T	thermal conductivity, W/m K	s_w^e	effective water/aqueous saturation, m ³ water/m ³ pore
k_{dry}^T	dry thermal conductivity, W/m K	$s_{w,o}$	initial water/aqueous saturation, m ³ water/m ³ pore
k_{gas}^T	gas thermal conductivity, W/m K	s_{wr}	residual water/aqueous saturation, m ³ water/m ³ pore
k_h^T	hydrate thermal conductivity, W/m K	S	storativity, 1/Pa
k_i^T	ice thermal conductivity, W/m K	t	time, s
k_{wet}^T	wet thermal conductivity, W/m K	T	temperature, °C or K
k_w^r	water/aqueous relative permeability	T_{init}	initial temperature, °C or K
K	bulk modulus, Pa	T_o	initial temperature, °C or K
K_d	drained bulk modulus, Pa	T_z	time factor
K_{do}	intrinsic reaction rate constant, mol/m ² Pa s	u	displacement, m
K_o	stress ratio	\mathbf{u}	displacement vector, m
K_o	initial bulk modulus, Pa	$u_{analytical}$	displacement from analytical solution, m
K_s	grain bulk modulus, Pa	u_r	radial displacement, m
K_u	undrained bulk modulus, Pa	$u_{r,r}$	partial derivative of radial displacement with respect to radial distance
K_w	water bulk modulus, Pa	$u_{r,z}$	partial derivative of radial displacement with respect to vertical distance
		u_{θ}	azimuthal displacement, m
		$\mathbf{u}_{,\theta}$	azimuthal component of the displacement vector, m
		$u_{z,r}$	partial derivative of vertical displacement with respect to radial distance
		$u_{z,z}$	partial derivative of vertical displacement with respect to vertical distance

v_g	volumetric gas flux, m/s	ξ	similitude variable, m ² /s
v_{sh}	composite soil-hydrate Poisson ratio	ξ	nondimensional parameter in analytical solution
v_w	volumetric water/aqueous flux, m/s	ρ_g	gas density, kg/m ³
V_g	gas volume, m ³	ρ_h	hydrate density, kg/m ³
V_h	hydrate volume, m ³	ρ_s	grain/solid density, kg/m ³
V_p	pore volume, m ³	ρ_w	water/aqueous density, kg/m ³
V_s	solid volume, m ³	σ'	effective stress, Pa
V_t	total volume, m ³	σ'	effective stress vector, Pa
V_w	water/aqueous volume, m ³	σ_h	horizontal stress, Pa
z	vertical distance, m	σ_h	horizontal effective stress, Pa
<i>Greek Symbols</i>		σ_m	mean stress, Pa
α	Biot's constant	σ_m	mean effective stress, Pa
β_ϕ	pore compressibility, 1/Pa	σ_{mo}	initial mean effective stress, Pa
γ	Kozeny-Carman scaling parameter	σ_o	initial stress, Pa
γ	contribution of hydrate to [fx]	σ_o'	initial effective stress, Pa
γ	stress gradient, Pa/m	σ_0'	initial effective stress tensor, Pa
γ'	effective stress gradient, Pa/m	σ_r'	radial effective stress, Pa
ϵ	elastic strain vector	σ_v	vertical stress, Pa
ϵ_{axi}	axial strain	σ_v'	vertical effective stress, Pa
ϵ_r	radial strain	σ_z'	vertical effective stress, Pa
ϵ_v	volumetric strain	σ_{zz}	vertical stress, Pa
ϵ_θ	azimuthal strain	σ_{zz}'	vertical effective stress, Pa
λ	capillary pressure or relative permeability function exponent	σ_θ'	azimuthal effective stress, Pa
μ	viscosity, Pa·s	ϕ	porosity, m ³ pore/m ³ rock
μ_f	fluid viscosity, Pa·s	ϕ_e	effective or apparent porosity, m ³ pore/m ³ rock
μ_g	gas viscosity, Pa·s	ϕ_o	initial porosity, m ³ pore/m ³ rock
μ_w	water/aqueous viscosity, Pa·s		

1. Introduction

To provide context for the second international gas hydrate code comparison study (IGHCCS2), three introductory sections are given here: 1) a primer on gas hydrate as a potential energy resource; 2) the motivations and challenges for gas hydrate reservoir modeling; 3) the role of code comparison projects in advancing gas hydrate as an energy resource.

1.1. Gas hydrate primer

Natural gas hydrate, or simply “gas hydrate” in this work, is a crystalline solid in which gas molecules, primarily methane, are trapped in individual molecular cages formed by hydrogen-bonded water molecules (Sloan and Koh, 2007). Methane is efficiently stored in gas hydrate, which can release up to ~164–180 vol of methane at standard temperature and pressure per volume of gas hydrate (Kvenvolden, 1993; Ruppel and Kessler, 2017). Methane hydrate is stable at the elevated pressures and low temperatures found in sub-permafrost environments and in submarine continental slope sediments in water depths exceeding ~300 m of water (Kvenvolden, 1993). To extract methane from gas hydrate in nature, solid gas hydrate must first be destabilized, or dissociated, so it breaks down into liquid water and free methane gas that can be mobilized toward a production well. Currently, depressurizing the pore space of gas hydrate-bearing reservoirs is viewed as the most efficient approach for producing methane for use as an energy resource (Boswell and Collett, 2011; Boswell et al., 2014; Max and Johnson, 2019).

Production testing from sub-permafrost gas hydrate systems (Boswell et al., 2017; Dallimore and Collett, 2005; Dallimore et al., 2012; Kurihara et al., 2011) and marine environments (Konno et al., 2017; Li et al., 2018; Yamamoto et al., 2019) has demonstrated the feasibility of extracting natural gas on timescales of days or weeks. For gas hydrate to be a commercially viable energy resource, however, wells

may need to operate reliably for decades (Anderson et al., 2011b; Deepak et al., 2019; Kurihara et al., 2011; Myshakin et al., 2019; Walsh et al., 2009; Wilson et al., 2011) and in the case of marine gas hydrate, overcome costly infrastructure installation and operational challenges (Deepak et al., 2019; Hancock et al., 2019; Walsh et al., 2009).

1.2. Motivations and challenges for gas hydrate reservoir simulators (GHRSS)

Given the large investment required both in time and in capital, assurances are needed that enough methane can be extracted, and production facilities can operate safely, over the reservoir's lifetime. GHRSS help provide these assurances not only by forecasting long-term production rates of gas and water from methane gas hydrate reservoirs, but also by predicting the reservoir's mechanical behavior so design requirements for production systems capable of operating for the projected duration of operations can be established.

Because methane extraction from gas hydrate involves a complex range of coupled physical, chemical and thermal processes, building confidence in modeling predictions is not straightforward. Well productivity hinges on the rate at which methane is extracted and recovered, but even a simplified example demonstrates that recovery rate predictions require modeling a broad suite of coupled processes in which several parameters co-evolve. For example, methane recovery rates depend on how rapidly methane is liberated from gas hydrate (e.g. the dissociation rate), and how easily that liberated gas can migrate through the reservoir to the production well (methane migration depends on the reservoir permeability to gas). Dissociation rate and gas permeability are coupled by several processes, however, meaning that when we follow what is required to calculate dissociation rate or permeability, we find the two parameters depend on each other and cannot be determined independently.

To illustrate this coupling, consider that dissociation can directly improve permeability as solid, immobile gas hydrate in the pore space

breaks down into water and free gas, but these mobile fluids interfere with each other's ability to flow (Stone, 1970). As dissociation progresses, the relative permeabilities for gas and water must both be calculated (Brooks and Corey, 1964; Stone, 1970; van Genuchten, 1980), which requires calculating the evolving pore-space occupancy of each phase as gas hydrate dissociates.

Predicting the gas hydrate dissociation rate requires calculating the heat flow in the system because gas hydrate dissociation is endothermic (Handa, 1986). In the long-term, gas hydrate dissociation rates are typically limited by the rate of heat transfer to the dissociation front (Anderson et al., 2011b), and using the 2013 production test in the Nankai Trough as an example, only ~33% of the heat required for dissociation was provided by sediment and pore water directly at the dissociation front. The rest was supplied by heat transported from warmer portions of the system (Yamamoto et al., 2017). However, the conduction and convection of heat to the dissociation front are controlled, respectively, by thermal conductivity and fluid permeability, both of which vary as the saturations of gas, water, and gas hydrate, and the sediment's intrinsic permeability all evolve over time (e.g., Moridis et al. (2009); Myshakin et al. (2019)). Ultimately, heat transfer in the system couples back to the gas hydrate dissociation rate through conductivity and permeability parameters that also vary as the gas hydrate dissociates. The multiply-coupled nature of the processes occurring when gas is extracted from dissociating gas hydrate makes it challenging not only to develop models based solely on first-principle approaches, but also to validate model outputs against relevant analytic solutions. As an additional challenge, there are currently no data from long-term (year-long or more) field tests with which to compare.

1.3. Role of code comparison studies

IGHCCS1 recognized the significance of modeling phase changes (e.g., the formation and breakdown of gas hydrate and how methane partitions between the free gas and dissolved-phase states) and the movement of heat and fluid through the reservoir system. IGHCCS1 not only provided a forum for discussing strategies for dealing with these coupled processes, but also established a means of cross-validating models against each other using seven benchmark problems of increasing complexity. Geomechanics were not a priority for IGHCCS1, which was focused on observations made on thick, coarse-grained gas hydrate-bearing sands in permafrost environments that were assumed to remain stable during production. From the IGHCCS1 benchmark problems and solutions, discussed by Wilder et al. (2008) and Anderson et al. (2011a); (2011b), it was concluded that methane extraction from gas hydrate was enhanced in warmer (deeper) reservoirs and in reservoirs characterized by higher intrinsic permeabilities.

The deep-water marine environment also hosts relatively warm, high-hydrate saturation reservoirs in sand and/or silt-rich sediment near the base of gas hydrate stability (Boswell et al., 2012; Fujii et al., 2015; Li et al., 2018; Waite et al., 2019), but field programs show that marine gas hydrate-bearing sands are more commonly found in thin layers interbedded with essentially gas hydrate-free, fine-grained sediment (Boswell et al., 2012; Flemings et al., 2017; Fujii et al., 2015; Jang et al., 2019; Ryu et al., 2013). Moreover, reservoir modeling indicates production via depressurization in deep-water systems requires pore pressure drawdowns in excess of 10 MPa (Boswell et al., 2019; Konno et al., 2019; Moridis et al., 2019a; Myshakin et al., 2019). Geomechanics becomes a priority in these systems because when pore pressure is drawn down, the reservoir feels an increased effective stress that tends to consolidate or compact the reservoir and significantly reduce production performance.

For example, after measuring water permeability at the in situ effective stress in gas hydrate-bearing pressure cores from the NGHP-02 expedition offshore India, Yoneda et al. (2019a) dissociated the gas hydrate and increased the effective stress by 10 MPa. This simulates the evolution of near-well sediment through which all subsequent fluid and

gas must flow before being recovered at the well. The increased effective stress compacted the specimen, reducing porosity enough to drive the gas hydrate-free permeability below the initial levels measured even while solid gas hydrate occupied more than 60% of the pore space.

Reservoir compaction and deformation were not considered in IGHCCS1, so generally speaking, increasing gas hydrate dissociation rates with larger pressure drawdowns was predicted to increase the methane extraction rates. In contrast, reservoir modeling in deep-water marine settings suggests operations should instead focus on maximizing the overall methane extraction rate by balancing the pressure drawdown needed to dissociate gas hydrate against the reservoir compaction and permeability loss caused by that pressure drawdown (Boswell et al., 2019; Konno et al., 2019; Li et al., 2018; Myshakin et al., 2019).

As occurs during conventional hydrocarbon recovery (Hancock et al., 2019), sediment deformation during production in gas hydrate reservoirs can also disrupt the sediment fabric, mobilizing both fine-grained sediment and sand (Oyama et al., 2016; Uchida et al., 2019). Fine-grained sediment migration can clog pore throats, reducing permeability and production efficiency beyond the effects of reservoir compaction (Cao et al., 2019; Jung et al., 2012; Valdes and Santamarina, 2007). Sand migration into the production well is also commonly halts production (Hancock et al., 2019; Li et al., 2016). The conventional hydrocarbon industry developed remediation strategies for sediment migration that can be tailored to gas hydrate production (Hancock et al., 2019). Geomechanics-based GHRS informs these strategies by predicting how parameters such as pressure, stress, deformation and flow rate evolve.

Geomechanics-based GHRS can be applied to any circumstance in which gas hydrate is destabilized. As an example, conventional oil reserves are generally buried deeper than gas hydrates, in reservoirs so warm that produced oil can be ~100 °C as it is pumped up through overlying gas hydrates (Briaud and Chaouch, 1997). Heat from produced oil propagates into the hydrate-bearing formation through the well casing, and can dissociate hydrate for several meters around the well in only a few years (Briaud and Chaouch, 1997). As Hadley et al. (2008) describe for a conventional hydrocarbon production site offshore Malaysia, producing warm oil through overlying gas hydrate was predicted to dissociate gas hydrate around the well within days. Reservoir modeling indicated the ensuing sediment fracturing and subsidence would likely buckle the well casing and eventually destabilize the production platform itself, so alternate production strategies were developed for the site. These examples highlight the importance of including geomechanics when forecasting reservoir evolution, but there is a challenge of maintaining confidence in every element of a fully-coupled GHRS.

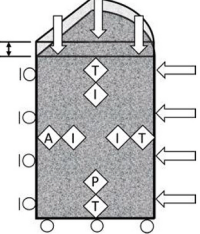
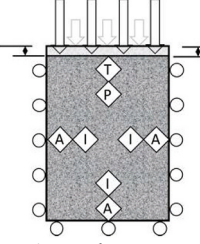
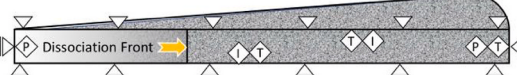
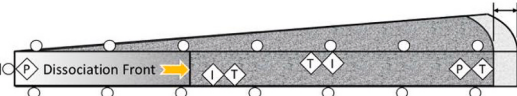
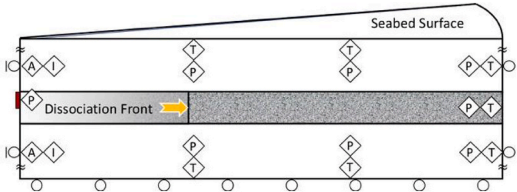
This paper addresses that challenge by presenting the IGHCCS2 benchmark problems and solutions, along with discussions of key modeling issues to manage in order to improve confidence in GHRS results. The benchmark problems are summarized in Table 1. Section 2 introduces the GHRS participating in this study. Section 3 summarizes the study process and outcomes for participants. Sections 4-8 are the benchmark problems themselves. Section 9 provides perspectives and future directions for GHRS development. Full Benchmark Problem descriptions, input parameters and model solutions are available online for others interested in testing their own modeling approaches on NETL's Energy Data Exchange (EDX) as the IGHCCS2 group (<https://edx.netl.doe.gov/group/ighccs2>).

2. Computer codes used in IGHCCS2

The IGHCCS2 brought together research teams from across the globe to verify and advance a variety of reservoir modeling computer codes by comparing simulation results applied to five benchmark problems, as shown in Table 2. In addition to seventeen institutions participating in submissions for at least one of the five benchmark problems, nine other institutions contributed expertise regarding existing data for model

Table 1

Summary of IGHCCS2 Benchmark Problems (BP) with schematic view of each model domain and boundary conditions. Geomechanical boundary conditions are noted with circles to indicate roller boundaries (i.e., zero displacement orthogonal to boundary surface), with circles and triangles with lines to indicate symmetry boundaries, and arrows to indicate imposed stress (i.e., traction boundary). BP3 does not include geomechanics, and is noted with triangles for zero displacement. Flow and transport boundary conditions are noted with lettered diamonds, with T for temperature, A for adiabatic, P for pressure, and I for impermeable.

<p>BP1 (Isotropic Consolidation with Hydrate Dissociation)</p> 	<p>Summary: Vertical consolidation of a single, cylindrical grid cell. Homogeneous system. Case 1 - No hydrate Case 2 - Hydrate without dissociation Case 3 - Hydrate with dissociation</p>
<p>BP2 (Extended Terzaghi Problem)</p> 	<p>Summary: Vertical consolidation and relaxation of a homogeneous system of sediment, water, gas, and hydrate Case 1 - No hydrate kinetics Case 2 - With hydrate kinetics Case 3 - With higher hydrate contribution to sediment strength Case 4 - Very fast hydrate kinetics</p>
<p>BP3 (Gas Hydrate Dissociation in a One-Dimensional Radial Domain)</p> 	<p>Summary: Axial symmetry. Dissociation is in a homogeneous system of sediment, water, gas and hydrate. No geomechanics Case 1 - Thermal Stimulation Case 2 - Depressurization</p>
<p>BP4 (Radial Production with Geomechanics)</p> 	<p>Summary: Axial symmetry. Depressurization in a homogeneous system with geomechanics. Case 1 - Without Hydrate Case 2 - With Hydrate</p>
<p>BP5 (Nankai Trough)</p> 	<p>Summary: Axial symmetry. Coarse-grained hydrate reservoir is isolated between two hydrate-free clay layers. Depressurization occurs only from the top of the hydrate reservoir layer (red block), so flow need not be purely radial.</p>

inputs and the plausibility of certain model results.

The gas hydrate benchmark problems of this study required modeling capabilities that consider coupled processes, known collectively as thermal-hydrologic-mechanical (THM) processes, involving multiple-phase hydraulics, gas hydrate thermodynamics and kinetics, phase appearances and transitions, heat transport and geomechanics. The computer codes utilized in IGHCCS2 were a mix of those developed by the participating institutes, by other institutes, and commercial software. Some were based on research codes initially built without geomechanical modeling capabilities, but now have geomechanics incorporated through a sequential or iterative sequential calculation scheme. For codes in which a commercial geomechanics solver has been incorporated, two common commercial solvers used in the sequential solution scheme mode are FLAC2D and FLAC3D, developed and marketed by Itasca Consulting Group, Inc. In contrast, some IGHCCS2 teams started with geomechanical solvers as the founding code and incorporated gas hydrate processes. This approach often requires converting rudimentary flow and transport solvers into those with multiphase capabilities, and converting from linear to nonlinear systems. Other teams adopted general physics-type computer codes to solve the coupled THM processes for gas hydrate systems. These efforts typically start with a fully coupled solution scheme, but use more simplified models for the gas hydrate thermodynamics and kinetics. The least common type of

code utilized in IGHCCS2 is a fully coupled THM solver specifically built for gas hydrate systems.

The principal features of the participating computer codes are listed in Table 3, which contains code names, websites or references, and descriptions of the numerical schemes for spatial and temporal discretization. Code names are typically acronyms with extensions indicating modifications made to the core code, but can also include institute names or abbreviations. Some of the codes lacked names at the start of the study and others received only descriptive titles. The more mature computer codes have websites with pages on user support, documentation, licensing, discussion forums, example problems, short courses, and licensing (noted in Table 3). For those codes without websites, reference to a published paper is provided in Table 3.

Hydrate reservoir problems generally have space and time dimensions (i.e., states vary over space and time). Numerical simulators are founded on the principle that space and time can be discretized, allowing for the transformation of nonlinear partial differential governing equations into nonlinear algebraic forms, which are solvable via numerical approaches. The most common spatial discretization approaches in Table 3 are the finite volume or integral volume approaches for solving the coupled flow and heat transport equations, and the finite element approach for solving the geomechanical equations. There are variations of this mixed scheme approach, in particular for computer

Table 2

Summary of institutes and teams who submitted solutions to benchmark problems, and/or the indicated computer codes for IGHCCS2. In addition, insight and expertise was provided by modelers, experimentalists and field researchers from the National Institute of Advanced Industrial Science and Technology (AIST), Colorado School of Mines (CSM), Georgia Institute of Technology (GT), Korea Advanced Institute of Science and Technology (KAIST), Oregon State University, Southampton University, Texas A&M University, U.S. Geological Survey, and the University of Tokyo.

Abbreviation	Institute	Teaming	Benchmark Problem Submissions	Computer Code(s)
Cambridge	University of Cambridge	Cambridge-JOGMEC (MH21 Research Consortium)-UCB (noted as UCB on plots)		Berkeley-Cambridge THM model – COMSOL FEM Code
GEOMAR	GEOMAR Helmholtz Center for Ocean Research Kiel	GEOMAR	2, 3	SuGar-TCHM Code for Methane Hydrate Systems
JLU	Jilin University	JLU	2, 3, 4	HydrateBiot
JOGMEC	Japan Oil, Gas and Metals National Corporation	Cambridge-JOGMEC (MH21 Research Consortium)-UCB (noted as UCB on plots)		
KAIST	Korea Advanced Institute of Science and Technology	KAIST		K-Hydrate with FLAC2D/FLAC3D
KIGAM	Korea Institute of Geoscience and Mineral Resources	Ulsan-KIGAM	1, 2, 3, 4, 5	Geo-COUS
Kyoto	Kyoto University	Kyoto	5	COMVI-MH
LBNL	Lawrence Berkeley National Laboratory	LBNL	2, 3, 4, 5	TOUGH + HYDRATE with Millstone
LLNL	Lawrence Livermore National Laboratory	LLNL-Tongji	1, 2, 3, 4, 5	GEOS
NETL	National Energy Technology Laboratory	NETL-Pitt-RPI (noted as NETL on plots)	1, 2, 3, 4, 5	MIX3HRS-GM
Pitt	University of Pittsburgh	NETL-Pitt-RPI (noted as NETL on plots)	1, 2, 3, 4, 5	MIX3HRS-GM
PNNL	Pacific Northwest National Laboratory	PNNL	1, 2, 3, 4	STOMP-HYDT-KE with GeoMech
RPI	Rensselaer Polytechnic Institute	NETL-Pitt-RPI (noted as NETL on plots)	1, 2, 3, 4, 5	MIX3HRS-GM
SNL	Sandia National Laboratories	SNL	3	PFLOTRAN
Southampton	National Oceanography Center Southampton, University of Southampton	Southampton - UPC		CODE_BRIGHT + Hydrate-CASM
TAMU	Texas A&M University	TAMU		CODE_BRIGHT-HYDRATE and T + M (AM)
Tongji	Tongji University	LLNL-Tongji	1, 2, 3, 4, 5	GEOS
UCB	University of California, Berkeley	Cambridge-JOGMEC (MH21 Research Consortium)-UCB (noted as UCB on plots)	1, 2, 3, 4, 5	Berkeley-Cambridge THM model – COMSOL FEM Code
Ulsan	University of Ulsan	Ulsan-KIGAM	1, 2, 3, 4, 5	Geo-COUS
UPC	Universitat Politècnica de Catalunya	Southampton-UPC		CODE_BRIGHT + Hydrate-CASM
UT	University of Texas at Austin	UT	3	UT_HYD

codes that solve flow, transport, and geomechanics in a fully coupled approach for which the finite element method has advantages.

Table 4 contains additional information on the codes used in IGHCCS2 in relation to the coupling of the flow and transport and geomechanics equations, the limits of the geomechanics scheme, the form of the hydrate model, any overall limits or assumptions of the code, and notes on development directions. The flow and transport processes are generally solved via conservation equations, with one equation per component (e.g., water, methane, energy), and the geomechanical processes are solved via quasi-static equilibrium equations for displacements in the three coordinate directions. Some of the computer codes solve these equations in a sequential fashion (i.e., one after another), some in an iterative sequential fashion (i.e., sequentially, but iterating until a joint convergence is achieved), some fully coupled. These coding choices impact execution speed and accuracy (see Table 4, THM Coupling column). Geomechanical processes are complex, involving deformations that may be reversible (i.e., elastic), or irreversible (i.e., creep and plastic). Elastic deformations are solved via linear equations, but creep/plastic deformations require nonlinear solutions (see Table 4, Geomechanics column).

Gas hydrates tend to remain stable unless they experience changes in temperature, pressure or availability of the gas hydrate guest molecules, in which case gas hydrates will form, dissociate, or swap guest molecules to reestablish an equilibrium condition. Gas hydrate growth and decay can be modeled using equilibrium approaches that assume these processes occur rapidly with respect to other flow, transport, or geomechanical processes; alternatively, growth and decay can be modeled via kinetic approaches in which process rates are considered as the system approaches equilibrium conditions over time (see Table 4, Hydrate Model column). All reservoir simulators are built on assumptions, and most are under development to incorporate new capabilities.

Principal assumptions and future directions for the computer codes are listed in Table 4 in the Notes column.

3. Method of code comparison

Code comparison studies are time consuming efforts for all participants, but the benefits often are worth the investments in terms of increasing confidence in simulators and avoiding generating faulty simulation results. In this section we describe the motivations for participating, approaches for comparing codes, expected outcomes from comparing codes, and the communication techniques used in conducting the IGHCCS2.

3.1. Participation motivations

Scientists and engineers write computer codes to solve mathematical problems with complexities that extend beyond those allowed by analytical solutions. Subsurface science problems generally fall within this class of problems because of the inherent heterogeneities, but also because of the number of coupled processes needing to be modeled. Such scientific software is time consuming to write, so for investigations of gas hydrate reservoirs in geologic media, the foundations of such computer codes are generally either more basic subsurface science flow and transport simulators or general physics simulators. There are several advantages to both starting points when developing a new gas hydrate reservoir simulator. Starting with a basic surface science flow and transport simulator usually provides developers with modeling capabilities for heterogeneous domains, reservoir geologic structures, and often the more classical coupled processes, such as hydrologic, thermal and geochemical. More recently, geomechanical modeling capabilities have been incorporated into subsurface science simulators, whereas

Table 3
Computer code basics.

Code Name	Website or Reference	Spatial Discretization	Temporal Discretization
Berkeley-Cambridge THM model – COMSOL FEM Code	A Coupled Thermal-Hydraulic-Mechanical-Chemical Model for Methane Hydrate Bearing Sediments (https://link.springer.com/article/10.1631/jzus.A1700464) and (https://www.researchgate.net/publication/342164833_A_Coupled_Thermal-Hydraulic-Mechanical-Chemical_Model_for_Methane_Hydrate_Bearing_Sediments_Scheme_for_the_THMC_model_Ongoing_research)	Implicit finite element for both geomechanics and flow and transport	Backward differentiation formula high-order integration method
CODE_BRIGHT + Hydrate-CASM	Thermo-Hydro-Mechanical Coupled Model of Methane Hydrate-Bearing Sediments: Formulation and Application, <i>Energies</i> , 2019, 12(11) (https://www.mdpi.com/1996-1073/12/11/2178?type=check_update&version=2) A Densification Mechanism to Model the Mechanical Effect of Methane Hydrates in Sandy Sediments, <i>International Journal for Numerical and Analytical Methods in Geomechanics</i> (2020) (https://onlinelibrary.wiley.com/doi/abs/10.1002/nag.3038)	Finite element method	Finite differences via implicit scheme (backward Euler method) incorporating an automatic sub-stepping procedure based on error control
CODE_BRIGHT-HYDRATE	Coupled Deformation, BRIne, Gas and Heat Transport, <i>Engineering Computations</i> , 1996, 13(7), pp. 87-112	Finite element method	Implicit linear time discretization with two intermediate time points
COMVI-MH	A chemo-thermo-mechanically coupled numerical simulation of the subsurface ground deformations due to methane hydrate dissociation, <i>Computers and Geotechnics</i> , 2007, 34, pp. 216–228.	Finite element method for equation of motion and flow of fluids, finite volume method for heat flow	Newmark's β method
Geo-COUS	Shin, H. (2014). "Development of a Numerical Simulator for Methane-hydrate Production", <i>Journal of the Korean geotechnical society</i> , 30(9), 67-75	Finite-element method	Generalized trapezoidal integration rule
GEOS	For GEOS, see Settgast et al. (2017) For hydrate module, see Ju et al. (2020)	Finite volume method for flow and transport and standard Galerkin finite element for geomechanics with an iterative method, such as Newton's method, to resolve nonlinearities.	Fully implicit time integration of both flow and transport and geomechanics; iterative coupling between flow and geomechanics
HydrateBiot	TOUGH2Biot - A simulator for coupled thermal-hydrodynamic-mechanical processes in subsurface flow systems: Application to CO2 geological storage and geothermal development, <i>Computers and Geosciences</i> , 2015, 77, pp. 8–19.	Integral finite difference method for flow and transport with Newton Raphson to resolve nonlinearities and finite element method for geomechanics	Fully implicit finite-difference scheme
K-Hydrate with FLAC2D/FLAC3D	Methane production from marine gas hydrate deposits in Korea: Thermal-hydraulic-mechanical simulation on production wellbore stability, <i>Journal of Geophysical Research: Solid Earth</i> , 2018, 123, pp. 9555–9569.	Explicit finite difference for geomechanics	
MIX3HRS-GM	Reservoir simulation for production of CH4 from gas hydrate reservoirs using CO2/CO2 + N2 by HydrateResSim. Ph.D. Thesis, West Virginia University, 2013. Novel technological approach to enhance methane recovery from Class 2 hydrate deposits by employing CO2 injection, <i>Energy and Fuels</i> 2018, 32(3), pp. 2949–2961.	Finite volume method for flow simulation and standard Galerkin finite element for geomechanics	Integral finite difference method with Newton-Raphson iteration
PFLOTTRAN	PFLOTTRAN: A Massively Parallel Reactive Flow and Transport Model for describing Subsurface Processes (https://www.pfлотran.org) (Moridis et al., 2019b , Queiruga et al., 2019)	Finite volume for flow and transport and Galerkin finite element for geomechanics, with the finite element nodes located at the cell centers of the finite volume domain.	Fully implicit backward Euler approach based on Newton-Krylov iteration
STOMP-HYDT-KE with GeoMech	STOMP Subsurface Transport Over Multiple Phases (https://stomp.pnnl.gov)	Finite volume method for flow and transport with Newton Raphson to resolve nonlinearities and linear finite element for geomechanics	Backward Euler method
TOUGH+ HYDRATE w/ Millstone	TOUGH: Suite of Simulators for Nonisothermal Multiphase Flow and Transport in Fractured Porous Media (https://tough.lbl.gov)	Integral finite volume method for flow and transport with Newton Raphson to resolve nonlinearities and finite element method for geomechanics with Cartesian or cylindrical (axisymmetric) geometries.	Backward Euler method
SuGaR-TCHM	Implemented with the C++ based DUNE-PDELab framework (https://www.dune-project.org) S. Gupta, Non-isothermal, Multi-phase, Multi-component Flows through Deformable Methane Hydrate Reservoirs, PhD Thesis, Technical University of Munich (2016).	Standard Galerkin finite element method with semi-smooth Newton method for incremental plasticity for geomechanics and fully upwind finite volume method with semi-smooth Newton method for flow and transport	Implicit Euler for flow and reactive-transport model
UT_HYD	Methane hydrate formation in thick sandstones by free gas flow, <i>Journal of Geophysical Research: Solid Earth</i> , 2018, 123, pp. 4582–4600.	Block centered finite difference method for the flow and transport with the option of Eulerian or Lagrangian coordinate systems	Fully implicit

classically they have been standalone simulators for geomechanical and geostructural analyses. General physics simulators may yield the fastest development time for gas hydrate reservoir simulators if the special functions required for modeling the gas hydrate processes are kept simple, such as using an equation with a limited number of parameters to compute the aqueous density versus the steam table formulations, or assuming isothermal conditions. Regardless of the path or starting point, code development, especially on large computer codes (i.e., those with

hundreds of thousands of lines), is subject to errors that could go unnoticed even after years of use on a variety of applications. Additionally, the inclusion of certain process models and the choice of numerical solution schemes can have unintended consequences for simulation results and simulator execution times. Code comparison studies offer a chance to validate and optimize a given modeling approach.

Table 4
Computer code submodels.

Code Name	THM Coupling	Geomechanics	Hydrate Model	Notes
Berkeley-Cambridge THM model – COMSOL FEM Code	Fully coupled solution of flow, thermal, and mechanics	Linear or nonlinear elastoplastic stress/strain law + grid deformation in large-strain mode + optional thermal and pore pressure coupling	Kinetic gas hydrate dissociation and formation	No consideration of salinity and methane concentration effects in the model.
CODE_BRIGHT + Hydrate-CASM	Fully coupled solution scheme	Elasto-plastic critical state model Hydrate-CASM. Densification mechanism approach for hydrate bearing geomechanics	Kinetic dissociation and formation	Densification mechanism approach for hydrate bearing geomechanics
CODE_BRIGHT-HYDRATE	Fully coupled with hydrate saturation dependent sediment behavior		Equilibrium gas hydrate dissociation and formation	Small strains and small strain rates are assumed for solid deformation
COMVI-MH	Fully coupled solution scheme	Elasto-viscoplastic with large deformation	Kinetic dissociation and formation	Dissolution of gas into fluid is not considered. Salinity is not considered.
Geo-COUS	Fully coupled solution at gaussian point level	Thermo-elasto-plastic models for small strain and finite strain	Kinetic dissociation and formation	Ongoing development: fine migration
GEOS	Iterative sequential coupling with fixed stress.	Standard equations of static equilibrium to model solid material deformation and linear elastic fracture mechanics	Equilibrium gas hydrate dissociation and formation	3D only for both geomechanics and flow/transport; Small strain assumption; Hydrate dissociation/formation attains chemical equilibrium instantly
HydrateBiot	Fully coupled flow and transport and partial coupling with geomechanics	Thermo-poro-elastic + small strain assumption	Equilibrium gas hydrate dissociation and formation	
K-Hydrate with FLAC2D/FLAC3D	Sequential solution of flow, thermal, and mechanics	Linear or nonlinear stress/strain law + grid deformation in large-strain mode + optional visco-elastic mode + optional thermal and pore pressure coupling	Kinetic dissociation and formation	No ice, no gas solubility or buoyancy, gas pressure neglected in geomechanics, no initial free gas
MIX3HRS-GM	Fully coupled flow, thermal, chemical and geomechanical processes are solved through sequential coupling solution strategy between flow and geomechanical components.	Multiple geomechanical constitutive models are available for GHBS including simple elastic model, elastic model with stress relaxation concept, perfect elastoplastic model, advanced critical state mechanical model.	Equilibrium/kinetic gas hydrate with ternary gas components (CH ₄ , CO ₂ , and N ₂). dissociation and formation	This simulator consists of a flow component and geomechanical component coupled through a sequential coupling technique. The flow component can simulate hydrates with ternary gas components (CH ₄ , CO ₂ , and N ₂). Sand migration model is being implemented at the time. Open-source and freely available
PFLOTRAN	Sequential coupling with an external code, such as Albany	Thermo-poro-elastic + small strain assumption	Equilibrium gas hydrate dissociation and formation	
STOMP-HYDT-KE with GeoMech	Iterative sequential coupling with fixed stress	Thermo-poro-elastic + small strain assumption	Kinetic dissociation, formation, and guest molecule exchange	No radial coordinates for geomechanics, small strain assumption
TOUGH + HYDRATE with Millstone	Fully implicit finite-difference scheme, with iterative coupling between flow and geomechanics.	Quasi-static approximation of linear momentum with variation form for displacement update, with incremental hydrate-dependent constitutive law	Equilibrium or kinetic dissociation and formation	
SuGar-TCHM	Reactive transport block, geomechanics block, and porosity equation block solved separately, with coupling via iterative block Gauss-Seidel scheme or multi-rate time-stepping	Elasto-plasticity framework; small-strain assumption	Kinetic dissociation, formation, and guest molecule exchange	Soil forms the primary skeleton which undergoes deformations, hydrate only enhances the mechanical properties of the skeleton, virtual porosity evolves due to the deformation of the enhanced skeleton; small strain assumption; kinetic model for hydrate phase change (leads to ill-conditioned system for very fast kinetics); Slow convergence rate of iterative block Gauss-Seidel for poroplastic problem, semi-implicit multirate time-stepping performs better in this case.
UT_HYD	Fully coupled flow and transport, no coupling with geomechanics	No geomechanics	Equilibrium hydrate dissociation and formation with methane hydrate phase boundary calculated from the intersections of the methane hydrate and methane gas solubility curves	No geomechanics; kinetic formation and dissociation is an option

3.2. Code comparison approaches and outcomes

Gas hydrate reservoir simulators can be compared in terms of code structure, numerical solution scheme, accuracy, and execution speed.

The ultimate accuracy comparison is against experimental or field observations, but comparisons against other numerical simulators are also valuable. IGHCCS2 principally considered accuracy in terms of similarity between results from different numerical simulators, using well

defined and constrained problems. Similarity among numerical simulation results does not provide assurance for accuracy against laboratory experiments or field observations, but it does provide confidence that the governing equations and associated constitutive equations are being solved properly. Each problem in this study required solving nonlinear equations for multiple phase systems in geologic media undergoing phase appearances, disappearances, and transitions. The most common nonlinear solution method is to iteratively solve the equations, with a reduction in the equation residuals (i.e., errors) with each iteration.

There was no execution speed comparison during this study. As all of the problems involved time transients, speed could be indicated by the convergence performance between computer codes by comparing the number of time steps required to complete a problem. However, submitting teams had the flexibility and freedom to constrain the time step sizes below that needed for convergence of the nonlinear equations. Because of the sharp stability envelope for gas hydrates, the presence of multiple phases, and the coupled hydrologic, thermal, thermodynamic, and geomechanical processes associated with modeling gas hydrate reservoirs, gas hydrate reservoir simulators generally proceed with smaller time stepping than do their counterpart subsurface flow and transport simulators (e.g., petroleum reservoir simulators, carbon sequestration simulators, geothermal simulators).

Code comparison studies of subsurface flow and transport simulators generally achieve four objectives: 1) creation of benchmark problems and solutions for future code developers, 2) establishment of a topical modeling community, 3) identification and correction of code bugs and 4) correlation of simulator result differences with process models or solution approaches. On occasion, code comparison studies also identify numerical solution schemes that are either impractical or are particularly more effective than conventional approaches. IGHCCS2 did not identify ineffective or outstanding numerical solution schemes, as most of the simulators in the study were either mature codes or used more conventional solution approaches. A number of teams in the study, however, were able to make modifications to their computer codes over the course of the study in response to code bugs, missing capabilities, or to take advantage of novel solution approaches. For example, a simple sign error on a geomechanical boundary condition in one computer code yielded tensile stress, as opposed to the compressive stress required by the problem. Another team realized the necessity of including secondary hydrate formation during the application of the depressurization approach for producing natural gas hydrates. Other code corrections were more subtle, such as the need to re-establish the reference stress state for geomechanics solvers that only consider linear elasticity when the rock elastic properties depend on the hydrate saturation.

For IGHCCS2, five benchmark problems were developed and considered, each with a problem champion. The benchmark problems have been ordered in this paper in order of increasing geometric complexity, starting with a single grid cell, expanding to a vertical array of grid cells, then considering a one-dimensional radial array of nodes, without geomechanical coupling. We then expanded that problem to include geomechanical coupling with and without gas hydrates, and finally conclude with a two-dimensional radial array of nodes. As a class of problems, these benchmark problems were designed to allow for solutions to be generated without the use of high-performance computing (i.e., using serial codes rather than parallelized codes run on supercomputers), with minimal to moderate computational times. The objective of each problem was to test the capabilities of the participating teams and codes against specific coupled processes. Not all participating teams completed all five benchmark problems, either due to time restrictions or limitations in their computer codes. A number of teams described code modifications or corrections that were made to their simulators during the study teleconferences.

3.3. Study communications

The IGHCCS2 study used four communication conduits: 1) the

National Energy Technology Laboratory's (NETL's) Energy Data eXchange (EDX) collaborative, web-based system (<https://edx.netl.doe.gov>), 2) regularly scheduled teleconferences, 3) teleconference recordings, and 4) conventional emails. The EDX system was used as a secured share site to post benchmark problems, submit problem solutions, and store teleconference presentations and recordings. Study participants had access to the study workspace on EDX, but the system was not open to the public. This approach allowed study participants to download and study solutions submitted by other teams, but distribution was limited to the study participants. Teams were free to choose whether to participate in specific problems depending on their reservoir simulator capabilities. Many of the teams submitted multiple solutions, either in response to input errors that were discovered or after making code modifications.

Teleconferences were the most beneficial in terms establishing a gas hydrate reservoir modeling community. The teleconferences were scheduled to allow all of the international participants an opportunity to join, and were recorded for those who could not attend. The teleconference series started with each team providing an overview of their computer code, establishment of benchmark problems and selection of problem champions, review of solution submissions, and finally revision of this manuscript.

4. Benchmark problem 1 – isotropic consolidation with hydrate dissociation

BP1 Champions: Shun Uchida, RPI; Yongkoo Seol, NETL; Jeen-Shang Lin, Pitt; Evgeniy Myshakin, NETL; and Xuerui Gai, NETL.

BP1 entails isotropic consolidation behavior with a focus on the effect of hydrate dissociation on volumetric deformation. The pore pressure depressurization approach to gas production induces isotropic consolidation, leading to volumetric deformation. In addition, the problem setting is intentionally simple to allow more laboratory experiments for isotropic consolidation (e.g., Yoneda et al. (2019a); Yoneda et al. (2019b)) to follow suit in the future. Moreover, we would also highly appreciate triaxial tests with hydrate dissociation to provide additional validation data (e.g., Cao et al. (2019)). BP1 emphasizes the importance of the volumetric deformation-permeability coupling and hydrate dissociation-induced deformation that will occur to some extent during gas production via depressurization.

4.1. BP1 description

This problem considers consolidation of a cylindrical geometry under three conditions: 1) water saturated soil system without gas hydrate, 2) water and hydrate saturated soil system without hydrate dissociation, and 3) water and hydrate saturated soil system with hydrate dissociation. The problem geometry is specifically made simple and the use of a single computational cell is encouraged, as shown in Fig. 1.

4.1.1. Model geometry and boundary conditions

Fig. 2 shows the geometry and boundary conditions of the considered problem. The specimen has a 5 mm radius and 30 mm height. This small size approximates an X-ray CT hydrate testing apparatus by Lei et al. (2018). The computational domain is 2D axisymmetric and only one model element is used. In other words, the model element size is identical to the specimen size. The axis of symmetry can only deform vertically (roller boundary) and is impermeable (no fluid flow) and insulated (no heat transfer). A roller boundary is a mechanical boundary condition that allows for deformation along the line of rollers, but not orthogonal to the line of rollers. The top and cylindrical side boundaries have constant total stress and constant temperature conditions and are impermeable. Because of the constant total stress boundaries, when the pore pressure inside the specimen decreases, the effective stress increases in an isotropic manner, leading to isotropic consolidation. The

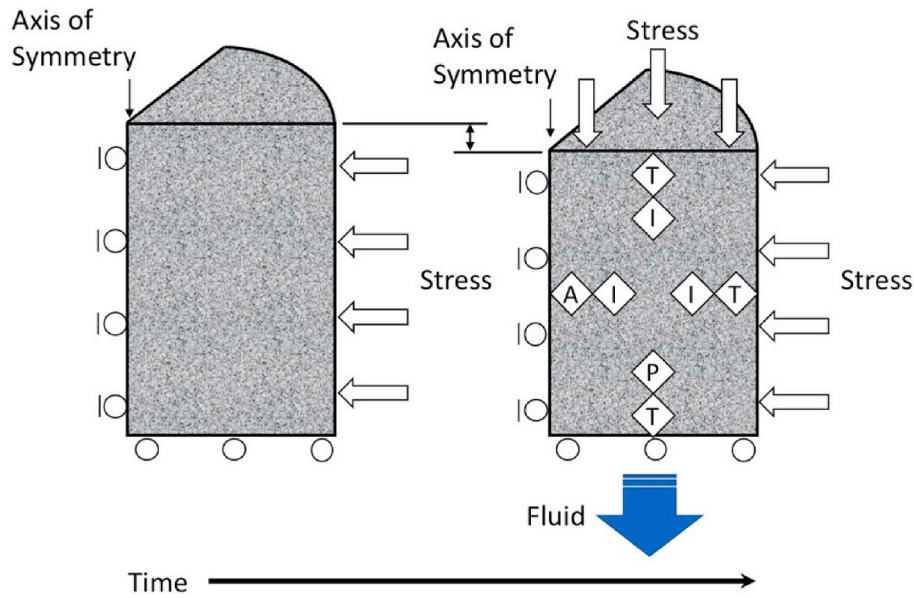


Fig. 1. Conceptual schematic of BP1, with white arrows indicating a stress boundary, circles indicating a roller boundary, T indicating a temperature boundary, P indicating a pressure boundary, I indicating an impermeable boundary, and A indicating an adiabatic boundary. Fluid exits sample base in response to consolidation (blue arrow). (For interpretation of the references to colour in this figure legend, the reader is referred to the Web version of this article.)

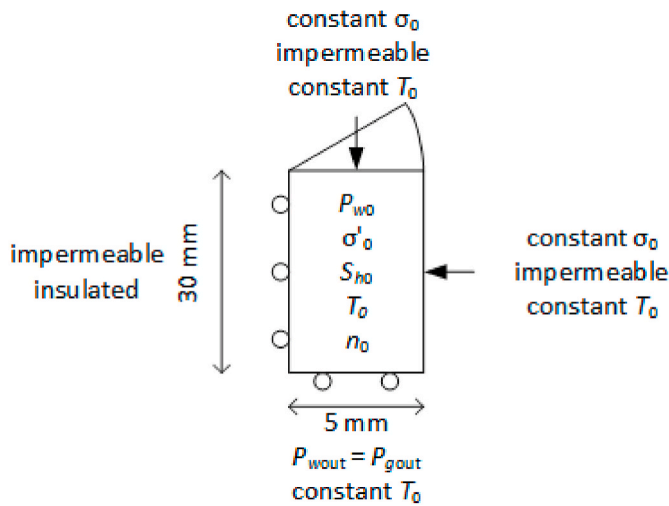


Fig. 2. Model geometry and boundary conditions for BP1.

bottom boundary can only move radially (roller boundary) and has a constant temperature condition. Pore fluid will flow out the bottom surface, driven by the pressure difference between the pore pressure and the bottom boundary pressure, which is maintained at zero capillary pressure (i.e., $P_{w,out} = P_{g,out}$). The value $P_{w,out}$ is reduced from 12 MPa to 4 MPa linearly over a 10 s period and then remains constant thereafter as shown in Fig. 3.

4.1.2. Initial conditions

Table 5 presents the initial conditions for BP1. There is no gas at the initial stage in any of the three cases. The initial effective stress is 1 MPa (isotropic).

- Case 1 – no hydrate
- Case 2 – hydrate without dissociation
- Case 3 – hydrate with dissociation

Note that the initial hydrate saturation, water saturation and

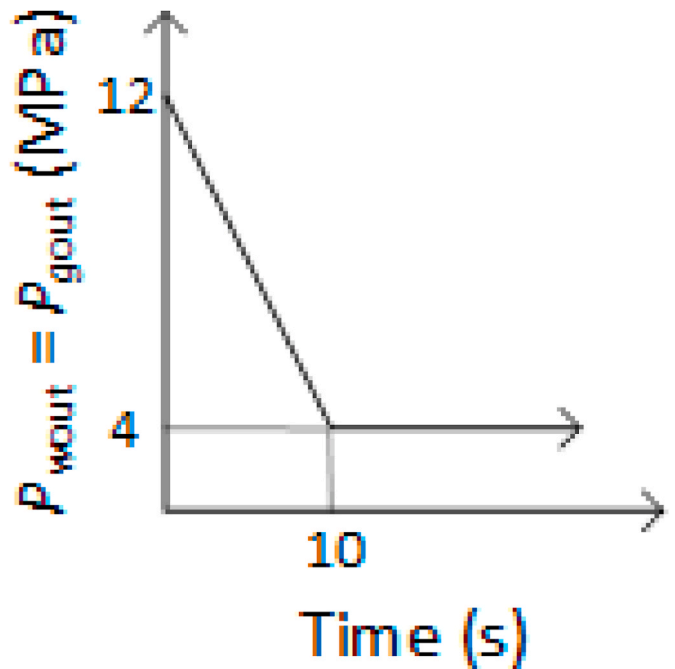


Fig. 3. Time history of fluid pressure at the bottom boundary for BP1.

Table 5
BP1 initial conditions.

Property	Value
Initial Pore Pressure	$P_{w,0} = P_{g,0} = 12 \text{ MPa}$
Initial Effective Stress	$\sigma_o = \sigma'_r = \sigma'_z = \sigma'_\theta = 1 \text{ MPa}$
Initial Total Stress	$\sigma_o = 13 \text{ MPa}$
Initial Hydrate Saturation	$s_{h,0} = 0.0 \text{ (Case 1)}, 0.5 \text{ (Cases 2 and 3)}$
Initial Water Saturation	$s_{w,0} = 1.0 \text{ (Case 1)}, 0.5 \text{ (Cases 2 and 3)}$
Initial Temperature	$T_o = 2^\circ \text{ C (Cases 1 and 2)}, 10^\circ \text{ C (Case 3)}$
Initial Porosity	$\phi_o = 0.4$

temperature vary with case.

4.1.3. Thermo-hydro-chemo-mechanical properties

Table 6 presents key thermo-hydro-chemo-mechanical properties for BP1. For simplicity, an elastic model with hydrate-dependent moduli is suggested. Since the deformation is only volumetric, the elastic bulk modulus governs the mechanical behavior. The intrinsic permeability should be modeled to change as a function of porosity. One of the most common porosity-permeability relationships is the Kozeny-Carman expression (Carman, 1937; Kozeny, 1927), which states:

$$k \propto \frac{\phi^3}{(1-\phi)^2} \quad (1)$$

where k is the intrinsic permeability and ϕ is the porosity. Another relationship, used for this problem to describe the change in permeability with changing porosity, is by Davies and Davies (1999):

$$\ln\left(\frac{k}{k_o}\right) = \gamma\left(\frac{\phi}{\phi_o} - 1\right) \quad (2)$$

where k_o is the initial intrinsic permeability and ϕ_o is the initial porosity, and k and ϕ are the permeability and porosity after compaction. In this problem, according to the Kozeny-Carman expression, the value of γ is approximately $\gamma = 4.6$. In Yoneda et al. (2019a), the value is found to $\gamma = 17.2$ for the Area B gas hydrate-bearing reservoir investigated during the NGHP-02 offshore eastern India. The Yoneda et al. (2019a) results indicate that it is important to consider permeability reduction caused by volumetric deformation, particularly in reservoirs containing compressible fine-grained sediment. For the effective permeability, that is, permeability in the presences of hydrate, Table 6 shows the simple power-law approach suggested by Masuda et al. (1997). The power 3 is estimated based on the data by Yoneda et al. (2019a). Residual saturations for water and gas are both assumed to be zero. For the thermal conductivity, the composite approach is used and leads to $k^T = 2.9 \frac{W}{m \cdot K}$.

For the capillary pressure and relative permeability curve, either the Brooks and Corey model (1964) or van Genuchten model (1980) could be used. For the two models to yield identical values, the following values are suggested:

$$P_c = 12.5 \left[\left(\frac{s_w}{s_w + s_g} \right)^{\left(\frac{1}{0.5} \right)} - 1 \right]^{0.5} [kPa] \quad (3)$$

$$k_w^r = \left(\frac{s_w}{s_w + s_g} \right)^{2.5} = \sqrt{\frac{s_w}{s_w + s_g} \left[1 - \left(1 - \left(\frac{s_w}{s_w + s_g} \right) \right) \right]^2} \quad (4)$$

$$k_g^r = \left(\frac{s_g}{s_w + s_g} \right)^{2.5} = \sqrt{1 - \frac{s_g}{s_w + s_g} \left[1 - \left(\frac{s_w}{s_w + s_g} \right) \right]^2} \quad (5)$$

Table 6
BP1 thermo-hydro-mechanical properties.

Property	Value
Bulk Modulus of Hydrate-Bearing Soil	$K' = 50 + 150 s_h$ [MPa]
Shear Modulus of Hydrate-Bearing Soil	G (any value)
Initial Intrinsic Permeability	$k_o = 10^{-16} m^2 = 0.1 mD$
Effective Permeability	$k_{eff} = k(1 - s_h)^3$
Residual Saturations	$s_{wr} = s_{gr} = 0.0$
Bulk Thermal Conductivity	$k^T = 2.9 W/mK$
Capillary Pressure	Eqn. (3)
Water Relative Permeability	Eqn. (4)
Gas Relative Permeability	Eqn. (5)
Intrinsic Reaction Rate Constant	$K_{do} = 36,400 mol/(m^2 \cdot Pa \cdot s)$
Activation Energy for Hydrate Dissociation	$\Delta E_a = 8.14 kJ/mol$
Hydrate Phase Equilibrium	$P_{eq} = 7 MPa$ at $T = 10^\circ C$

where P_c is the capillary pressure, s_w is the aqueous saturation, s_g is the gas saturation, k_w^r is the aqueous relative permeability, and k_g^r is the gas relative permeability.

The process of hydrate dissociation is assumed to be governed by the first-order kinetics, as suggested by Kim et al. (1987). Thus, the change in the gas hydrate mass is given by

$$\frac{dm_t}{dt} = -M_h K_{d0} \exp\left(\frac{\Delta E_a}{R T}\right) A_d (P_{eq} - f_g) \quad (6)$$

where m_t is the mass of gas hydrate, M_h is the molecular mass of gas hydrate, K_{d0} is the intrinsic reaction rate constant, ΔE_a is the activation energy for gas hydrate dissociation, R is the universal gas constant, T is the temperature, A_d is the surface area available for the reaction, P_{eq} is the temperature-dependent hydrate phase equilibrium pressure, and f_g is the fugacity of the gas. For the hydrate phase equilibrium pressure, each simulator is asked to shift their gas hydrate phase equilibrium curve so that it has $P_{eq} = 7$ MPa at $10^\circ C$. By doing this, hydrate dissociation starts at the effective stress of $\sigma' = 6$ MPa (i.e., 12 MPa + 1 MPa - 7 MPa).

4.1.4. Outputs and simulation cases

Four plots were requested for each of the three simulation cases:

1. Porosity versus effective stress (i.e., total stress - pore pressure)
2. Pore-water pressure versus time
3. Hydrate saturation versus time
4. temperature versus time.

BP1 Case 1 - No Hydrate.

Case 1 is initialized without gas hydrate and an aqueous saturation of 1.0. Expected responses in porosity, pore-water pressure, hydrate saturation and temperature are shown in Fig. 4 (top row). Porosity is expected to decrease from $\phi = 0.4$ to 0.286 and the effective stress should increase from $\sigma' = 1$ to 9 MPa. If permeability is assumed to be constant, there is an analytical solution for time, t , versus pore-water dissipation:

$$t = T_z \frac{\mu_w d^2}{k K'} \quad (7)$$

where T_z is the time factor, μ_w is the viscosity of water, d is the sample height when one-way drainage is specified, k is the intrinsic permeability, and K' is the bulk modulus. For 50% consolidation, $T_z = 0.196$, whereas for 90% consolidation, $T_z = 0.848$. Therefore, using these values and assuming constant intrinsic permeability, it will take approximately 35 s for P_w to reach 8 MPa and 153 s for P_w to reach 4.8 MPa. Since intrinsic permeability decreases with porosity loss during consolidation (Eqn. (1) or (2)), the pore-water dissipation times will be longer than without consolidation. Hydrate saturation is expected to remain zero, and no change in temperature is expected unless the code considers Joule-Thomson effects with pressure changes.

BP1 Case 2 - Hydrate without Dissociation.

Case 2 is initialized with hydrate and aqueous saturation, without gas saturation, and the temperature throughout the consolidation is sufficiently low to avoid hydrate dissociation. Expected responses in porosity, pore-water pressure, hydrate saturation and temperature are shown via the four requested plots in Fig. 4 (middle row). Porosity change is expected to be less than in Case 1, as the soil is stiffer with the addition of gas hydrate. A nonlinear response in porosity is possible if the bulk modulus of the soil increases due to an increase in hydrate saturation. It is expected that the pressure decline to 4 MPa will take longer than Case 1, as the effective permeability of the soil is lower, with the addition of gas hydrate. However, as the soil is stiffer, these two effects counterbalance, as shown in Eqn. (7) (i.e., permeability decreases with porosity reduction together with the increase in hydrate saturation while the bulk modulus of soil increases with the increase in hydrate saturation). The mass of gas hydrate is expected to remain unchanged,

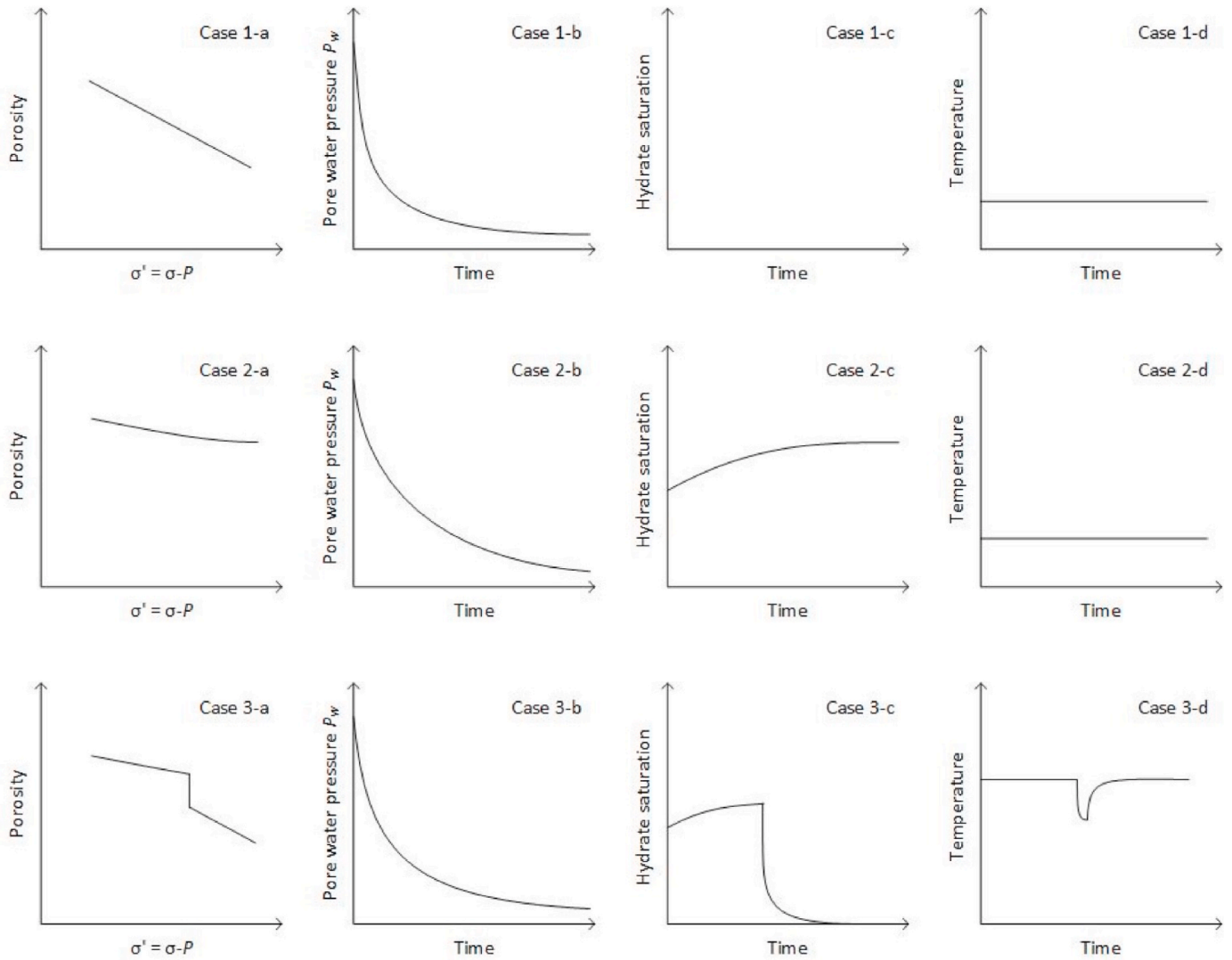


Fig. 4. Expected curve shapes for BP1 Case 1 (upper row), BP1 Case 2 (middle row), and BP1 Case 3 (lower row) of porosity versus effective stress (a), and the time dependence of pore-water pressure (b), hydrate saturation (c) and temperature (d).

while the void volume reduces due to consolidation, the hydrate saturation effectively increases. If not, the mass balance of hydrate is not kept unless the density of hydrate changes. No change is expected in the temperature, unless Joule-Thomson effects are considered.

BP1 Case 3 – Hydrate with Dissociation.

Case 3 is initialized with hydrate and aqueous saturation, without gas saturation, but the temperature throughout the consolidation is not sufficiently low to avoid hydrate dissociation. Rapid dissociation of the gas hydrate is expected, with complete hydrate dissociation under the constant effective stress. This is expected to yield a sudden reduction in porosity at $\sigma' = 6\text{MPa}$ caused by hydrate-dissociation induced stress relaxation (see the sub-section 4.1.5 for details). Under aqueous-gas multiphase conditions, the following representative pore pressure is recommended (Bishop, 1959):

$$P = \frac{s_w P_w + s_g P_g}{s_w + s_g} \quad (8)$$

where s is saturation, P is pressure, and the subscripts w and g represent water and gas, respectively. The final porosity should be identical to Case 1, which is $\phi \approx 0.286$. If not, the mechanical model is missing the stress relaxation term. Complete consolidation is expected to take longer than Case 1, but shorter than Case 2. Hydrate dissociation is expected to

be rapid because of the availability of heat as all the outer boundaries are constant temperature. Temperature is expected to remain nearly constant, with a sharp decline and then recovery during the hydrate dissociation process. The exact timescale for recovery depends on the values of the thermal conductivity and bulk heat capacity, relative to the effective permeability.

4.1.5. Stress-strain relationship and hydrate bearing soil elastic stiffness

Upon hydrate dissociation, the effective stress supported by the solid hydrate in pores is released. This leads to the reduction in effective stress under zero straining, the process known as stress relaxation. The non-uniform hydrate dissociation can lead to non-uniform stress relaxation and stress redistribution, resulting in a very complex mechanical behavior of hydrate-bearing sediments. We briefly describe the hydrate-dissociation induced stress relaxation. The detailed derivation of this stress relaxation term can be found in Uchida et al. (2012).

The stress-strain relationship of hydrate-bearing sediment can be given by:

$$\sigma' - \sigma'_0 = D_{hs} \epsilon \quad (9)$$

where σ' is the current effective stress vector (i.e., tensor in a vector form), σ'_0 is the effective stress when hydrate is formed, D_{hs} is the elastic

stiffness matrix for hydrate-bearing soil and ϵ is the elastic strain vector (i.e., tensor in a vector form). Solid-phase hydrate contributes to soil strength and stiffness. For simplicity, we will assume that the hydrate-bearing soil's elastic stiffness can be given by:

$$D_{hs} = D_s + D_{h0}s_h \quad (10)$$

where D_s is the elastic stiffness matrix of the host soil (without hydrate), D_{h0} is the proportionality of the elastic stiffness due to hydrate, and s_h is the hydrate saturation. Therefore, the incremental form of Eqn. (9) is

$$d\sigma' = D_{hs}d\epsilon + D_{h0} [D_{hs}]^{-1} (\sigma' - \sigma_0')ds_h \quad (11)$$

The first term on the right-hand-side of Eqn. (11) is a conventional stress-strain relationship and the second term states that the effective stress decreases when hydrate dissociates ($ds_h < 0$) without straining. This is hydrate-dissociation-induced stress relaxation. When the effective stress remains almost constant ($d\sigma' = 0$) due to constant confinement during hydrate dissociation (like Case 3), the stress relaxation term is then compensated by additional deformation. Therefore, in Case 3, there is deformation at constant effective stress due to hydrate dissociation.

4.2. BP1 simulation results and comparisons

Solutions for BP1 were submitted by teams from LLNL-Tongji, NETL, PNNL, UCB, and Ulsan-KIGAM.

4.2.1. BP1 case 1 – No hydrate

Expected responses for Case 1 are described above and included a linear decay in porosity from 0.4 to 0.286 and an asymptotic decay in pore pressure. Simulation results for porosity versus effective stress and pore-pressure versus time are shown in Fig. 5(a) and (b), respectively. Simulation results matched the shapes of the expected results, as shown in Fig. 4 (top row), in terms of porosity versus effective stress, Fig. 5(a), and pore-pressure versus time, Fig. 5(b). Differences among the submitting teams and against the expected results for the decay in pore pressure are probably due to the nature of the dependency between porosity and permeability specified in the codes for the simulation. Simulation teams had some flexibility in this model and its parameters.

4.2.2. BP1 case 2 – hydrate without dissociation

Expected responses for Case 2 are described above and, relative to Case 1, include a reduced change in porosity, a slower decay in pore pressure, a slight increase in hydrate saturation and no change in temperature. Simulation results for porosity versus effective stress and pore-pressure versus time, hydrate saturation versus time, and temperature versus time are shown in Fig. 6(a)–(d), respectively. Results for porosity versus effective stress (Fig. 6(a)) for all of the submitting teams showed smaller changes due to the increased soil stiffness with gas hydrate. Considerable differences were noted for the rate of change of pore pressure versus time (Fig. 6(b)), across the teams. It was expected that pore pressure would decrease slower than in Case 1 due to decreased effective permeability with gas hydrate, but the reduction in permeability with the increase in soil stiffness (i.e., bulk modulus) was expected to counterbalance this effect (Eq. (7)). The LLNL-Tongji solution appears to have an effective permeability model that yields greater reductions in effective permeability with hydrate saturation. This solution, as with PNNL's, use sequential iterative approaches to couple flow and heat transport with geomechanics, but selection of a tighter convergence criterion for the sequential coupling should eliminate this as a factor in the delayed pressure response.

As expected, the modeled hydrate saturation increased with decreasing porosity upon consolidation (Fig. 6(c)). Plotting the hydrate saturation versus effective stress avoids any time dependent differences, showing better agreement in results across the solutions. There are two groups of solutions, those resulting from assuming a constant gas

hydrate density (i.e., LLNL-Tongji and NETL) and those with variable gas hydrate density. Also as expected, the modeled temperature results show only slight variations in temperature, generally associated with the changes in pore pressure and Joule-Thomson effect. The Ulsan-KIGAM solution showed a slight increase in temperature during the period of sharp pressure decline (i.e., resulting from a negative Joule-Thomson coefficient), and the LLNL-Tongji solution showed a moderate decrease in temperature with a decline in pressure (a positive Joule-Thomson coefficient).

4.2.3. BP1 case 3 – hydrate with dissociation

The most significant differences between this case and Cases 1 and 2 occurs during the period of hydrate dissociation. Simulation results for the change in porosity versus effective stress from the submitting solutions are shown in Fig. 7(a) and generally follow the expected results, shown in the first panel of Fig. 4 (bottom row), with a linear decrease, as in Case 2, followed by a sharp decrease during dissociation, and then a continued linear decrease with a steeper slope, as in Case 1. Simulation results for pore pressure versus time (Fig. 7(b)) differ slightly from the expected results and across the teams. The difference from the expected results occurs during the dissociation period while hydrate dissociation is occurring at a constant pressure, due to the constant temperature boundary and small volume to surface area ratio. Most solutions show a plateau in pressure around 7 MPa during the period of hydrate dissociation. Differences in pore pressure decline rates are compounded in this case, due to the rates of hydrate dissociation plus the change in effective permeability. To eliminate time dependences, simulation results for changes in hydrate saturation versus effective stress (Fig. 7(c)), show good agreement across the submitting teams. Hydrate saturation increases initially with consolidation, then decreases as hydrate dissociates under constant effective stress conditions. Dissociation coincides with the constant pore-pressure interval (Fig. 7(b)) due to nearly constant temperature conditions. Numerical simulation results for temperature versus time (Fig. 7(d)), generally agree across the submitting teams and with the expected results, shown in the bottom-right panel of Fig. 4. Temperature remains constant prior to the onset of hydrate dissociation, then dips slightly because hydrate dissociation is endothermic, then recovers via thermal conduction from the constant temperature boundary.

4.3. BP1 summary

At first inspection, a single node (model cell) consolidation problem with or without gas hydrate would appear to be the most basic of problems involving coupled hydrologic, thermal, and geomechanical processes. Analytical solutions were not sought for this benchmark problem, but the expected results, shown in Fig. 4, were derived through thinking through the coupled processes, and generally represented the simulation results. Simulation results from Case 1 without hydrate and Case 2 with hydrate but no dissociation, showed good agreement across the simulation results, but highlighted the importance of modeling effective permeability (i.e., permeability evolution in response to changes in porosity and pore-filling material, such as gas hydrate). The consequences of these differences in effective permeability modeling persisted in Case 3, and were especially evident in the pore pressure versus time relationship (Fig. 7(b)), but were additionally compounded by differences in the modeled rate of hydrate dissociation. As with the effective permeability, the hydrate dissociation rate impacted the pressure response of the system versus time. Overall simulation results show good agreement when plotted against effective stress, which eliminates the temporal elements of the problem.

5. Benchmark problem 2 – Extended Terzaghi Problem

BP2 Champion: Shubhangi Gupta, GEOMAR.

In BP2, we extend the classical 1D consolidation problem proposed

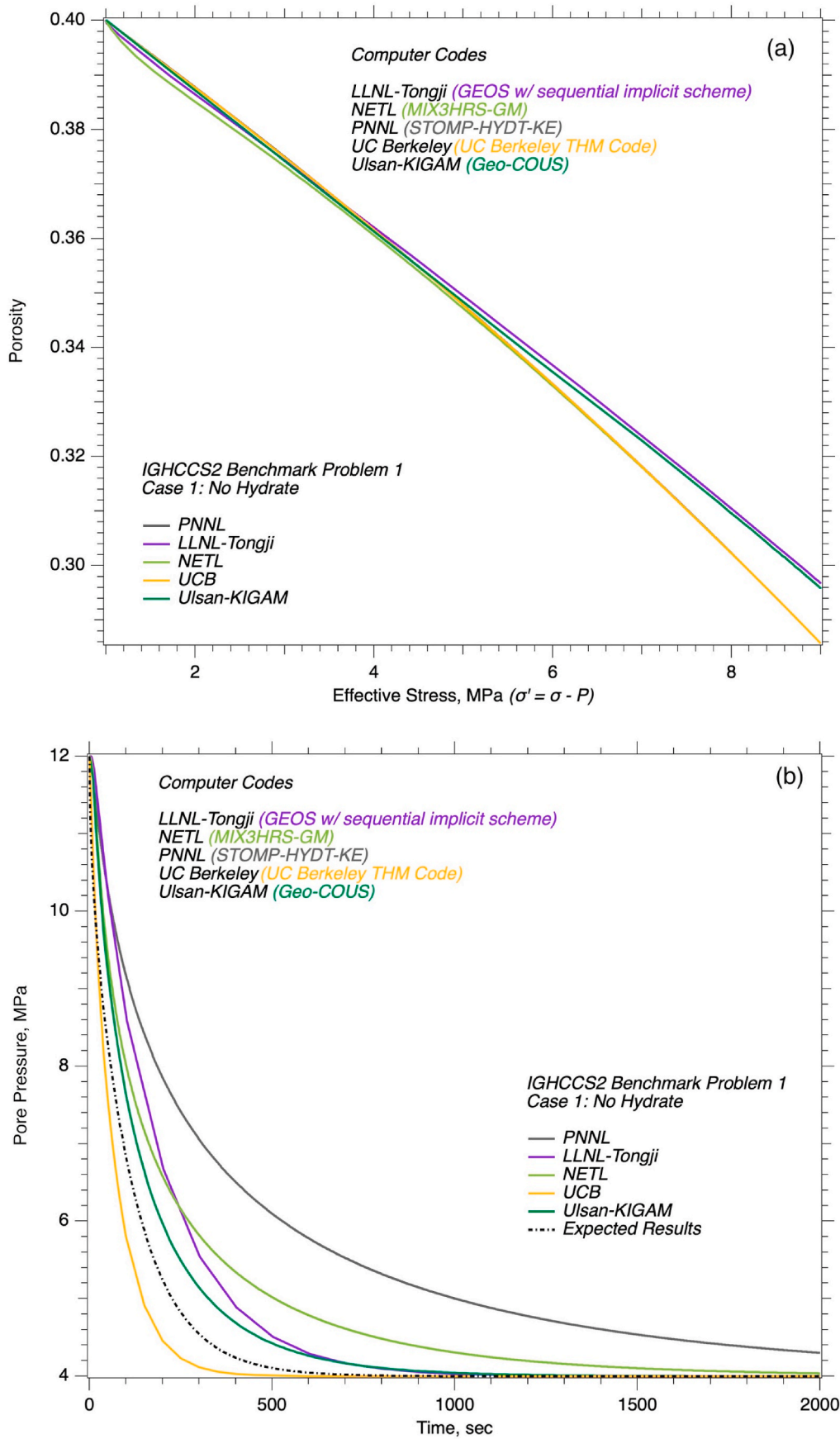


Fig. 5. BP1 Case 1 model outputs for (a) porosity versus effective stress and (b) pore-pressure versus time.

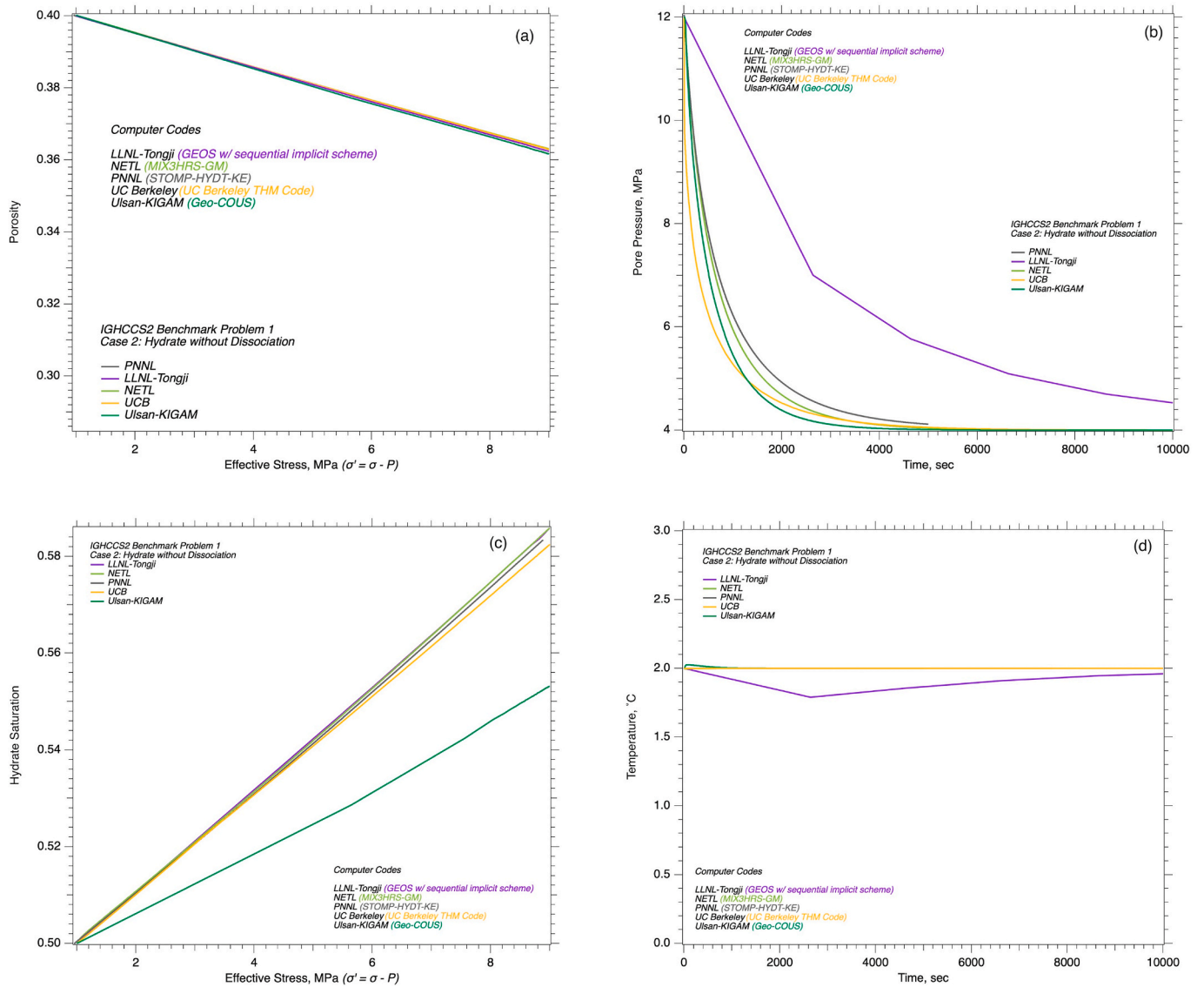


Fig. 6. BP1 Case 2 model outputs for (a) porosity versus effective stress, (b) pore-pressure versus time, (c) hydrate saturation versus time, and (d) temperature versus time.

by Terzaghi (1943) to include the effects of methane hydrate kinetics on the standard poro-elastic coupling. Terzaghi’s problem is widely accepted as one of the standard benchmarks for verifying the poro-elastic coupling conditions in hydro-geomechanical models cast within the framework of infinitesimal strain theory. Terzaghi’s problem and its numerous variations (e.g., Verruijt (2013); Wang (2000)) simulates the pore-pressure response generated by the mechanical compression of a confined soil column through the application of a constant, ramped, or cyclic vertical stress. The mathematical description of Terzaghi’s problem in 1D reduces to a simple diffusion equation for which closed-form or semi-analytical solutions can be derived (e.g., Verruijt (2013); Wang (2000)). Due to the simplicity of the problem setting and the availability of analytical solutions for a variety of time-dependent loading conditions, Terzaghi’s problem is deemed a necessary (but not sufficient) test for the numerical implementation of any hydrogeomechanical simulator (Terzaghi, 1943).

Our motivation for developing this benchmark problem is to provide a similar standardized test setting specific to gas hydrate models which can be used for:

- analyzing and validating the numerical strategies for coupling reactive transport and geomechanical codes for gas hydrates; and,
- understanding the main bi-directional couplings (i.e., kinetic phase change ↔ fluid flow ↔ mechanical deformation), which characterize a typical mathematical model for gas hydrates. A schematic for this problem is shown in Fig. 8.

5.1. BP2 mathematical framework

In order to develop BP2 and to understand its characteristics, we briefly consider a simplified mathematical framework. Let us consider a homogenized representative elementary volume (REV) composed of four distinct phases: methane, water, hydrate, and soil. The relevant homogenized state variables (e.g., phase saturations, porosities) are defined in Fig. 9.

Using Darcy’s law to model fluid flow, the small strain theory for the soil displacements, and for simplicity, ignoring the effects of gravity, fluid miscibility, and capillary pressure, we can reformulate the mass balance equations for the four phases and obtain a partial differential equation (PDE) governing the pore fluid pressure P , also known as the

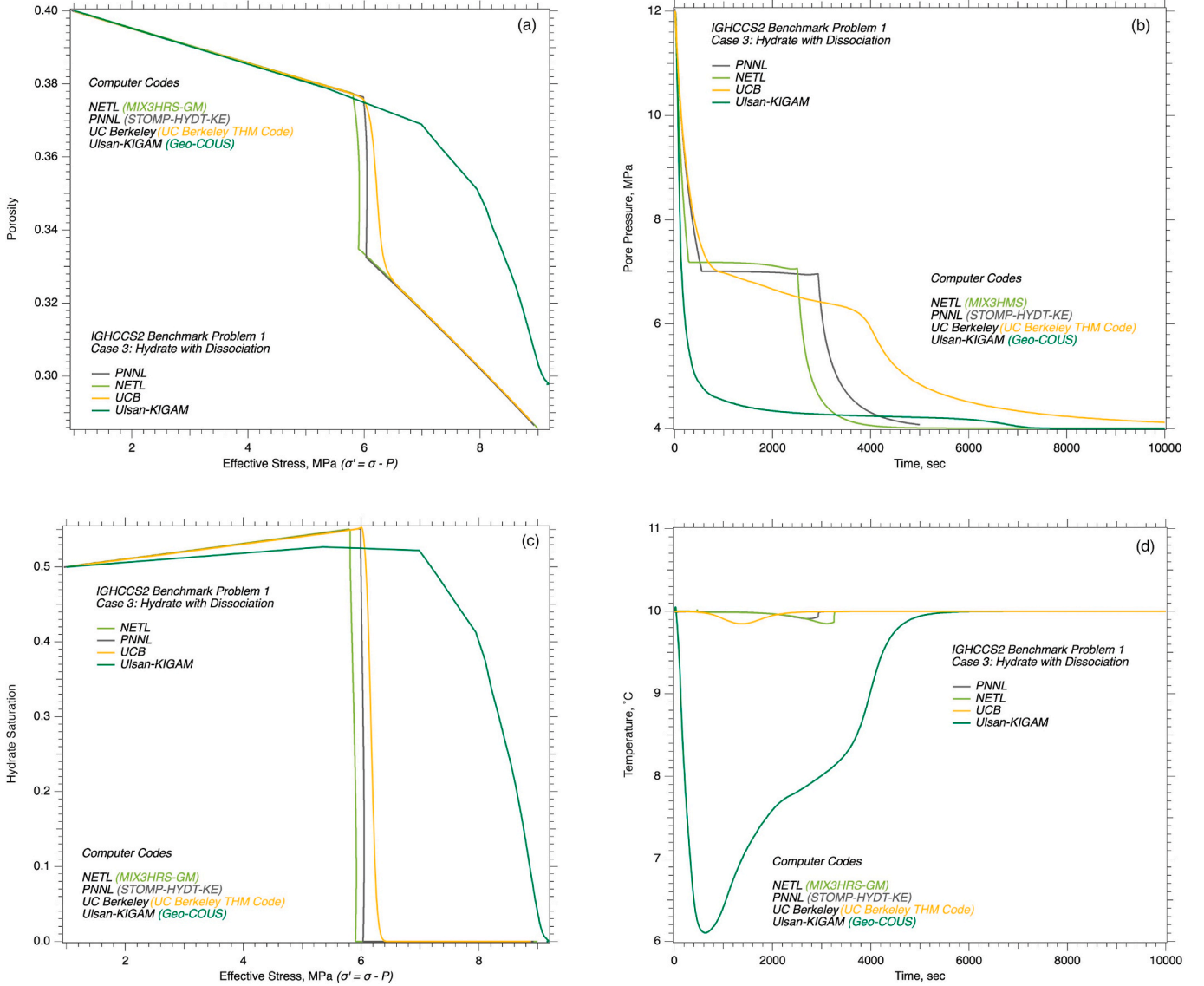


Fig. 7. BP1 Case 3 model outputs for (a) porosity versus effective stress, (b) pore-pressure versus time, (c) hydrate saturation versus time, and (d) temperature versus time.

storage equation, for which a detailed derivation can be found in Gupta et al. (2015),

$$\alpha \frac{d}{dt} \varepsilon_v + S \frac{d}{dt} P = \nabla \cdot \frac{k}{\mu_f} \nabla P + \sum_{\beta=g,w,h} \dot{g}_\beta \quad (12)$$

where ε_v is the volumetric strain given as $\varepsilon_v = \nabla \cdot \mathbf{u}$, α is Biot's constant, k is absolute permeability, and μ_f is the fluid mobility,

$$\frac{1}{\mu_f} = \left(\frac{k_g^r}{\mu_g} + \frac{k_w^r}{\mu_w} \right)$$

where k_β^r and μ_β are the relative permeability and dynamic viscosity of the fluid phases, respectively. The term S , called the *storativity*, is given as,

$$S = \phi_e \left(C_w s_w + C_g s_g \right) + C_{s,h} (\alpha - \phi_e)$$

where C_w , C_g , and $C_{s,h}$ are the phase compressibilities of water, methane, and composite hydrate + soil matrix, respectively. \dot{g}_β are the volumetric source/sink terms for methane, water, and hydrate phases due to the

hydrate phase change kinetics, which can be modeled as

$$\dot{g}_g = \frac{k^r M_g A_{rs} (P_{eq} - P)}{\rho_g}, \dot{g}_w = \dot{g}_g N_h \frac{\rho_g M_w}{\rho_w M_g}, \dot{g}_h = -\dot{g}_g \frac{\rho_g M_h}{\rho_h M_g} \quad (13)$$

where k^r is the reaction rate, A_{rs} is the specific surface area available for the phase change reaction, M_β denotes the molar mass of the respective phases, and N_h is the hydration number, the number of water molecules per caged methane molecule. The volumetric source terms can be lumped together as,

$$\sum_{\beta=g,w,h} \dot{g}_\beta = C(P_e - P) \quad (14)$$

where P_{eq} is the hydrate equilibrium pressure, and

$$C = \left(N_h \frac{M_w}{\rho_w} + \frac{M_g}{\rho_g} - \frac{M_h}{\rho_h} \right) k^r A_{rs}$$

Using Eqn. (14), we can rewrite the storage equation as,

$$\alpha \frac{d}{dt} \varepsilon_v + S \frac{d}{dt} P = \nabla \cdot \frac{k}{\mu_f} \nabla P + C(P_e - P) \quad (15)$$

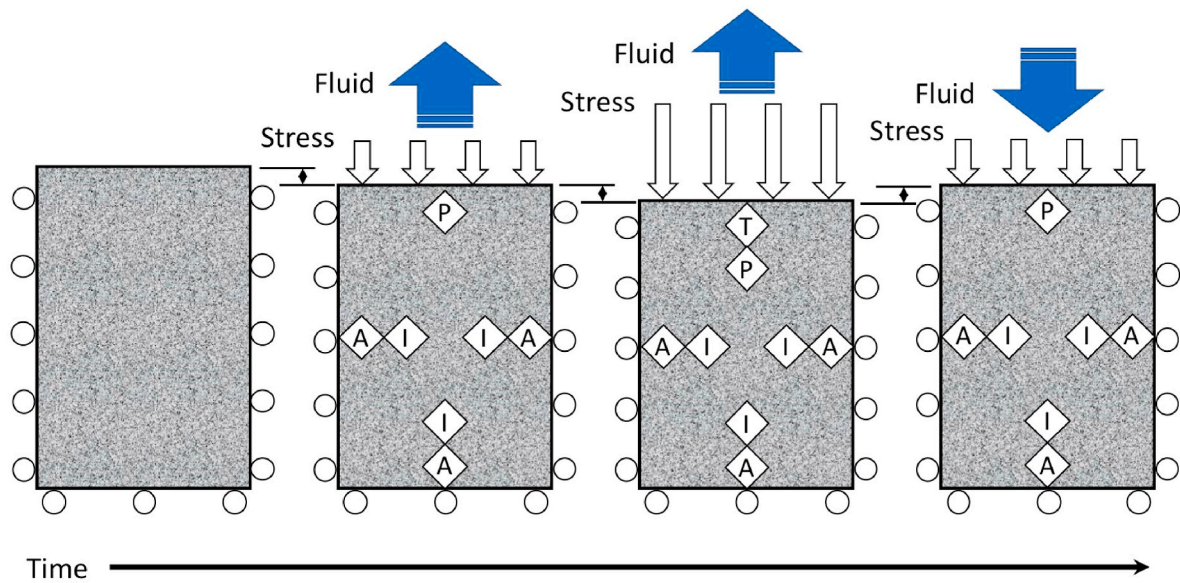


Fig. 8. Conceptual schematic of BP2, with white arrows indicating a stress boundary, circles indicating a roller boundary, T indicating a temperature boundary, P indicating a pressure boundary, I indicating an impermeable boundary, and A indicating an adiabatic boundary. Fluid moves out and into the model domain across the top surface (blue arrows) in response to the evolving stress state. (For interpretation of the references to colour in this figure legend, the reader is referred to the Web version of this article.)

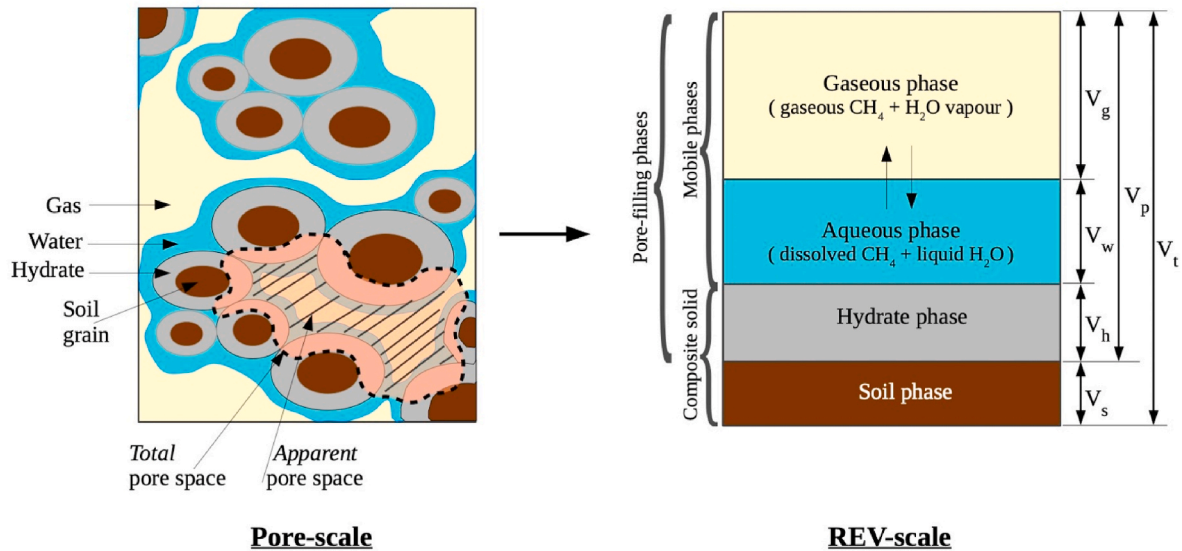


Fig. 9. Representation of the phases and components in a homogenized representative elementary volume (REV), shown at the pore-scale as a grain-coating gas hydrate. For any pore-filling phase $\beta = g, w, h$, phase saturation is defined as $s_\beta = \frac{V_\beta}{V_p}$, where V is volume and the subscripts are defined in the right-hand panel. Total and effective porosities are defined as $\phi = \frac{V_p}{V_t}$ and $\phi_e = \frac{V_p - V_h}{V_t} = \phi(1 - s_h)$, respectively. Effective saturation of a fluid phase $\beta = g, w$ is defined as $s_\beta^e = \frac{s_\beta}{1 - s_h}$.

Observe that in Eqn. (15), the term $\left[\alpha \frac{d}{dt} \epsilon_v \right]$ is a purely mechanical part, and the term $\left[\nabla \cdot \frac{k}{\mu_f} \nabla P \right]$ is a purely flow part. The terms $\left[S \frac{d}{dt} P \right]$ and $[C(P_e - P)]$ are the coupling terms, the former couples the flow and the mechanical models, and the latter couples flow and the reaction kinetics models. This is a very powerful feature of this problem, since it allows us to isolate the effects of the chemical-hydrological and hydrological-mechanical couplings in a gas hydrate model.

In 1-dimension, Eqn. (15) can be reduced further. For uniaxial deformation, the volumetric strain equals the vertical strain and is induced by the vertical stress σ_{zz} ,

$$\frac{d}{dt} \epsilon_v = -C_m \frac{d}{dt} \sigma_{zz} = -C_m \left(\frac{d}{dt} \sigma_{zz} - \alpha \frac{d}{dt} P \right) \quad (16)$$

where C_m is the compressibility of the bulk porous material. Thus, we can eliminate $\frac{d}{dt} \epsilon_v$ in Eqn. (15), yielding,

$$\frac{d}{dt} P = \frac{\alpha C_m}{\alpha^2 C_m + S} \frac{d}{dt} \sigma_{zz} + \frac{k}{\mu_f (\alpha^2 C_m + S)} \frac{d^2}{dz^2} P + \frac{C}{\alpha^2 C_m + S} (P_e - P)$$

Denoting,

$$\mathcal{L} = \frac{\alpha C_m}{\alpha^2 C_m + S} \frac{d}{dt} \sigma_{zz}, C_v = \frac{k}{\mu_f (\alpha^2 C_m + S)}, C_r = \frac{C}{\alpha^2 C_m + S}$$

yields,

$$\frac{d}{dt}P = \mathcal{L} + C_v \frac{d^2}{dz^2}P + C_r(P_e - P) \quad (17)$$

Here, we can clearly see how the classical Terzaghi problem (i.e., the first three terms of Eqn. (17)) is extended to include the hydrate phase change kinetics. C_v is the consolidation parameter, which comes from Terzaghi's classical theory of consolidation. \mathcal{L} is a time dependent forcing function due to the applied stress. For the special case of a constant applied stress, $\mathcal{L} = 0$. For a ramped applied stress, \mathcal{L} is constant. C_r is the reaction parameter. It indicates the damping of the pore-pressure response due to hydrate phase change kinetics. The ratio C_v/C_r can also be used as an indicator for the relative activities of the hydrate kinetics and geomechanical processes (Gupta et al., 2016).

Eqn. (15) is a simplified framework for BP2 which provides some useful indicators for analyzing the coupling terms in the gas hydrate models. For some very specific test settings, it is also possible to derive analytical or semi-analytical solutions for this model (e.g., Gupta et al. (2015)). However, for most test settings of interest, analytical solutions do not exist yet, especially with the thermal effects. So instead, with BP2 we aim to develop a theoretical test setting which is based on this mathematical framework, but considers realistic constitutive models and phase properties as well as the associated thermal effects. In this code comparison study, we provide a standardized reference setting and compare the numerical solutions of the different thermal-geochemical-hydrological-mechanical (TCHM) gas hydrate codes in relation to the theoretical model indicators.

5.2. BP2 description

The problem is set as a confined soil column of length $L = 1$ m with homogeneous and isotropic properties and phase distributions. Initially, the water saturation in the column is 60%, the gas (i.e., methane and water vapor) saturation is 40%, and the hydrate saturation is 0. The porosity of the hydrate free sample is 15% and the absolute permeability is 0.1 mD. The initial pressure-temperature (P-T) state of the system lies well outside the hydrate stability curve. The lower boundary of the soil column (at $z = 0$) is impermeable, and the upper boundary (at $z = L$) is fully drained. The column is loaded at its upper surface by a ramped vertical compressive stress for a total period of 2000 s. The load is first increased at a constant rate of 0.01 MPa/s for 1000 s, and then decreased at the same rate for the next 1000 s. Unlike the assumption of isothermal processes in Terzaghi's problem, hydrate phase change is a non-isothermal process. Heat is released when hydrate forms, and absorbed during dissociation. We, therefore, also consider thermal effects in our setting, and assume that the column is fully insulated on all sides. The initial and boundary conditions are listed in Table 7. The main assumptions, constitutive models, and relevant parameters are also specified in Table 7. Note that, in the derivation of Eqn. (15), we ignored the capillary pressure effects for the ease of mathematical presentation. However, in our numerical simulations we do, in fact, consider this effect.

Initially, with no gas hydrates in the domain, this test setting resembles the classical Terzaghi problem. As the external load ramps up, we expect excess pore-pressure to build up in the soil column. If the pore pressure exceeds the hydrate equilibrium pressure P_{eq} , hydrate will start to form in the domain and a further build-up of the excess pore-pressure will be damped. When the external load ramps down, the excess pore pressure begins to gradually dissipate, which causes the hydrate to dissociate. Again, the rate of pressure dissipation is damped by the hydrate dissociation process. The degree of damping is controlled by the parameter C_r . From Eqn. (15), we can see that the thermal feedbacks from the hydrate kinetics can affect the pore-pressure evolution mainly through P_{eq} and S (assuming that the temperature dependence of mechanical and hydraulic properties is negligible). The parameter S varies

due to the strong temperature dependence of gas compressibility. In general, parameter C can also show non-negligible temperature dependence, but in this problem, we have assumed a constant hydrate reaction rate, and therefore, a temperature independent C .

5.3. BP2 numerical simulation results

We discretize the domain uniformly into 100 cells of size $\Delta z = 0.01$ m. For code comparison, we consider 4 test cases with different combinations of the model parameters k^r (hydrate reaction rate) and γ (contribution of hydrate to G_{sh}), where G_{sh} is the combined shear modulus of the porous media and gas hydrate:

BP2 Case 1 - No hydrate kinetics ($k^r = 0$).

In this case, $C = 0$ and $G_{sh} = G_s$ (because $s_h = 0$, and the choice of γ is immaterial). The setting reduces to Terzaghi's problem, but with a highly compressible gas phase and a weak temperature coupling. For this case, we set the initial temperature to 20 °C. The main objective is to compare the non-isothermal poro-elastic coupling in the participating codes *without* gas hydrates.

BP2 Case 2 - With hydrate kinetics ($k^r = 2.5 \times 10^{-10} \frac{\text{mol}}{\text{m}^2 \text{Pa s}}$, $\gamma = 1$).

In this case, we compare the codes *with* gas hydrate kinetics and related thermal effects. The kinetic rate for this case is based on the measurements of Kim et al. (1987).

BP2 Case 3 - With higher contribution of hydrate to G_{sh} ($k^r = 2.5 \times 10^{-10} \frac{\text{mol}}{\text{m}^2 \text{Pa s}}$, a) $\gamma = 0.1$, b) $\gamma = 0.01$).

In this case, we extend Case 2 to see the effect of higher and lower contribution of hydrate to the shear modulus of soil + hydrate composite matrix. Two sub cases are considered with different L values.

BP2 Case 4 - Very fast hydrate kinetics ($k^r = 2.5 \times 10^{-6} \frac{\text{mol}}{\text{m}^2 \text{Pa s}}$, $\gamma = 1$).

High kinetic rates can lead to ill-conditional matrices and cause instabilities in the numerical solution. We compare the codes for very fast hydrate kinetics. The kinetic rate for this case is 10^4 times that of Case 2.

The numerical results for Case 1 are plotted in Fig. 10, for Case 2 in Figs. 11 and 12, for Case 3 in Fig. 13 through 16, and for Case 4 in Figs. 17 and 18. The P , T , and s_h profiles are shown at a representative location $z/L = 0.605$ inside the domain, and the z -displacement is plotted at the upper surface $z/L = 1.0$.

5.4. BP2 summary

The solutions computed by the different codes show similar qualitative behavior, but quantitatively, their differences are rather large. Given that the models are complex with a large number of bi-directional process couplings and strongly nonlinear parameterizations, it is challenging to identify the factors leading to the observed differences. However, if we look at the solutions through the lens of the idealized mathematical problem developed in Section 5.1, it becomes easier to identify the controls on the bi-directional couplings and obtain a more quantitative basis for comparing different codes for the gas hydrate models.

First, let us look at the solutions for Case 1 (Fig. 10) with no hydrate kinetics. According to Eqn. (17), for this problem $C_r = 0$ and C_m is constant, and the problem is therefore controlled only by two parameters, C_v and \mathcal{L} . The parameter \mathcal{L} controls how the applied stress acts on the phases, and the parameter C_v controls the rate of consolidation. *The main difference among the codes in this case appears to be due to the contribution of storativity, S , to C_v and \mathcal{L} .* The storativity depends

Table 7
BP2 problem specifications.

Initial Conditions	
at $t = 0$ s, and $0 \text{ m} \leq z \leq 1 \text{ m}$	$P_g = 3.25 \text{ MPa}$ $s_w = 0.6$ $s_h = 0.0$ $T = 4^\circ\text{C}$ $\phi = 0.15$ $k = 0.1 \text{ mD}$
Boundary Conditions	
at $z = 0 \text{ m}$, and $0 < t \leq 2000 \text{ s}$	$v_g \cdot \mathbf{n} = 0$ $v_w \cdot \mathbf{n} = 0$ $\nabla T \cdot \mathbf{n} = 0$ $u_z = 0$
at $z = 1 \text{ m}$, and $0 < t \leq 2000 \text{ s}$	$P_g = 3.25 \text{ MPa}$ $s_w^e = 0.6$ $\nabla T \cdot \mathbf{n} = 0$ $\sigma_{zz} = \begin{cases} -0.01 \text{ t, if } 0 \leq t < 1000 \text{ s} \\ -10 + 0.01(t - 1000), \text{ if } t \geq 1000 \text{ s} \end{cases}$
Main Assumptions	
Effects of gravity, gas-water miscibility, and water salinity are ignored.	
Ice formation is ignored.	
Gas phase contains pure methane, and only methane hydrate can form.	
Soil displacements are infinitesimally small, and the stress-strain response is linear-elastic.	
Hydraulic Properties	
Capillary Pressure	
	$P_c = P_{c,0} f_{sh}^{pc} f_\phi^{pc}$ $\text{where, } P_{c,0} = P_o (s_w^e)^\lambda \frac{-1}{1 - m \lambda}$ $f_{sh}^{pc} = (1 - s_h) \frac{1 - m \lambda}{m \lambda}$, and $f_\phi^{pc} = \frac{\phi_0}{\phi} \left(\frac{1 - \phi}{1 - \phi_0} \right)^a$ $k = k_o f_{sh}^k f_\phi^k$ $\text{where, } f_{sh}^k = (1 - s_h) \frac{5m + 4}{2m}$ and $f_\phi^k = \frac{\phi}{\phi_o} (f_\phi^{pc})^{-2}$ $k_w^r = (s_w^e)^\lambda \left(\frac{2 + 3\lambda}{\lambda} \right)$ $k_g^r = (1 - s_w^e)^2 \left(1 - (s_w^e)^\lambda \left(\frac{2 + \lambda}{\lambda} \right) \right)$ $P_o = 50 \text{ kPa}$, $\lambda = 1.2$, $a = 1$, $m = 3$ k_o and ϕ_o denote values at $t = 0$
Intrinsic Permeability	
Relative Permeabilities	
Constants	
Hydrate Phase Change Kinetics	
Kinetic Rates	
Hydrate Equilibria	
Reaction Rate	
	$\dot{g}_g = k^r M_g A_{rs} (P_e - P)$, $\dot{g}_w = \dot{g}_g N_h \frac{M_w}{M_g}$, $\dot{g}_h = -\dot{g}_g \frac{M_h}{M_g}$ $P_{eq} [\text{kPa}] = \exp \left(38.98 - \frac{8533.8}{T [\text{K}]} \right)$ Case 1 - No hydrate kinetics $(k^r = 0)$ Case 2 - With hydrate kinetics $(k^r = 2.5 \times 10^{-10} \frac{\text{mol}}{\text{m}^2 \text{ Pa s}}, \gamma = 1)$ Case 3 - With higher contribution of hydrate to G_{sh} $(k^r = 2.5 \times 10^{-10} \frac{\text{mol}}{\text{m}^2 \text{ Pa s}}, a) \gamma = 0.1, b) \gamma = 0.01)$ Case 4 - Very fast hydrate kinetics $(k^r = 2.5 \times 10^{-6} \frac{\text{mol}}{\text{m}^2 \text{ Pa s}}, \gamma = 1)$
Specific Reaction Surface Area	
	$A_{rs} \left[\frac{\text{m}^2}{\text{m}^3} \right] = 10^6 \Gamma_s$ $\text{where, } \Gamma_s = \begin{cases} \phi s_h & \text{for } P_e \geq P \\ s_g s_w (1 - s_h) & \text{for } P_e < P \end{cases}$ $\dot{Q}_h \left[\frac{\text{W}}{\text{m}^3} \right] = -\frac{\dot{g}_g}{M_h} (56599 - 16.744 T [\text{K}])$
Heat of Hydrate Dissociation	
Constants	
Mechanical Properties	
Soil Shear Modulus	
Hydrate Shear Modulus	
Composite Shear Modulus	
Composite Poisson Ratio	
Biot's Coefficient	
	$G_s = 2.5 \text{ GPa}$ $G_h = 2.5 \text{ GPa}$ $G_{sh} = G_s + \gamma s_h G_h$ $\nu_{sh} = 0.2$ $\alpha = 1$
Phase Properties	

(continued on next page)

Table 7 (continued)

Phase Properties	Methane	Water	Hydrate	Soil Grains
	Methane	Water	Hydrate	Soil Grains
Density $\left[\frac{kg}{m^3}\right]$	a	a	900 or ^a	2600
Compressibility $[Pa^{-1}]$	a	a	–	–
Dynamic Viscosity $[Pa\ s]$	10^{-5} or ^a	10^{-3} or ^a	–	–
Thermal Conductivity ^b $\left[\frac{W}{m\ K}\right]$	0.044 or ^a	0.5	0.5	3
Heat Capacity ^b $\left[\frac{J}{kg\ K}\right]$	3274 or ^a	3945 or ^a	800 or ^a	1000

^a Density and compressibility are not specified, but computed within each participating code.

^b Average rule for effective property. $(\)^{eff} = (1 - \phi)(\)_s + \phi \sum_{\beta=g,w,h} (\)_{\beta}$

dominantly on the gas compressibility C_g (because, $C_w \ll C_g$ and C_s is constant). The gas compressibility and the corresponding C_v and \mathcal{L} parameters are plotted for the GEOMAR, PNNL, and NETL solutions in Fig. 19. The parameterization of C_g , in the storativity, and thus in C_v and \mathcal{L} in the PNNL and NETL codes match closely. Therefore, their numerical solutions also show a close match.

Next, we look at the solutions for Case 2 (Figs. 11 and 12) with hydrate kinetics. Again, according to Eqn. (17) this problem is controlled by \mathcal{L} , C_v , and C_r . These parameters are plotted for GEOMAR, PNNL, and NETL solutions in Figs. 20 and 21. In this case, storativity is not only controlled by C_g (Fig. 21), but also by C_m and C_{sh} (Fig. 20), which are linear functions of s_h . Note that C_{sh} and C_m are one and two orders of magnitude smaller than C_g , respectively. Therefore, \mathcal{L} and C_v are still dominantly controlled by the gas compressibility. While C_v controls the rate of consolidation, C_r counters the effect of C_v by damping the pore-pressure response. The parameter C_r depends on $A_s \cdot k'$ (Fig. 22). The k' values for PNNL and NETL are almost one order of magnitude smaller than for GEOMAR. The reaction surface area for PNNL is one order of magnitude smaller than that of GEOMAR, while the reaction surface area for NETL is one order of magnitude larger than that of GEOMAR. It is also worth noting that the available reaction surface area appears to increase for NETL during hydrate formation, as opposed to the trend for GEOMAR and PNNL. The differences in the solutions for s_h (Fig. 12) arise directly from the differences in the hydrate phase change models in their respective codes. The higher the value of C_r , the closer the pore-pressure gets to the hydrate equilibrium pressure P_e . In codes where the kinetics is modeled based on fugacities, the gas fugacity approaches P_e (and consequently, the pore pressure is higher). The differences in the pore pressures (Fig. 11), therefore, arise due to a combination of P_e and C_r values. For GEOMAR solution, the C_r value is high enough that P_g coincides with P_e , for the GEOMAR temperature profile (Fig. 11(b)) (see Fig. 23).

In Case 3, the γ parameter affects the values of C_m and C_{sh} . For $\gamma = 0.1$, the effect of s_h is expected to dominate. Another quantity of interest is the ratio C_r/C_v , which indicates the relative activities (i.e., time scales) of the kinetics and consolidation processes. In Case 4, where the rate of kinetic reaction is four orders of magnitude higher than in Cases 2 and 3, this ratio is expected to be very large, leading to very small time step sizes. In such cases, it can be helpful to exploit this difference in time scales to develop multi-rate time-stepping schemes to reduce the computational costs.

6. Benchmark problem 3 – gas hydrate dissociation in a One-Dimensional Radial Domain

BP3 Champion: Mark White, PNNL.

BP3 involves the dissociation of natural gas hydrate via two conventional mechanisms; depressurization and thermal stimulation. Dissociation is affected by either lowering the pressure, via constant fluid removal, or increasing the temperature, via constant heat injection.

Unlike other problems in IGHCCS2, BP3 does not consider geo-mechanical coupling, but was a problem in the IGHCCS1 suite (Anderson et al., 2011a, 2011b; Wilder et al., 2008). Addressing this problem in IGHCCS2 allows a comparison with previous results, and serves to test the effects of spatial discretization. Fine spatial discretization is specified in BP3 to capture the characteristics of the dissociation front.

A unique feature of BP3 is its similarity solution: plots of state variables versus the similitude variable $\xi = r^2/t$, where r is the radius in this cylindrical model domain and t is time, yield a single solution (Doughty and Pruess, 1992; O'Sullivan, 1981). This type of solution arises from the radial domain and constant source driver of the problem and yields state parameters that, when plotted against the ratio r^2/t , should plot on a single curve from spatially distributed points at one point in time or single locations in space over distributed points in time. A schematic of this problem is shown in Fig. 24.

6.1. BP3 description

A one-dimensional radial compositional domain is specified with an outer radius of 1000 m and thickness of 1 m. Radially the domain is discretized in two sections. From $r = 0$ m to $r = 20$ m, a uniform spacing of 0.02 m is used and between $r = 20$ m to $r = 1000$ m, 1000 grid cells are used with a logarithmically distributed spacing, yielding a spacing of 0.0784 m for the inner-most radial grid cell of the outer 1000 grid cells. Hydrate, aqueous, and gas phases are assumed to occur and the porosity, intrinsic permeability and relative permeability of the porous media are assumed to follow the original porous medium (OPM) model (Moridis et al., 2005). The OPM model considers the porous medium to be unaltered by the solid hydrate phase and phase relative permeability is solely dependent on the mobile phase saturation. Gas and aqueous relative permeability were defined by the Stone (1970) and Aziz (Aziz and Settari, 1979) models, respectively. The pore space is assumed to be occupied with mobile and immobile phases: the gas and aqueous phase are mobile phases and hydrate and ice are immobile. Given the initial conditions, ice is not expected to form in this problem, however. The relationship between aqueous saturation and capillary pressure (i.e., $P_{cap} = P_g - P_w$) is expressed via the van Genuchten function (van Genuchten, 1980), with the aqueous saturation scaled by the mobile phase saturations (i.e., $s_{w,e} = s_w/(s_w + s_g)$). This approach accounts for the effects of the immobile phases. Problem specifics differed between the thermal stimulation and depressurization cases and are given below in six categories: 1) initial conditions, 2) boundary conditions, 3) hydraulic properties, 4) thermal properties, 5) relative permeability, 6) capillary pressure, 7) output. Details are shown in Table 8 for the six categories.

6.2. BP3 simulation results and comparisons

Solutions for BP3 were submitted by ten teams: GEOMAR, JLU, LBNL, LLNL-Tongji, NETL, PNNL, SNL, UCB, Ulsan-KIGAM, and UT. As all simulation results followed the characteristics of a similarity

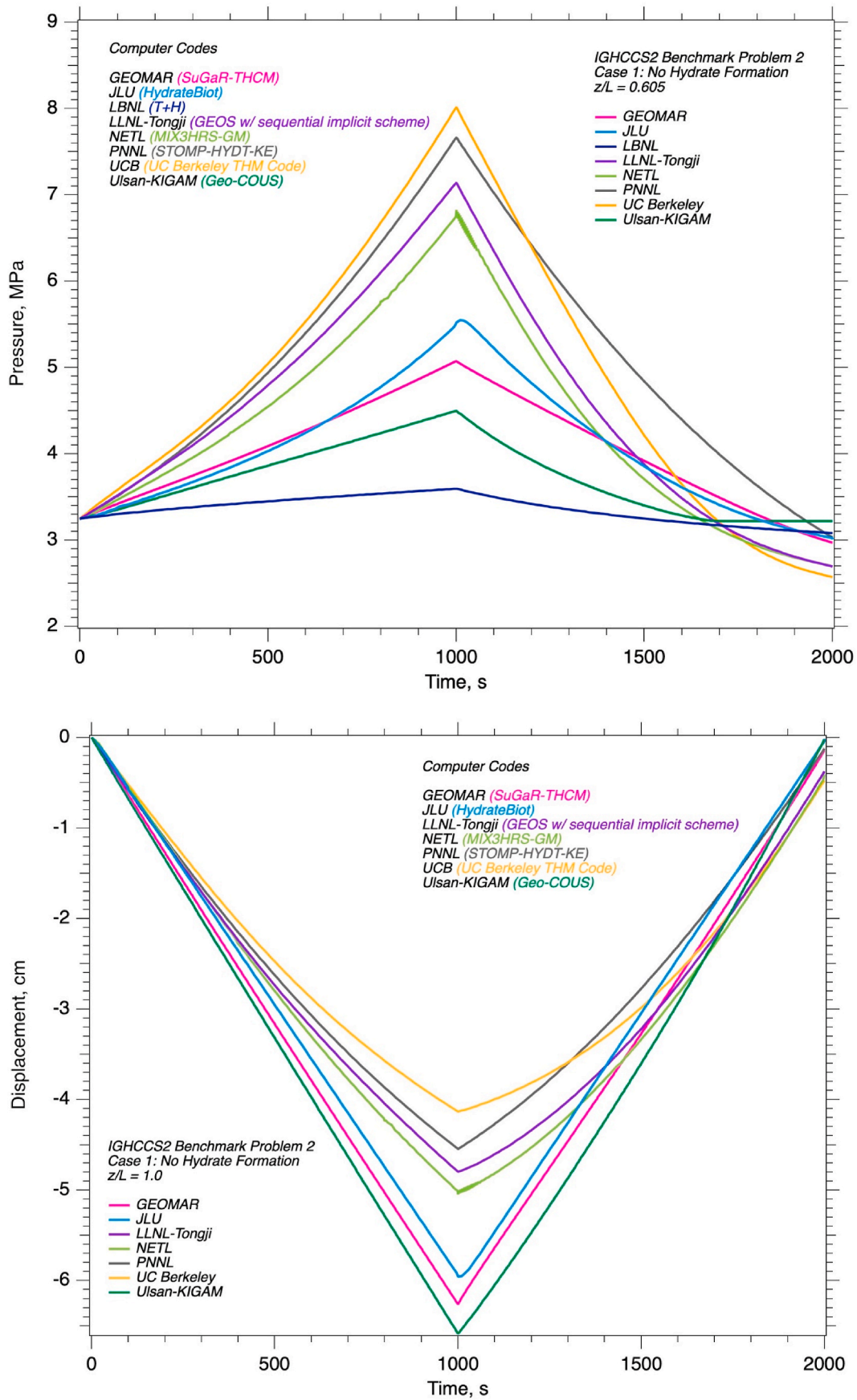


Fig. 10. Comparison of numerical solutions for BP2 Case1 from different codes. Plotted profiles: Pressure at $z/L = 0.605$ and z -displacement at $z/L = 1.0$.

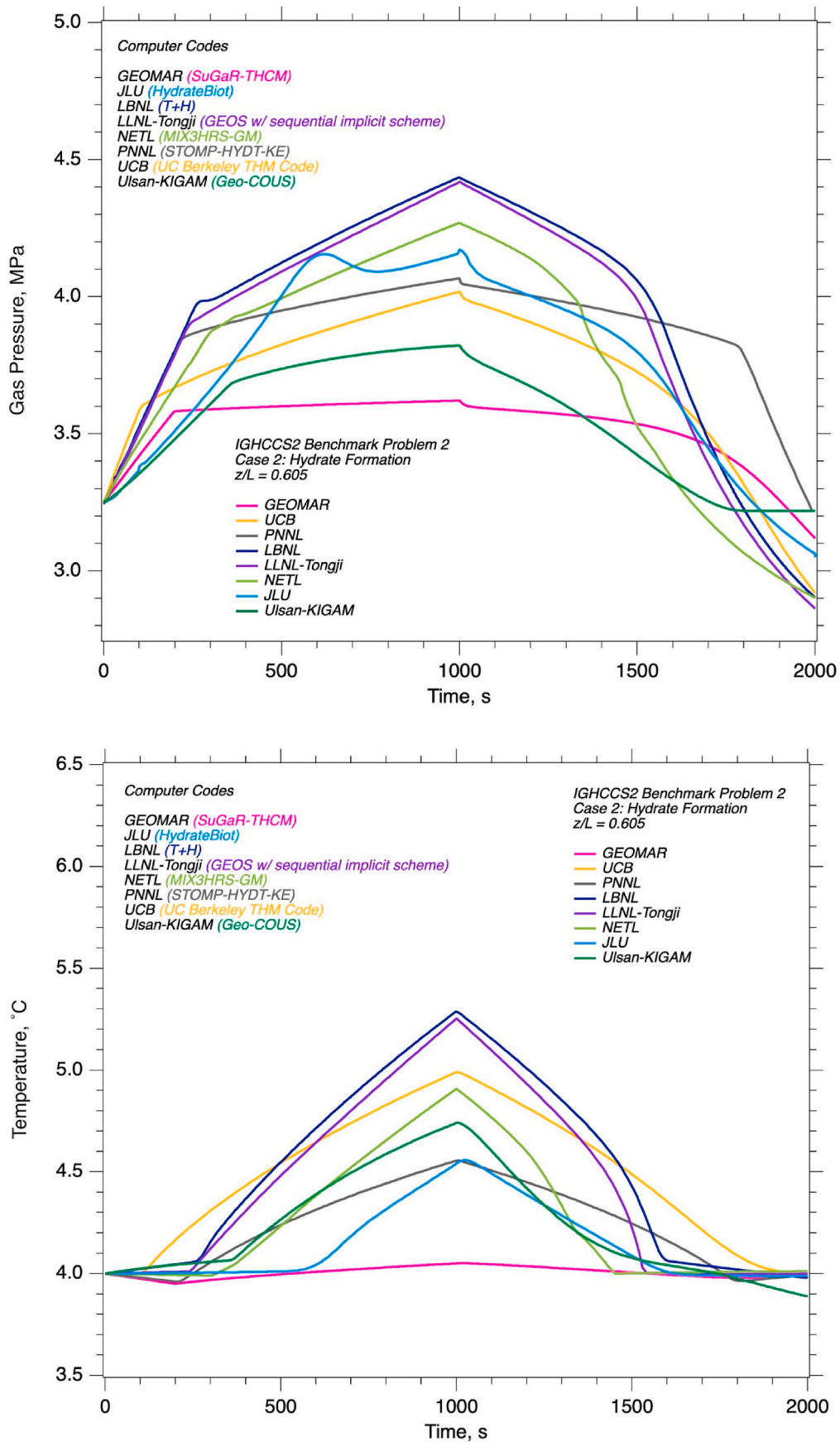


Fig. 11. Comparison of numerical solutions for BP2 Case 2 from different codes. Plotted profiles: Pressure at $z/L = 0.605$ and temperature at $z/L = 0.605$.

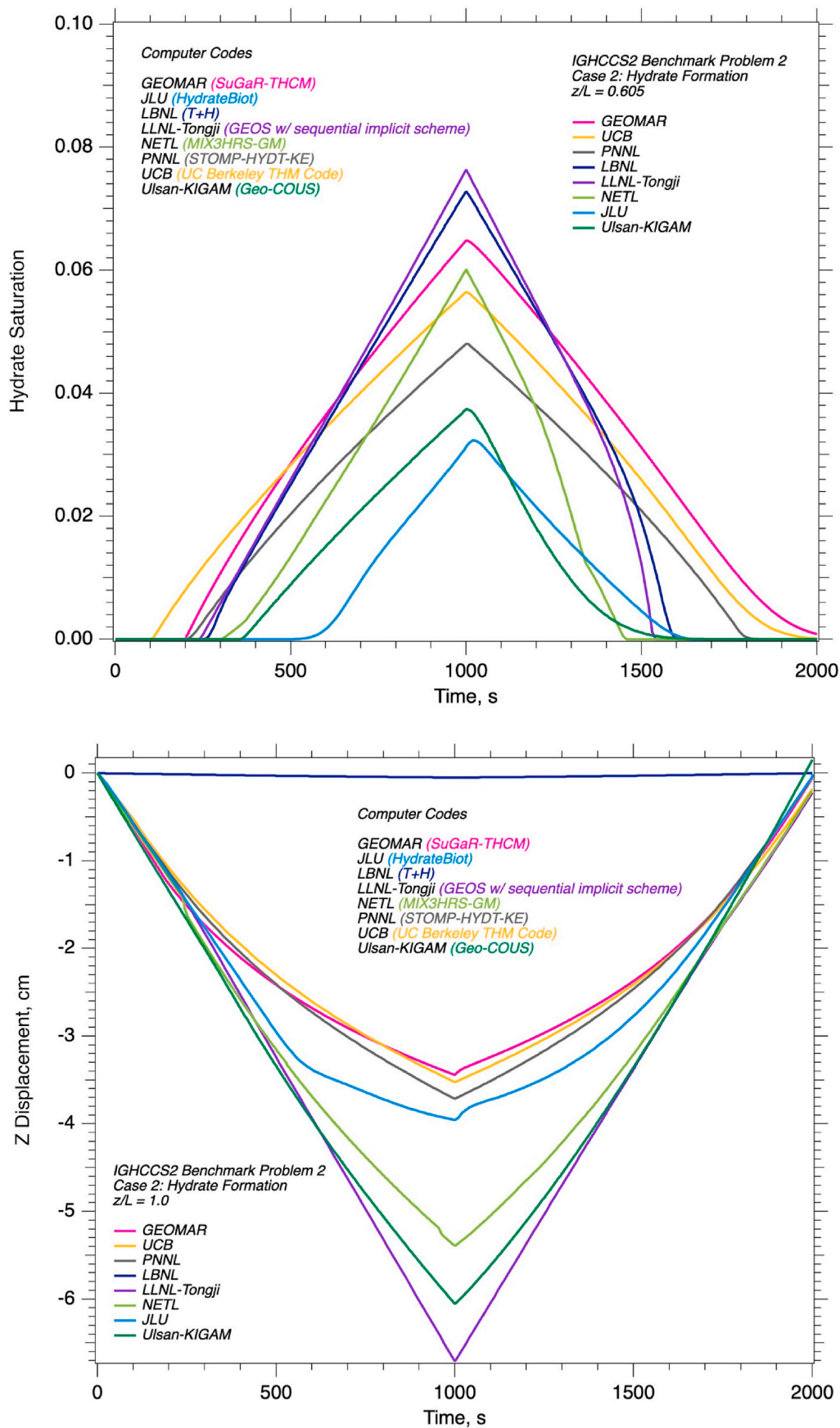


Fig. 12. Comparison of numerical solutions for BP2 Case2 from different codes. Plotted profiles: Hydrate saturation at $z/L = 0.605$ and z -displacement at $z/L = 1.0$.

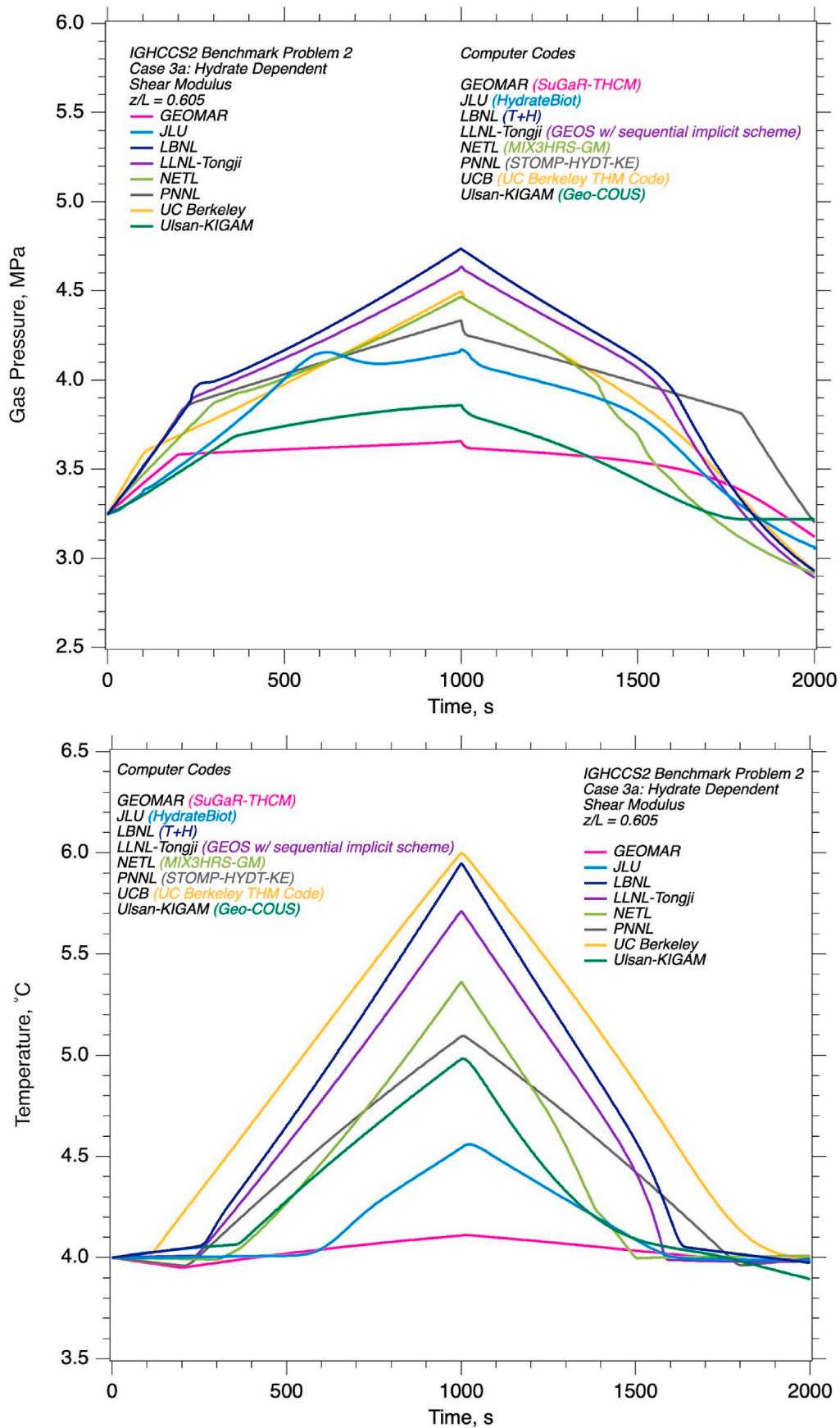


Fig. 13. Comparison of numerical solutions for BP2 Case 3a from different codes. Plotted profiles: Pressure at $z/L = 0.605$ and temperature at $z/L = 0.605$.

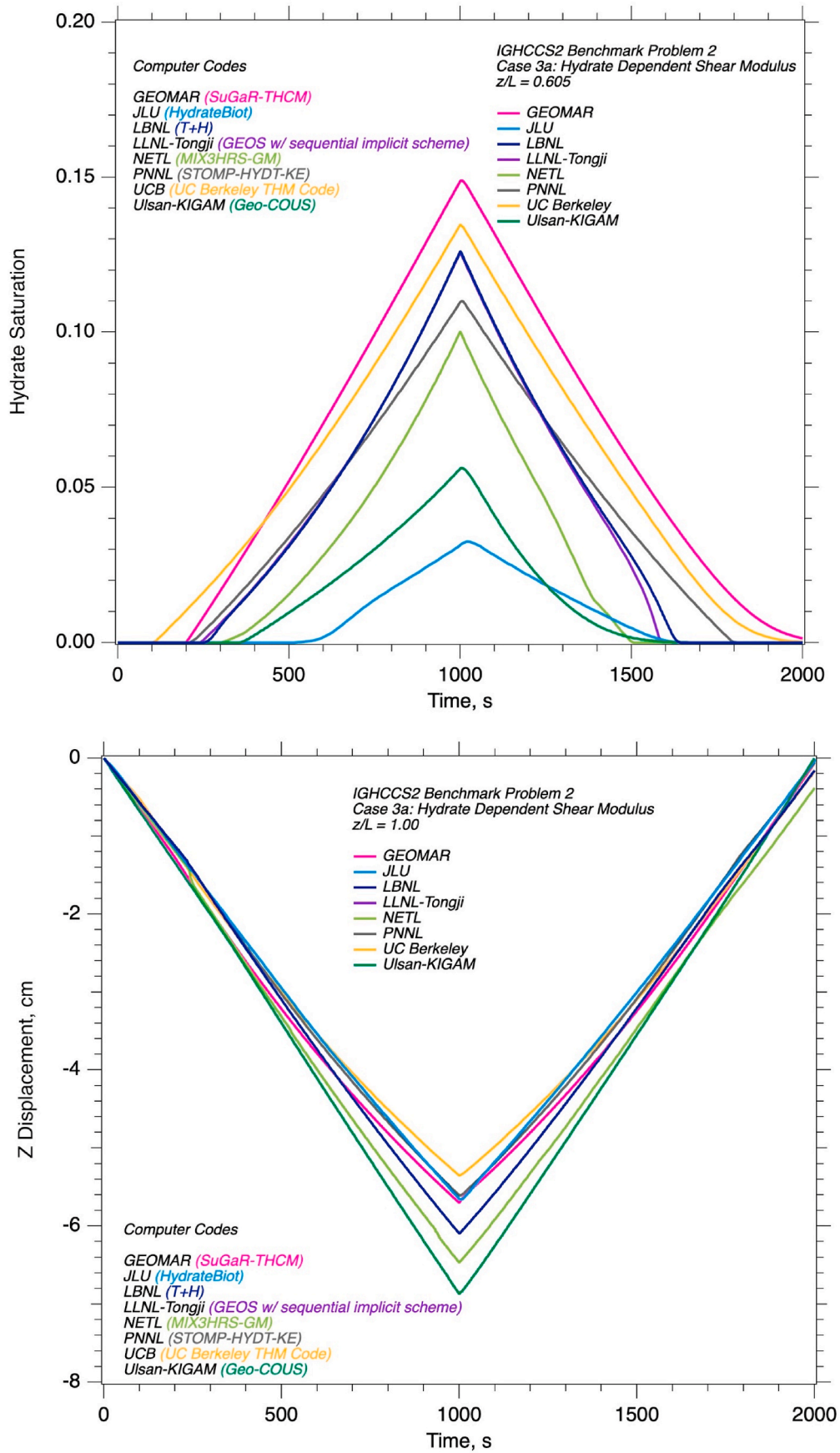


Fig. 14. Comparison of numerical solutions for BP2 Case 3a from different codes. Plotted profiles: Hydrate saturation at $z/L = 0.605$ and z -displacement at $z/L = 1.0$.

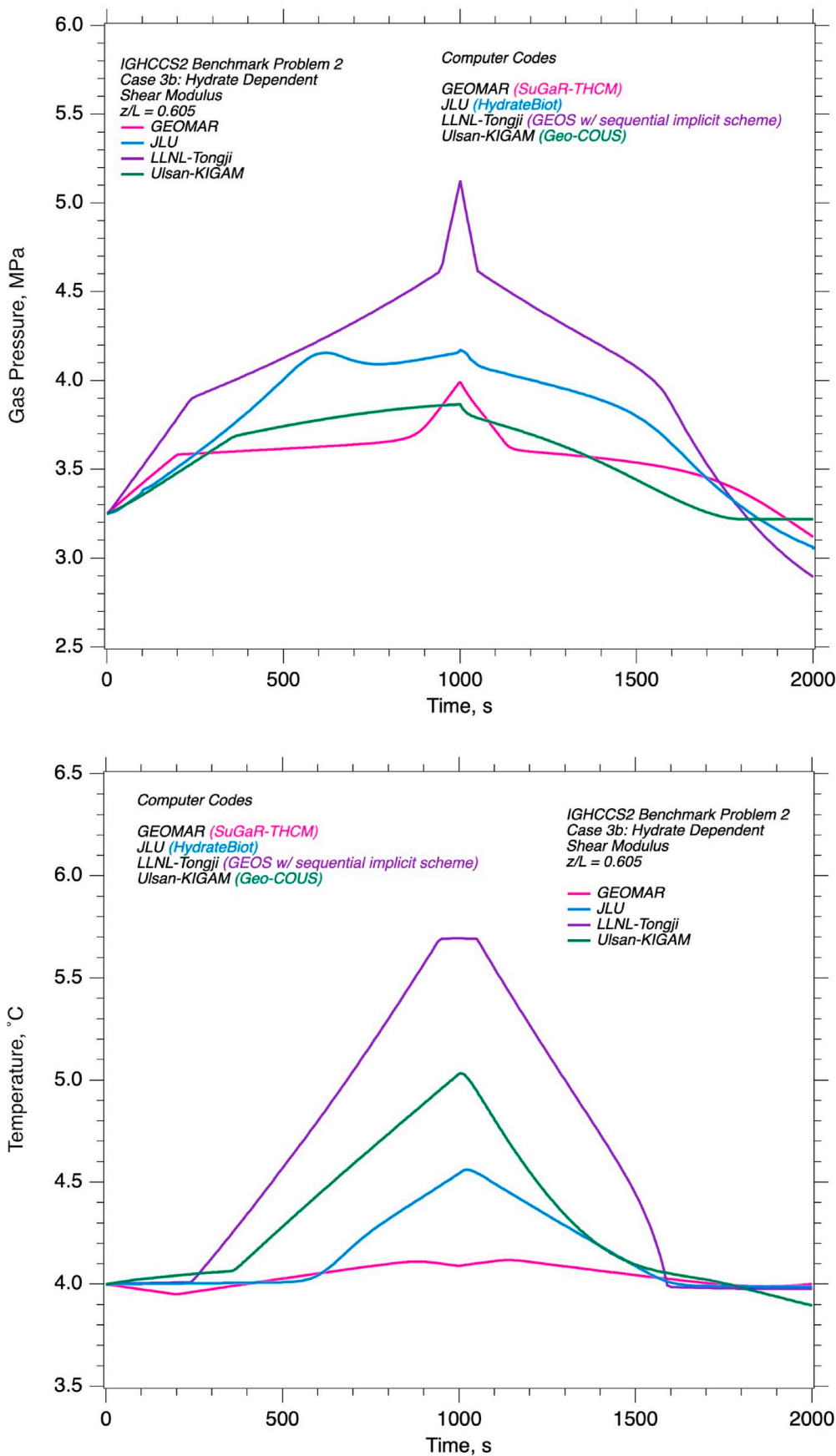


Fig. 15. Comparison of numerical solutions for BP2 Case 3b from different codes. Plotted profiles: Pressure at $z/L = 0.605$ and temperature at $z/L = 0.605$.

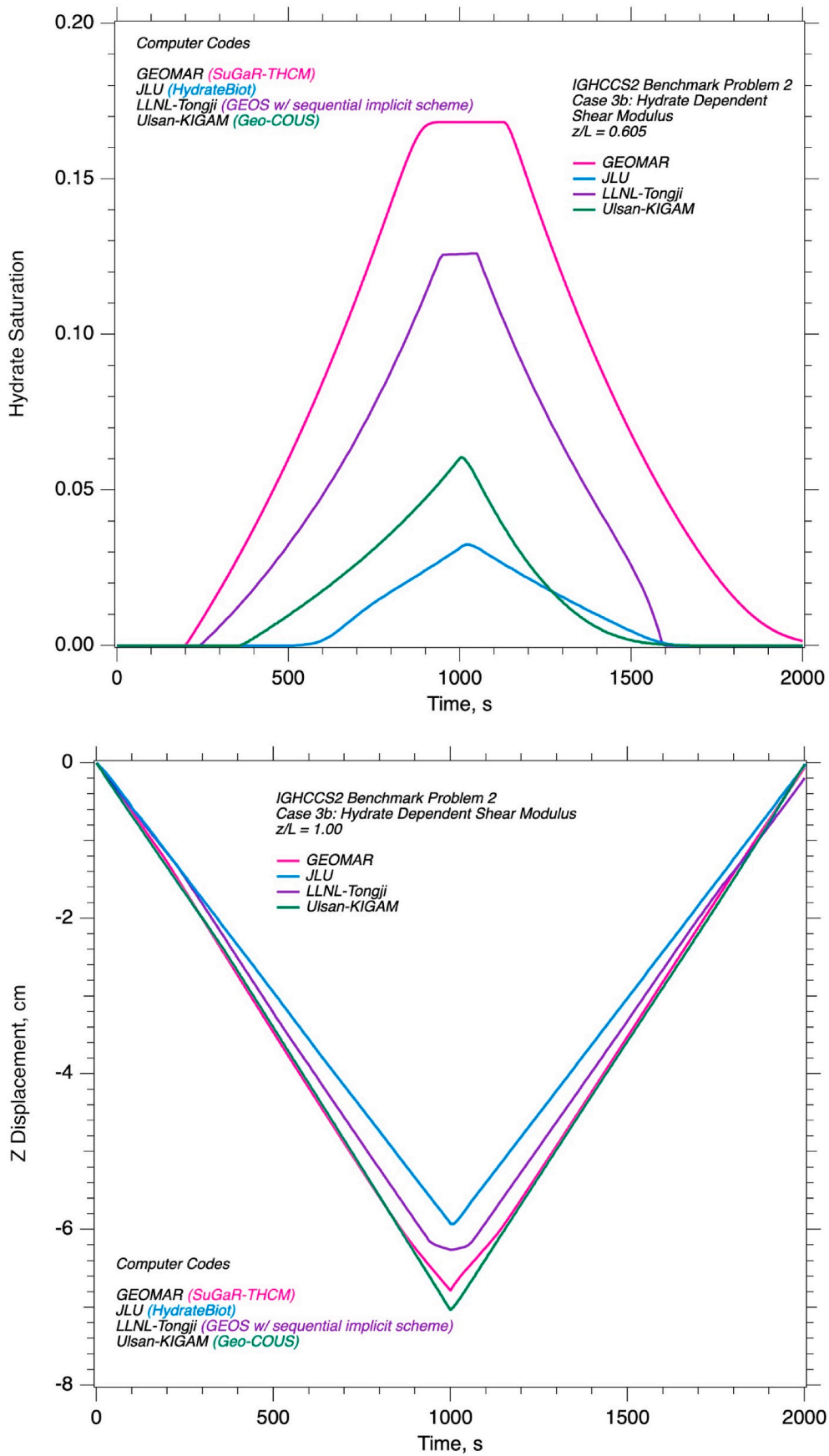


Fig. 16. Comparison of numerical solutions for BP2 Case 3b from different codes. Plotted profiles: Hydrate saturation at $z/L = 0.605$ and z -displacement at $z/L = 1.00$.

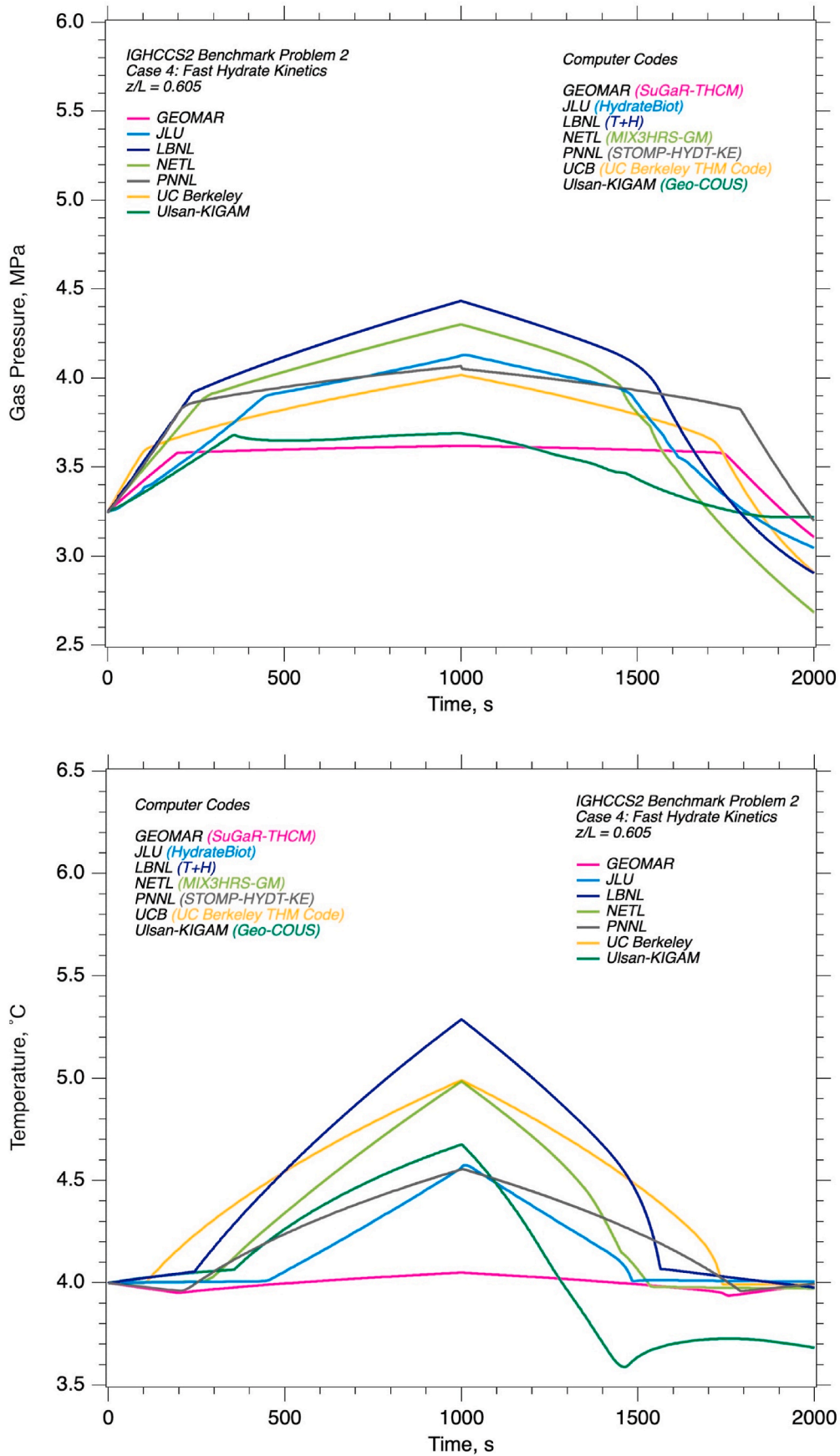


Fig. 17. Comparison of numerical solutions for BP2 Case 4 from different codes. Plotted profiles: Pressure at $z/L = 0.605$ and temperature at $z/L = 0.605$.

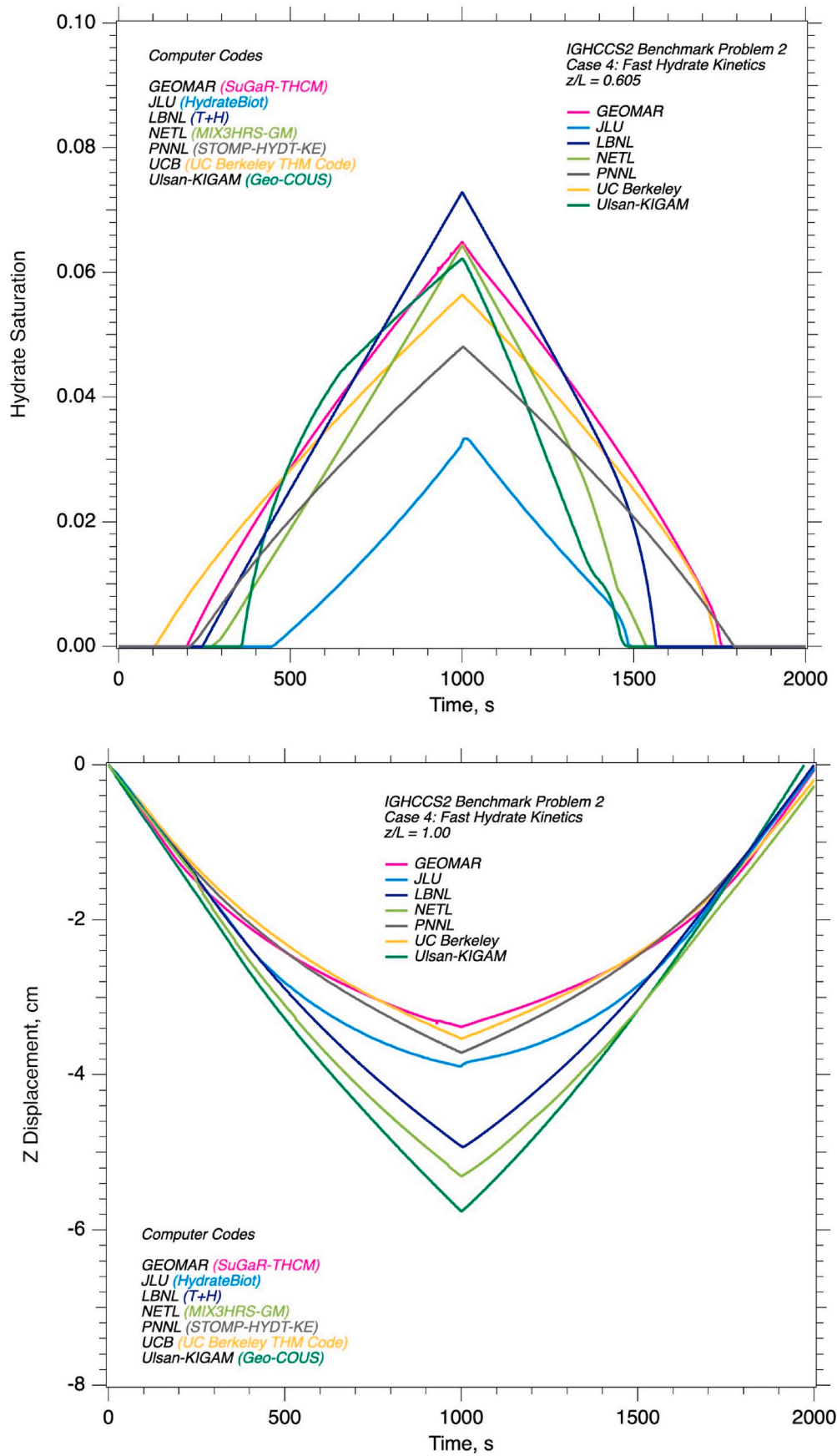


Fig. 18. Comparison of numerical solutions for BP2 Case 4 from different codes. Plotted profiles: Hydrate saturation at $z/L = 0.605$ and z -displacement at $z/L = 1.0$.

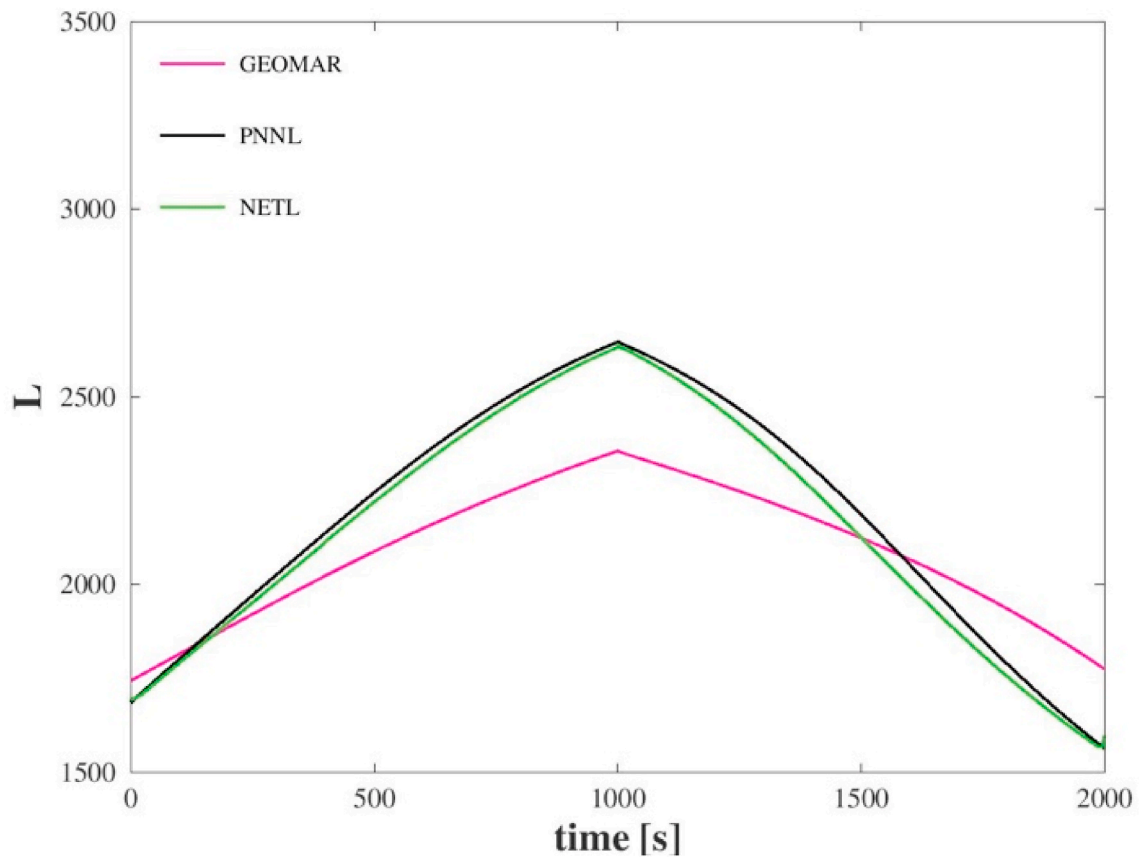
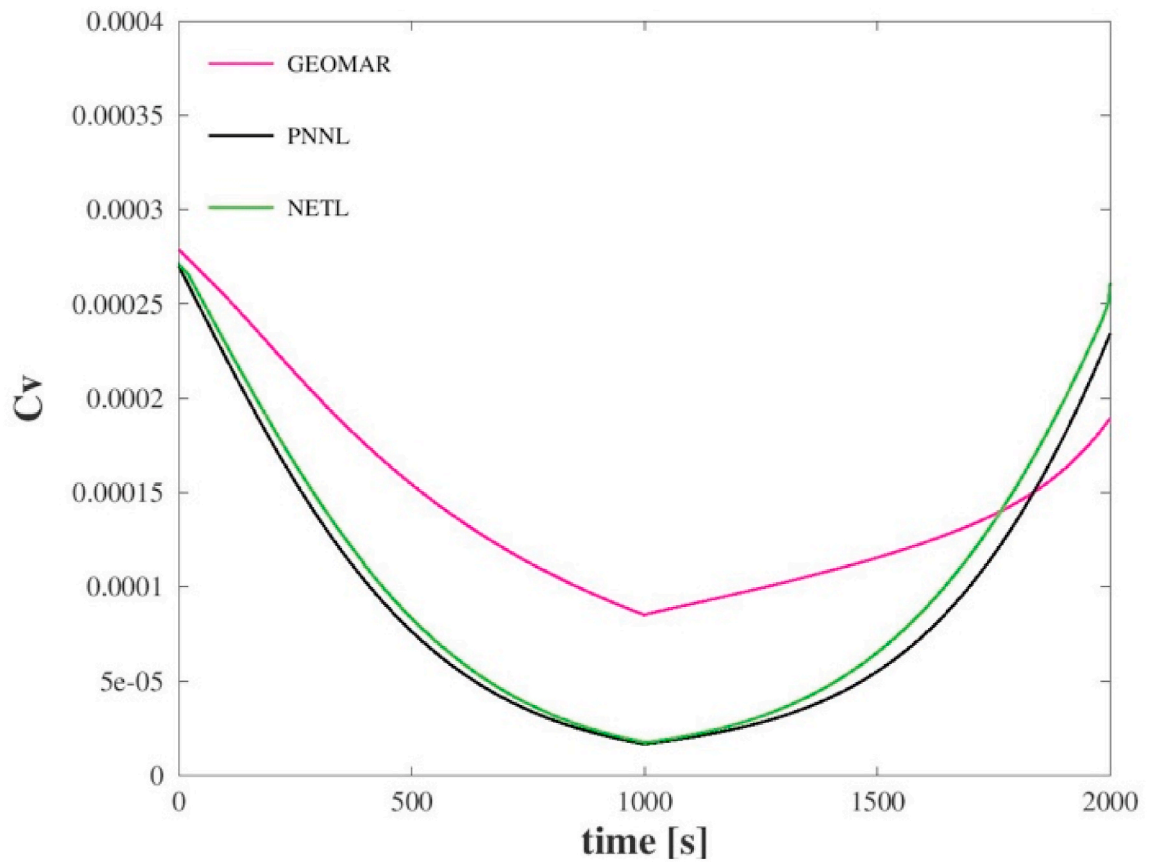


Fig. 19. Evolution of C_v and \mathcal{L} parameters for the GEOMAR, PNNL, and NETL solutions for BP2 Case 1.

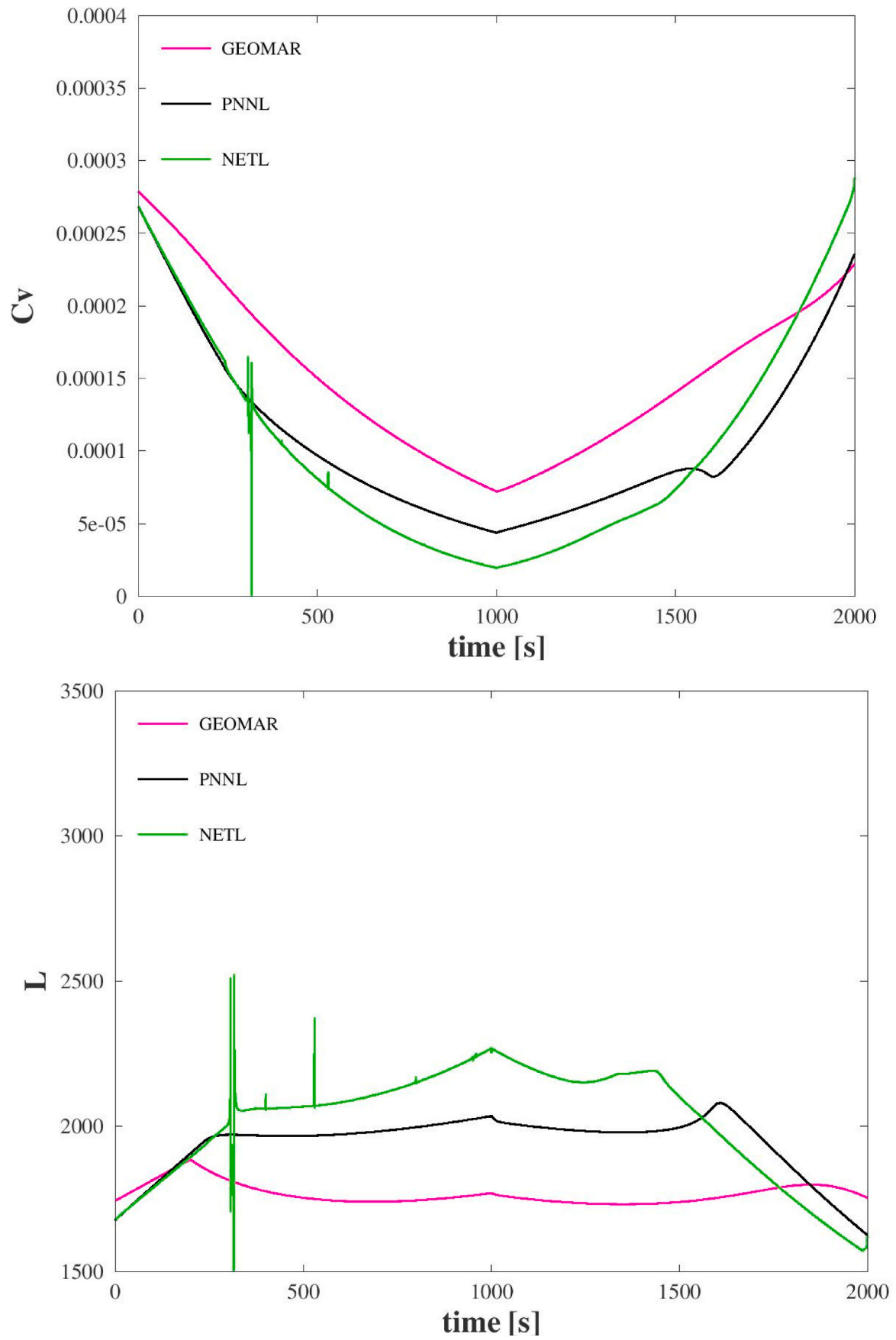


Fig. 20. Evolution of C_v and L parameters for the GEOMAR, PNNL, and NETL solutions for BP2 Case 2.

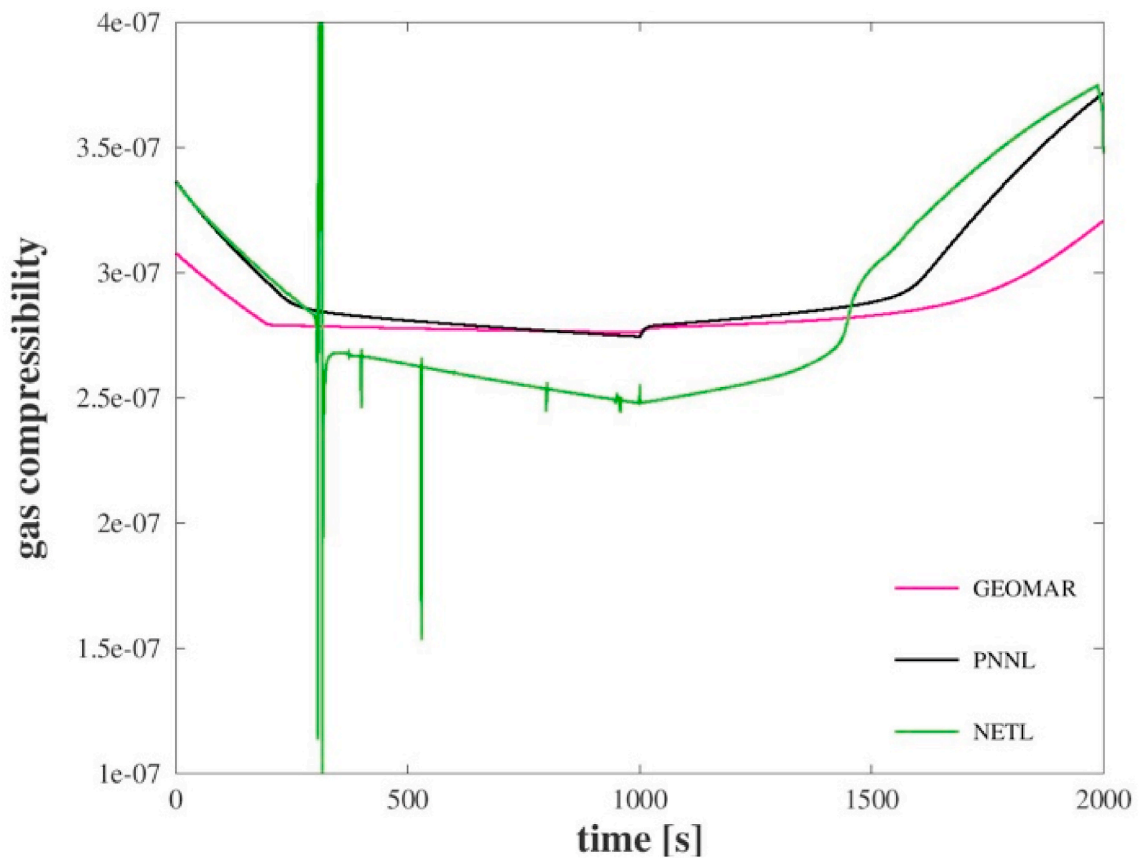
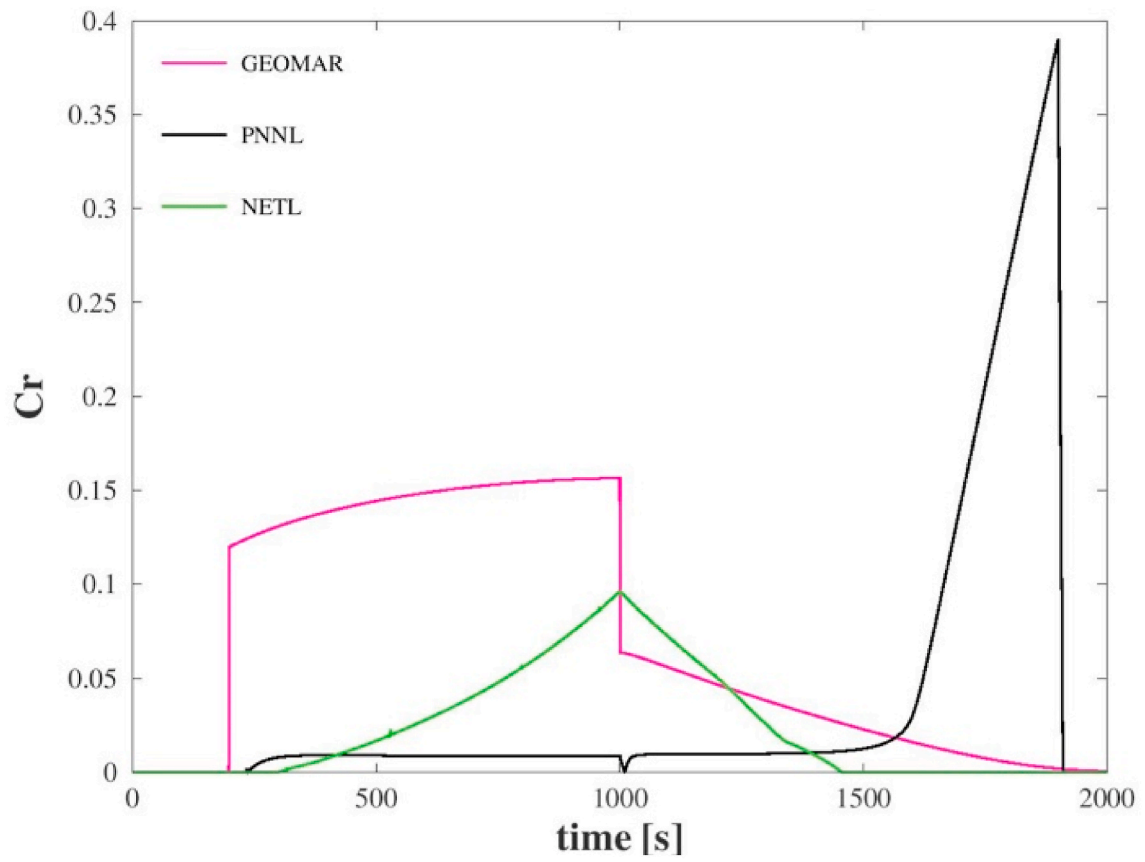


Fig. 21. Evolution of C_r and C_g parameters for the GEOMAR, PNNL, and NETL solutions for BP2 Case 2.

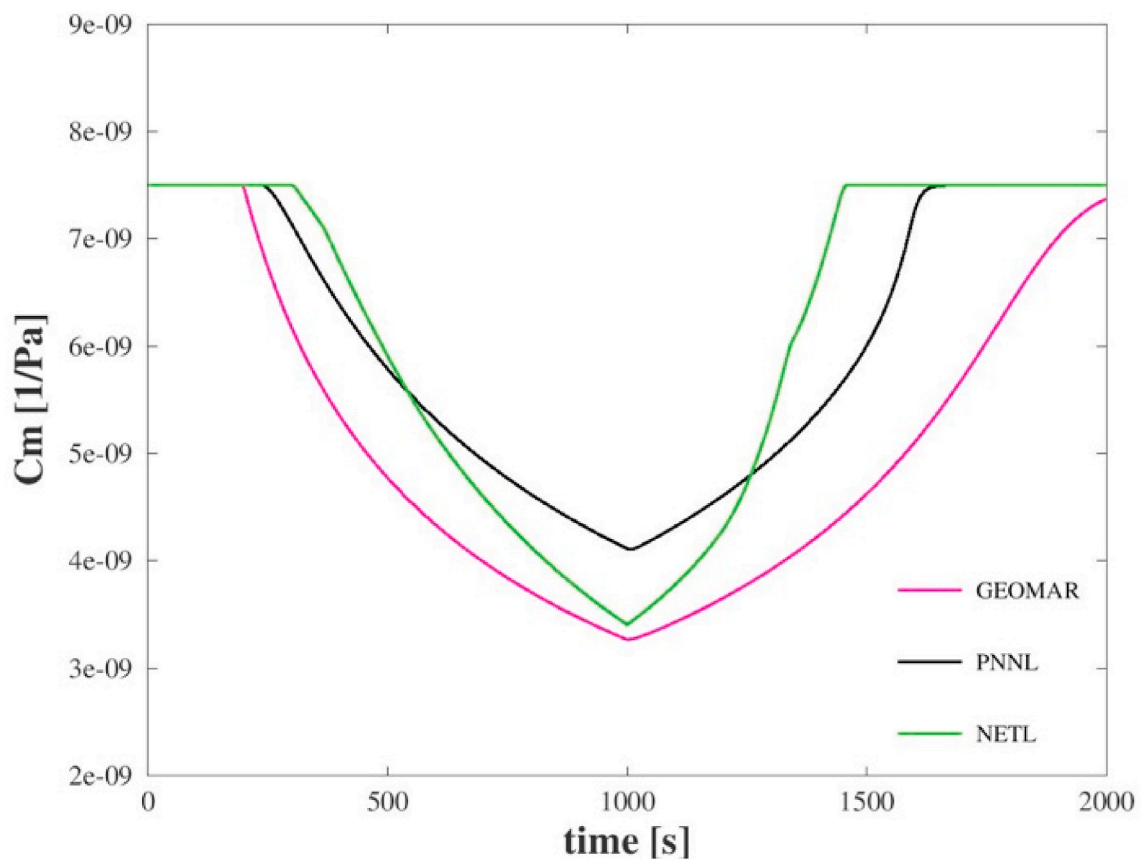
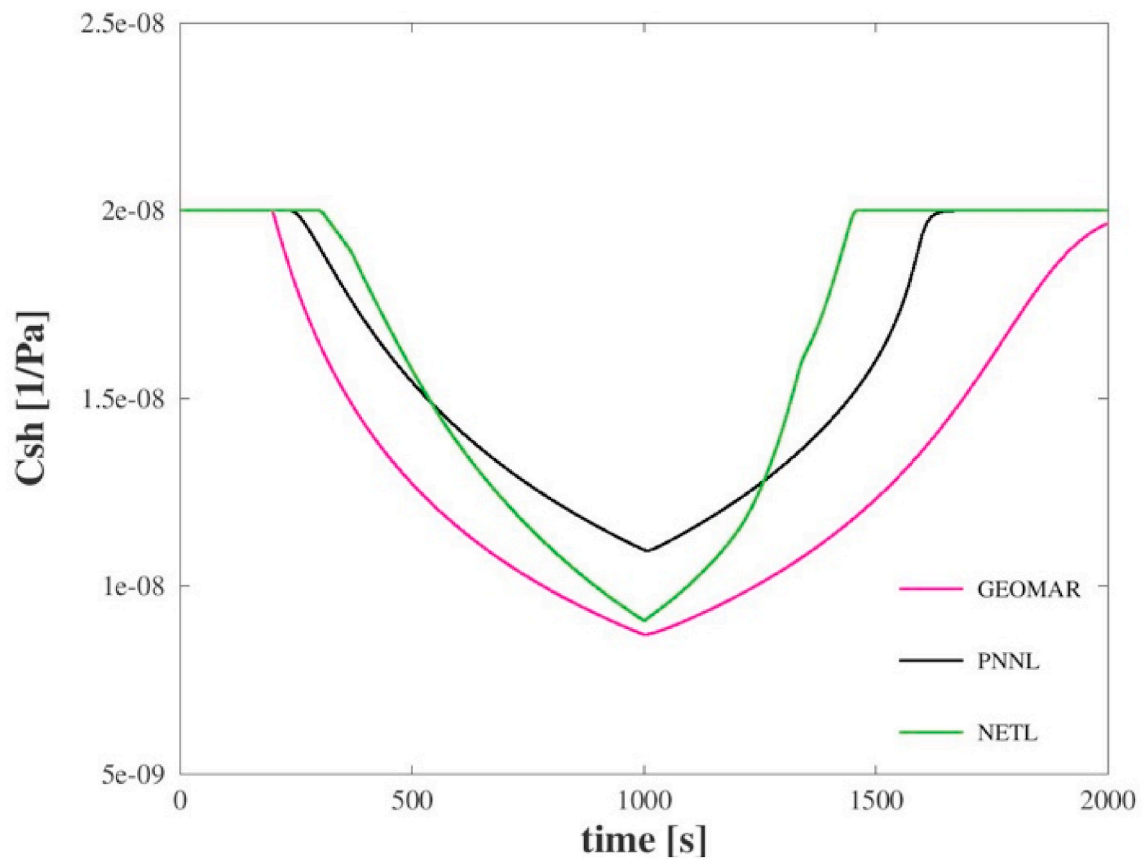


Fig. 22. Evolution of C_{sh} and C_m parameters for the GEOMAR, PNNL, and NETL solutions for BP2 Case 2.

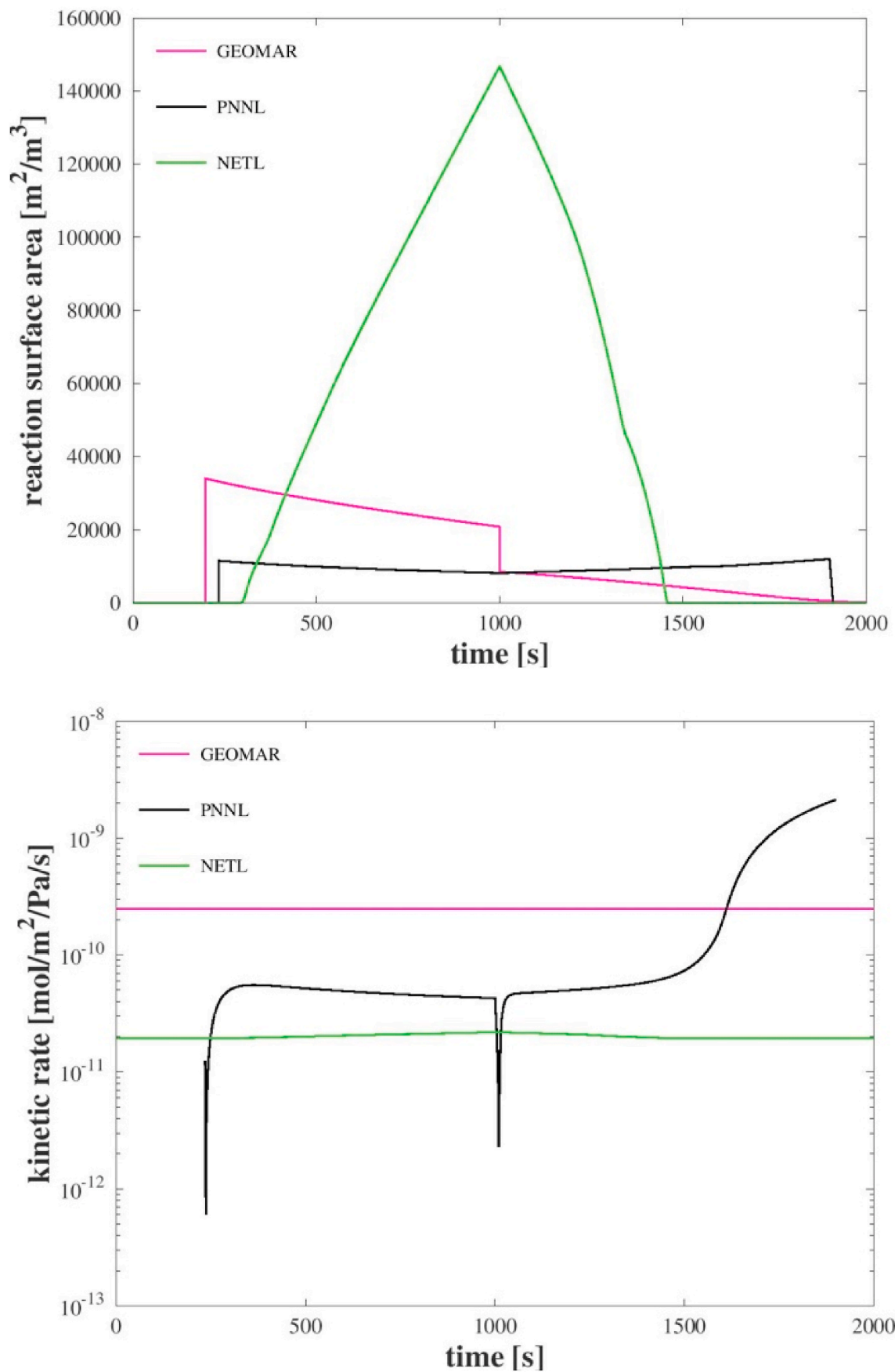


Fig. 23. Evolution of A_s and k' parameters for the GEOMAR, PNNL, and NETL solutions for BP2 Case 2.

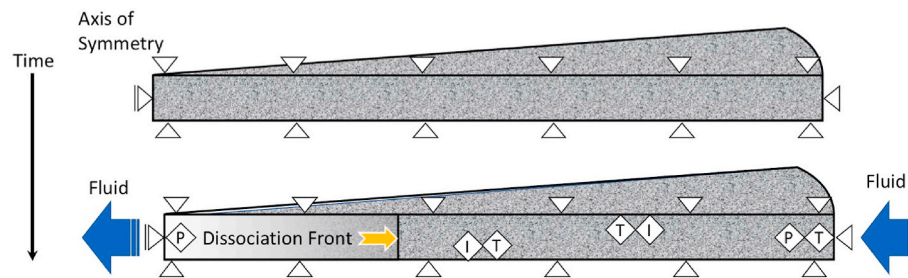


Fig. 24. Conceptual schematic of BP3, with triangles indicating a fixed strain boundary, T indicating a temperature boundary, P indicating a pressure boundary, and I indicating an impermeable boundary. Fluid flow (blue arrows) is toward the production well. (For interpretation of the references to colour in this figure legend, the reader is referred to the Web version of this article.)

solution, comparisons were only made at a single point in time (30 days) for both the thermal stimulation and depressurization cases. The problem description for IGHCCS1 included output of the mass rate of CH_4 released from the hydrate and produced at the well, but for IGHCCS2 those were not included, as proper calculation of CH_4 release rates are reflected in the state variables versus the similitude variable.

6.2.1. BP3 case 1 - thermal stimulation

Production of gas from hydrate under the thermal-stimulation case proceeded via dissociation with the addition of 150 W of heat at the center, generally accomplished numerically as a heat source applied to the inner-most radial grid cell/node. The heat source increases the temperature of the hydrate bearing sediment above the hydrate equilibrium point, dissociating the hydrate to produce water and CH_4 and elevated pressures at the dissociation front. The dissociation front was predicted to be sharp, as shown in the plots of hydrate saturation versus similitude variable (Fig. 25), and occurs generally near $r^2/t = 0.045 \text{ m}^2/\text{day}$. Temperatures around the dissociation front are nearly constant, as expected for a system undergoing a phase transition (Fig. 26). The precise location of the dissociation front varies between simulators, but there is good correspondence across all the simulators between the zone of constant temperature and the dissociation region. The temperature plot demonstrates a difficulty associated with thermal stimulation as a production strategy for natural gas hydrate production using a single well, namely that radial temperature gradients are required to maintain an outward expanding dissociation front, requiring the heating of a radially increasing volume of rock with time.

The inner radial boundary is closed for the thermal stimulation case, which results in migration of the released water and CH_4 outward, creating a zone of secondary hydrate formation, generally between $r^2/t = 0.045$ and $0.15 \text{ m}^2/\text{day}$ (Fig. 25). The pore space behind the dissociation front is occupied with aqueous and gas phases, and devoid of gas hydrate. Differences in phase saturation ratios were noted amongst the simulators, as shown in the plot of aqueous saturation versus similitude variable (Fig. 27). Overall the various simulators show good agreement in results, with some exceptions. The oscillations in hydrate saturation versus similitude variable are generally more prevalent for codes that assume thermodynamic equilibrium conditions, versus those that use a nonequilibrium or kinetic approach.

6.2.2. BP3 case 2 - depressurization

Production of gas from hydrate under the depressurization case proceeded via dissociation with the removal of fluids from the central well at a rate of 0.1 kg/s. As the removal rate is not specific about the composition of removed fluids, this becomes a computed quantity. Initially only aqueous phase is removed with any dissolved CH_4 , but after dissociation starts both aqueous and gas phases are removed. A common assumption taken to determine the relative amounts of removed fluids is to base the removal fractions on relative mobilities of the fluids, where mobility is defined by k_r/μ . As with the thermal stimulation case, the simulators generally demonstrated similarity

solution characteristics in the results, and results at 30 days used for comparison and discussion. Unlike the thermal stimulation case, depressurization yields a hydrate dissociation zone between $r^2/t = 0.04$ and $400.0 \text{ m}^2/\text{day}$, as shown in the plot of hydrate saturation versus similitude variable (Fig. 28). Most of the CH_4 released during dissociation occurs as gas, due to the relatively low solubility of CH_4 in water. Correspondingly, the gas saturation extends from the central well to the outer radial distance of the hydrate dissociation zone (Fig. 29). Depressurization of gas hydrate bearing sediment yields hydrate dissociation, but also a temperature drop due to the endothermic hydrate dissociation. For field-scale cases the temperature drop can be sufficient to reestablish hydrate stability conditions, in which case dissociation is limited by heat transfer from outside the dissociation zone. For this one-dimensional radial problem, the only source of heat is from radial conduction and fluid being drawn into the dissociation zone. Whereas this problem involves radial flow driven by fluid removal from a central well, comparison of the temperature results across the codes shows excellent agreement (Fig. 30). Included on this plot is the mean temperature of clustered solutions. Plots of system pressure versus the similitude variable show more scatter across the codes, but the trends are similar (Fig. 31). The equilibrium pressure computed from CSMGem (Lafond et al., 2012) associated with the average temperature in the temperature plot (Fig. 30) defines the three hydrate dissociation zones. At similitude variables values below $r^2/t = 0.04 \text{ m}^2/\text{day}$ pressures are generally below the equilibrium curve and the hydrate has been dissociated, at values between $r^2/t = 0.04$ and $400.0 \text{ m}^2/\text{day}$ hydrate dissociation is occurring and the pressures trend along the equilibrium curve, and at values above $r^2/t = 400.0 \text{ m}^2/\text{day}$ pressures are above the equilibrium curve and the hydrate is intact. Variance in pressure across the codes may be due to the representation of the equilibrium function.

6.3. BP3 outcomes

BP3 examines the production of natural gas from hydrates using thermal stimulation and depressurization. The problem is devoid of geomechanical coupling and involves a one-dimensional radial coordinate system, the fine discretization allows for the resolution of the hydrate dissociation front. The radial homogeneous domain and constant source terms for both the thermal stimulation and depressurization cases yield similarity solutions, such that state variables computed at single points in space over time or at single points in time over all space should collapse to a single curve when plotted against the similitude variable $\xi = r^2/t$. This feature of BP3 makes it valuable for evaluating the accuracy of a numerical simulator in predicting hydrate dissociation/formation and transport processes. BP3 additionally makes use of the original porous media model, which eliminates the coupling of hydrate saturation and effective permeability (i.e., reduction of intrinsic permeability with hydrate saturation). For the STOMP-HYDT-KE simulator the default model is the Civan permeability model (Civan, 2004), which alters the effective permeability with hydrate saturation. Application of the Civan model in STOMP-HYDT-KE resulted in lower

Table 8
BP3 problem specifications.

Initial Conditions		
	Thermal Stimulation	Depressurization
Pressure	$P = 4.6\text{MPa}$	$P = 9.5\text{MPa}$
Temperature	$T = 3^\circ\text{C}$	$T = 12^\circ\text{C}$
Hydrate Saturation	$s_h = 0.5$	$s_h = 0.4$
Aqueous Saturation	$s_w = 0.5$	$s_w = 0.6$
Gas Saturation	$s_g = 0.0$	$s_g = 0.0$
Boundary Conditions		
	Thermal Stimulation	Depressurization
$r = 0\text{ m}$	heat input = 150 W	mass removal rate = 0.1 kg/s
$r = 1000\text{ m}$	$P = 4.6\text{MPa}$ $T = 3^\circ\text{C}$ $s_h = 0.5$ $s_w = 0.5$ $s_g = 0.0$	$P = 9.5\text{MPa}$ $T = 12^\circ\text{C}$ $s_h = 0.4$ $s_w = 0.6$ $s_g = 0.0$
Hydraulic Properties		
	Thermal Stimulation	Depressurization
Intrinsic Permeability	$k = 10^{-12}\text{m}^2(1D)$	$k = 3 \times 10^{-13}\text{m}^2(0.3D)$
Porosity	$\phi = 0.3$	$\phi = 0.3$
Pore Compressibility	$\beta_\phi = 10^{-9}\text{ 1/Pa}$	$\beta_\phi = 10^{-9}\text{ 1/Pa}$
Grain Density	$\rho_s = 2600\text{ kg/m}^3$	$\rho_s = 2600\text{ kg/m}^3$
Thermal Properties		
	Thermal Stimulation	Depressurization
Grain Specific Heat	$c_{p,s} = 1000\frac{\text{W}}{\text{kg K}}$	$c_{p,s} = 1000\frac{\text{W}}{\text{kg K}}$
Dry Thermal Conductivity	$k_{dry}^T = 2.0\frac{\text{W}}{\text{m K}}$	$k_{dry}^T = 2.0\frac{\text{W}}{\text{m K}}$
Pore Compressibility	$k_{wet}^T = 2.18\frac{\text{W}}{\text{m K}}$	$k_{wet}^T = 2.18\frac{\text{W}}{\text{m K}}$
Composite Thermal Conductivity Model	$k = k_{dry}^T + \phi (s_l k_{wet}^T + s_h k_h^T + s_i k_i^T + s_g k_g^T)$	
Relative Permeability		
	Thermal Stimulation	Depressurization
Exponent	$n = 3.0$	$n = 3.0$
Gas Residual Saturation	$s_{gr} = 0.02$	$s_{gr} = 0.02$
Aqueous Residual Saturation	$s_{wr} = 0.12$	$s_{wr} = 0.12$
Gas Relative Permeability Model	$k_g^r = \left(\frac{s_g - s_{gr}}{1 - s_{wr}}\right)^n$	
Aqueous Relative Permeability Model	$k_w^r = \left(\frac{s_w - s_{wr}}{1 - s_{wr}}\right)^n$	
Capillary Pressure		
	Thermal Stimulation	Depressurization
Exponent	$\lambda = 0.45$	$\lambda = 0.45$
Entry Pressure	$P_o = 1.25 \times 10^4\text{ Pa}$	$P_o = 1.25 \times 10^4\text{ Pa}$
Aqueous Residual Saturation	$s_{wr} = 0.12$	$s_{wr} = 0.12$
Capillary Pressure Model	$P_{cap} = P_o \left[\frac{s_w - s_{wr}}{1 - s_{wr}} \right]^{-\frac{1}{\lambda}} - 1$	
Output		
Pressure (MPa)	Temperature ($^\circ\text{C}$)	Aqueous Saturation
Gas Saturation	Hydrate Saturation	Aqueous Relative Permeability
Gas Relative Permeability	CH_4 Aqueous Mass Fraction	
Thermal Stimulation	$t = 2, 5, 10, 20, 30, 60\text{ days}$	
Depressurization	$t = 2, 5, 10, 20, 30\text{ days}$	

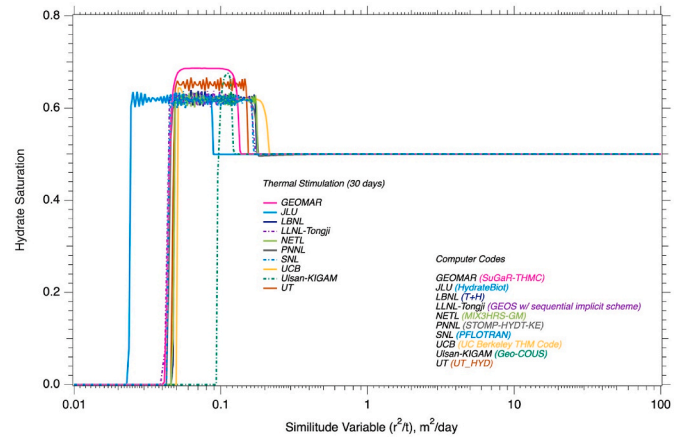


Fig. 25. Numerical simulations for BP3 Case 1 – Thermal Stimulation, showing hydrate saturation versus similitude variable.

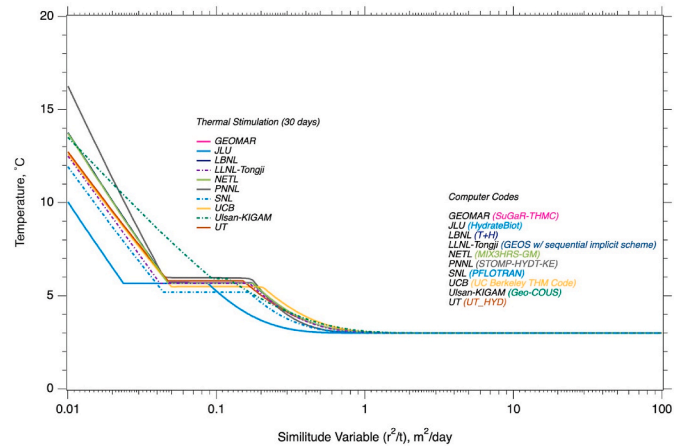


Fig. 26. Numerical simulations for BP3 Case 1 – Thermal Stimulation, showing temperature versus similitude variable.

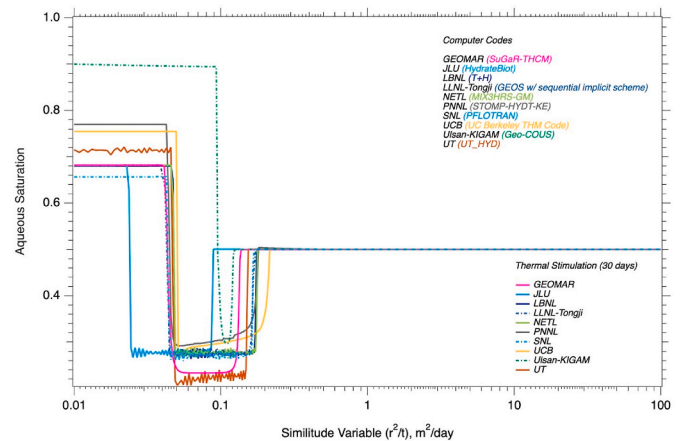


Fig. 27. Numerical simulations for BP3 Case 1 – Thermal Stimulation, showing aqueous saturation versus similitude variable.

pressure profiles for the depressurization case.

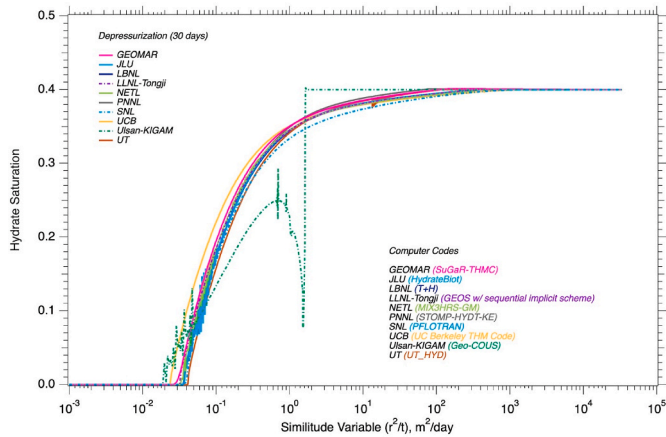


Fig. 28. Numerical simulations for BP3 Case 2 – Depressurization, showing hydrate saturation versus similitude variable.

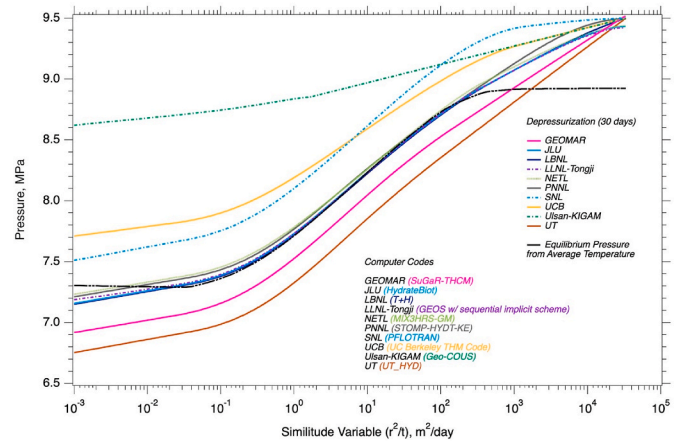


Fig. 31. Numerical simulations for BP3 Case 2 – Depressurization, showing pressure versus similitude variable.

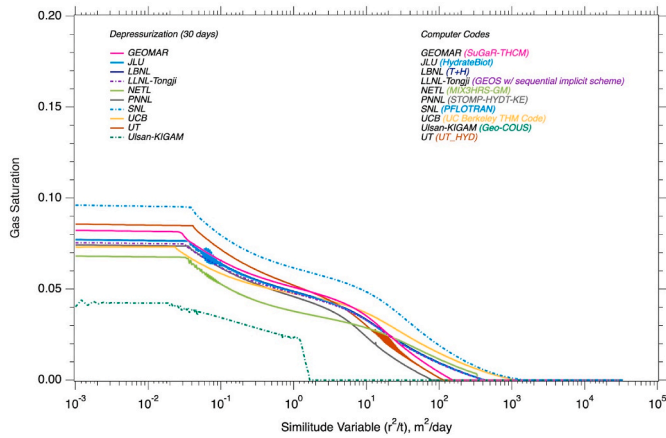


Fig. 29. Numerical simulations for BP3 Case 2 – Depressurization, showing gas saturation versus similitude variable.

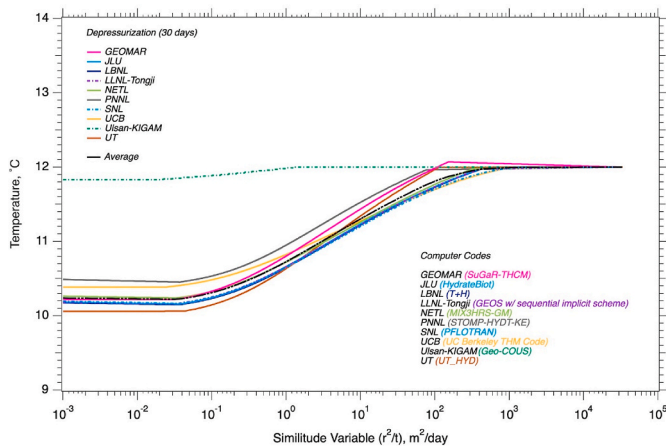


Fig. 30. Numerical simulations for BP3 Case 2 – Depressurization, showing temperature versus similitude variable.

7. Benchmark problem 4 – Radial Production with geomechanics

BP4 Champions: Matt Reagan and Alejandro Queiruga, LBNL.

Using radially symmetric domains is an efficient way to simulate vertical production well problems. We make use of that efficiency to

focus on the problem of incorporating geomechanics into a depressurization-style gas hydrate simulation, but also to generate an analytical solution with which to compare the results. BP4 comprises two production cases, one without gas hydrate (Case 1), and one with gas hydrate (Case 2). Both cases involve coupled flow and geomechanics within a one-dimensional radially symmetric domain. An analytical solution is available for Case 1, but not for Case 2. Small pressure changes were imposed in the Case 1 to minimize computational non-linearities and allow us to assess each model’s fundamental handling of the geomechanical aspects of problem. A schematic of this problem is shown in Fig. 32.

7.1. BP4 description

The problem domain of BP4 (Fig. 33) uses a mesh is similar to that of BP3, but extended to 5000 m. The true problem domain needed for analytical analysis extends infinitely, but is truncated for numerical analysis. A no-flow condition is adequate at the far-field boundary, but the truncated boundary does not accurately reflect a zero-boundary condition at infinity. The poroelastic problem is known to converge, but since it is an open question if the hydrate thermal-hydrological problem converges, a grid convergence experiment was conducted in addition to using the base mesh.

In Case 1, no gas hydrate is present, allowing a purely flow and sediment-deformation calculation that can be compared to the analytical solution. The simulation domain is similar to BP3, but is now 5000 m in radius, as geomechanics requires larger domains to get an effective far-field boundary condition. The reference mesh starts with $r_{well} = 0.15\text{ m}$, then 999 elements of $\Delta r = 0.02\text{ m}$, then 500 elements logarithmically distributed from $r = 20\text{ m}$ to $r = 5000\text{ m}$.

The same parameters were used for Cases 1 and 2 (Table 9). The bulk modulus and viscosity of water are experimentally determined empirical fits. For most hydrate reservoir simulators, these are implicitly defined, but for the analytical solution they must be input. The values are included in the table for completeness, as changes to these values greatly affect the magnitude of the analytical solution.

The thermal conductivity model is from Moridis et al. (2005):

$$k^T = k_{dry}^T + (\sqrt{s_w} + \sqrt{s_h}) (k_{wet}^T - k_{dry}^T) \quad (17)$$

where s_l is the aqueous saturation and s_h is the hydrate saturation. The OPM model (Moridis et al., 2005) is used for the gas and aqueous relative permeability:

$$k_g^r = (s_g^e)^n; \quad s_g^e = \frac{(s_g - s_{gr})}{(1 - s_{wr})} \quad (18)$$

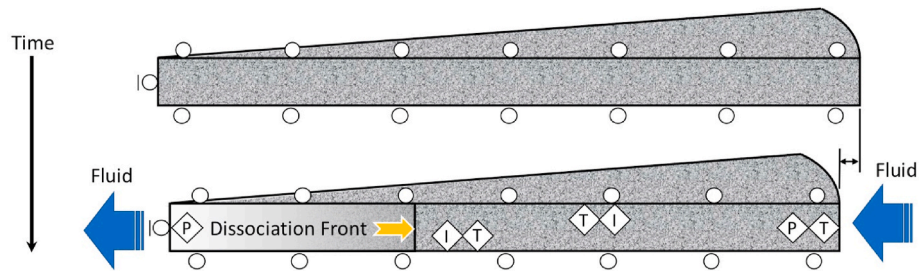


Fig. 32. Conceptual schematic of BP4, with circles indicating a roller boundary, T indicating a temperature boundary, P indicating a pressure boundary, and I indicating an impermeable boundary. Fluid flow (blue arrows) is toward the production well. (For interpretation of the references to colour in this figure legend, the reader is referred to the Web version of this article.)

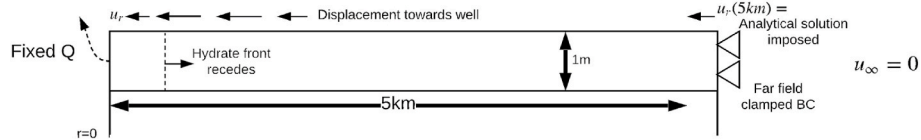


Fig. 33. Problem domain for Benchmark Problem 4.

Table 9
Parameters for both cases of BP4.

Property	Value
Intrinsic Permeability	$k = 3.0 \times 10^{-13} \text{ m}^2$
Porosity	$\phi = 0.3$
Grain Density	$\rho_s = 2600 \text{ kg/m}^3$
Specific Heat	$c_p = 1000 \text{ J/kg K}$
Dry Thermal Conductivity	$k_{dry}^T = 1.0 \text{ W/m K}$
Wet Thermal Conductivity	$k_{wet}^T = 3.1 \text{ W/m K}$
Initial Pressure	$P_{init} = 9.5 \text{ MPa}$
Initial Temperature	$T_{init} = 12^\circ \text{ C}$
Drained Bulk Modulus	$K_d = 22 \text{ GPa}$
Shear Modulus	$G = 22 \text{ GPa}$
Grain Bulk Modulus	$K_s = 100 K_d$
Water Bulk Modulus @ 12 °C	$K_w = 2.16346 \text{ GPa}$
Water Viscosity @ 12 °C	$\mu_w = 0.001227 \text{ Pa s}$

$$k_w^r = (s_w^e)^n; s_w^e = \frac{(s_w - s_{wr})}{(1 - s_{wr})} \quad (19)$$

where k_g^r is the gas relative permeability, s_g^e is the effective gas saturation, s_g is the actual gas saturation, $n = 3.0$, $s_{gr} = 0.02$ and $s_{wr} = 0.12$, are the residual gas and aqueous saturations, s_w^e is the effective aqueous saturation, and s_w is the actual aqueous saturation. For capillarity, the scaled van Genuchten equation (van Genuchten, 1980) is used:

$$P_{cap} = \min \left\{ P_{max}, -P_o \left[(s_w^e)^{-1/\lambda} - 1 \right]^{(1-\lambda)} \right\}; s_w^e = \frac{(s_w - s_{wr})}{(1 - s_{wr})} \quad (20)$$

where $\lambda = 0.45$, $s_{wr} = 0.11$, $P_o = 12.5 \text{ kPa}$, and $P_{max} = 5 \text{ MPa}$. The initial conditions for phase saturations are aqueous saturated for the case without gas hydrate:

$$s_g(r, 0) = 0; s_w(r, 0) = 1; s_h(r, 0) = 0 \quad (21)$$

and for the case with gas hydrate equal pore volume fractions of aqueous and hydrate are assumed:

$$s_g(r, 0) = 0; s_w(r, 0) = 0.5; s_h(r, 0) = 0.5 \quad (22)$$

At the production well, which is a finite cylinder of radius 0.15 m, a constant rate production (by mass) is assumed:

$$Q = 1 \text{ kg/s} \quad (23)$$

The analytical solution is for a Dirac delta line source at $r = 0 \text{ m}$. The radial displacement is 0 m at the center of the domain. The boundary conditions at the far edge are matched to the analytical solution to exactly match the infinite domain:

$$P(5 \text{ km}, t) = P_{analytical}(5 \text{ km}, t); u(5 \text{ km}, t) = u_{analytical}(5 \text{ km}, t) \quad (24)$$

which are provided in the next section. However, the pressure field does not change significantly at 5 km, so a constant-pressure boundary at 5 km will suffice for the flow simulation. In the plane stress case, there is deformation in the vertical direction. To match plane stress, roller boundary conditions were applied to one horizontal plane of the mechanical domain, and constant traction boundary conditions were applied on the other side. For plane strain, rollers were applied to the top and bottom. For the geomechanical elements of the problem, parameters were chosen that represent very hard rock.

7.2. Analytical solution for the BP4 case 1 – without gas hydrate

The problem is cylindrically symmetric, which provides the following constraints on the displacement in the angular direction:

$$u_\theta = 0; u_{,\theta} = 0 \quad (25)$$

Note that the $\theta\theta$ strain is not 0, as under axisymmetry the radial displacement adds a hoop strain:

$$\epsilon_{axi} = \begin{bmatrix} u_{r,r} & \frac{1}{2}(u_{r,z} + u_{z,r}) & 0 \\ \frac{1}{2}(u_{r,z} + u_{z,r}) & u_{z,z} & 0 \\ 0 & 0 & \frac{u_r}{r} \end{bmatrix} \quad (26)$$

In the vertical direction, the problem definition specifies a plain strain condition, corresponding to a slice through a long vertical well. This problem was first solved by Rudnicki (1986). The rate of injection is denoted Q_s/h , which describes the volumetric injection rate Q_s per unit length h in the z direction. The solution of the solid displacement in the radial direction, u_r is given by

$$u_r = \frac{(Q_s/h) \alpha f(\xi) r}{8\pi(k/\mu)(K_d + 4G/3)} \quad (27)$$

where

$$f(\xi) = \frac{1 - e^{-\xi}}{\xi} + E_1(\xi); \xi = \frac{r^2}{4Dt} \quad (28)$$

$$D = \frac{k}{\mu} M \left(1 - \frac{\alpha^2 M}{K_u + 4G/3} \right) = \frac{k}{\mu} M \left(\frac{K_d + 4G/3}{K_u + 4G/3} \right) \quad (29)$$

where K_u is the undrained bulk modulus, and $E_1(\xi)$ is the exponential integral defined as

$$E_1(\xi) = \int_{\xi}^{\infty} \frac{e^{-s}}{s} ds \quad (30)$$

The Biot coefficient and fluid storativity are

$$\alpha = 1 - \frac{K_d}{K_s}; M = \frac{K_s}{\alpha - \phi(1 - K_s/K_w)} \quad (31)$$

The solution for pressure is

$$P = \frac{Q_s/h}{4\pi k/\eta} E_1(\xi) + P(0) \quad (32)$$

where $P(0)$ is the initial background pressure. This analytical solution is used in Case 1 as a benchmark to verify the basic hydrological-mechanical response of the simulators.

7.3. Results for the BP4 case 1 – without gas hydrate

Case 1 is initialized as an aqueous saturated system at constant temperature, Eqn. (21). The outer radial boundary conditions for pressure, temperature, and radial displacement are:

$$p(5000 \text{ m}, t) = \text{Eqn. (32)}; T(5000 \text{ m}, t) = 12 \text{ }^\circ\text{C}; u_r(5000 \text{ m}, t) = \text{Eqn. (27)} \quad (33)$$

The total simulation duration is 6 h. Each code provided the following results:

1. P, T, u_r as functions of r at 1, 3, and 6 h.
2. Production of water at the well versus time.

Results from seven numerical simulations, plus the analytical solution for pressure versus radial distance, are plotted in semi-log form ($\log_{10} r$) in Fig. 34. The simulations show good agreement with each other and with the analytical solution, the analytical results for pressure falling within the distribution of curves for each of the reported times (Fig. 34). This problem was in general solved using an r, z coordinate system, however, some solutions were restricted by the geomechanical system to a rectilinear coordinate system, yielding a three dimensional domain, which made application of the outer radial boundary conditions from the analytical solutions difficult. Some of the differences in pressure plots, apparent in Fig. 34, are due to differences in grid discretizations.

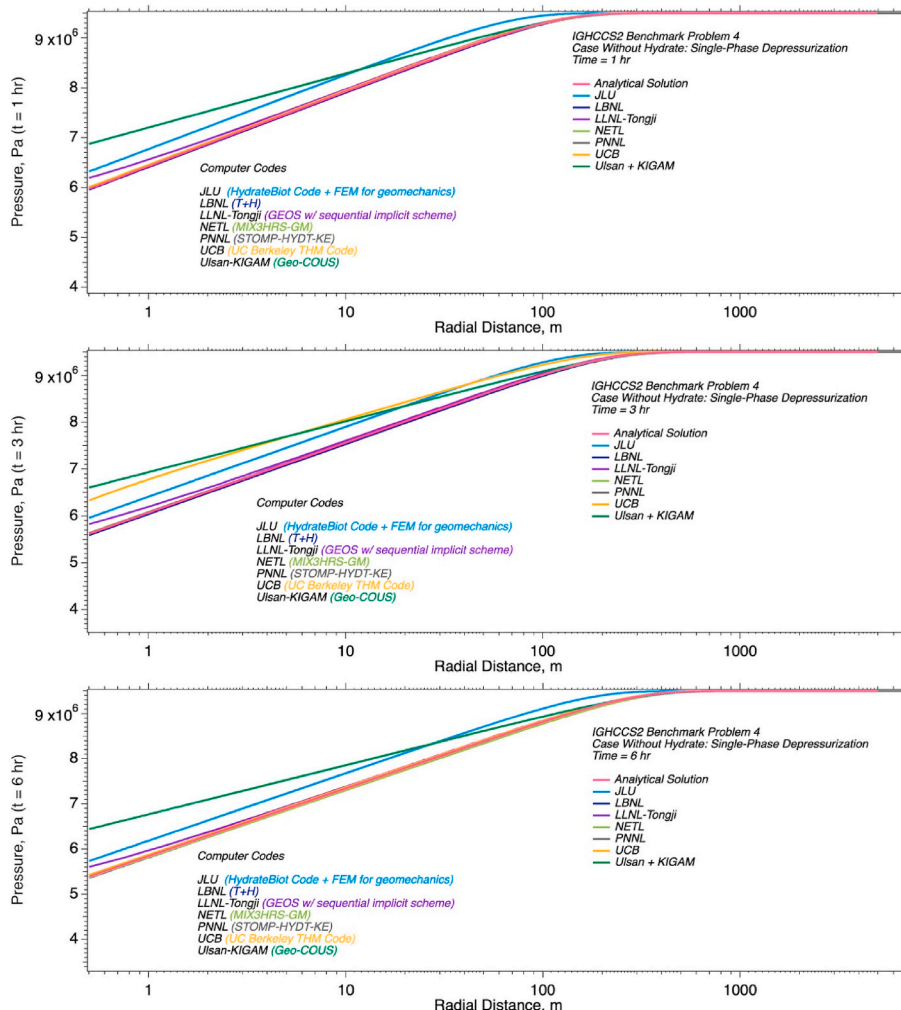


Fig. 34. Numerical simulations and analytical solution for BP4 Case 1 (without gas hydrate) showing pressure versus radial distance at 1, 3, and 6 h.

The 5000 m radial extent of the domain is not sufficiently far from the production well to avoid changes in pressure and radial displacement. The problem description recommends applying a boundary condition based on the analytical solution, i.e. the time-varying, analytical values of pressure and radial displacement at 5000 m. The pressure at $r = 5000$ m varies only slightly from the initial pressure of 9.5 MPa. Variation in the radial displacement as given by the analytical solution is nonlinear versus time near the production well, but at a 5000 m, it can be represented as a straight line, as shown in Fig. 35.

Fig. 36 shows radial displacements from the seven simulations and the analytical solution versus radial distance at 1, 3, and 6 h. There is general agreement across the simulations and with the analytical solution, all showing an inflection point in the radial displacement versus distance, an increase in largest radial displacement over time, and a migration of the inflection point radially outward over time. Interestingly, the agreement in radial displacements versus radial distance improved with simulation time. Some simulations did not impose the analytical solution for radial displacement at the outer radial boundary, but the differences in radial displacement generated by this choice were limited to later times and distances greater than 2000 m.

7.4. Results for B4 case 2 – with gas hydrate

The hydrological and geomechanical parameters for Case 2 are the same as Case 1, but Case 2 is initiated with gas hydrate, Eqn. (22), altering the effective permeability and thermal conductivity of the material. As no analytical solution exists for this problem the outer radial boundary conditions for pressure, temperature, and radial displacement are held fixed

$$p(5000 \text{ m}, t) = 9.5 \text{ MPa}; T(5000 \text{ m}, t) = 12^\circ \text{C}; u_r(5000 \text{ m}, t) = 0 \text{ m} \quad (34)$$

For production, we impose a constant pressure of $P = 3.1$ MPa at $r = 0$. Dependence of the elastic moduli on the hydrate saturation is neglected.

The simulation duration was 30 days. Each participant provided output for:

1. P , T , u_r , s_h as functions of r at 1, 2, 5, 10, 20, and 30 days.
2. Mass rate of hydrate dissociate vs time.
3. Production of water and gas at the well versus time.

Gas hydrate saturation versus radial distance is shown at 1, 10, and 30 days in Fig. 37. The PNNL simulation consistently shows delayed dissociation of gas hydrate with its kinetic dissociation.

Pressure profiles at 1, 10, and 30 days are shown in Fig. 38, and generally agree with the hydrate saturation profiles of Fig. 37. Sharp increases in pressure versus radial distances occur at 10 days for the JLU simulation and 30 days for the LBNL simulation, reflecting the gas hydrate lensing. The sharp pressure increases align with the points of higher hydrate saturation in those simulations with lensing, corresponding to a reduction in effective permeability at that point.

Temperature profiles at 1, 10, and 30 days are shown in Fig. 39. Temperatures for all simulations are reduced on the production side of the gas hydrate dissociation front, and a sharp increase in temperature occurs in correspondence with the sharp pressure increase for simulations with lensing gas hydrate saturations.

The bulk modulus was considered to be independent of gas hydrate saturation, so radial displacement was most impacted by pressure, as shown in Fig. 40. There is more variation in radial displacement for Case 1 than for Case 2 with gas hydrate. Gas hydrate dissociation yields liquid water and gaseous methane, producing three-phase conditions: 1) aqueous, 2) gas, and 3) hydrate. Production pressures were maintained above the Q1 point (quadruple point of water), avoiding ice. Effective stress is computed from the deviatoric stress and fluid pressure, where the fluid pressure may be considered to be a function of the aqueous and gas saturations. Different computer codes use different approaches for modeling the effective stress, which contributes to the greater range in radial displacements. For example, the PNNL simulations uses the non-wetting fluid pressure, not a saturation weighted fluid pressure in the effective stress calculation. The difference between the JLU and the other simulations is consistent between cases.

Figs. 41 and 42 respectively show methane (i.e., gas) and water production rates at the well versus time. Both production rates show variability across the simulations. Production rates are dependent on several coupled processes, including hydrate dissociation rates, phase saturations, pressure gradients, and effective permeabilities. Drops in production are noted for the JLU and LBNL simulations due to gas hydrate lensing and sharp decreases in effective permeability. Simulations without gas hydrate lensing generally show gradual decays in production rates with time.

7.5. BP4 summary

This problem considered the production from a hypothetical cylindrically symmetric reservoir from a central production well, with and without gas hydrates, under geomechanical conditions of fixed vertical strain. Radial displacements are set to be zero at the center of the domain and at infinite radial distance, but otherwise the domain is free to deform radially. The first case, without gas hydrates, produced only water, with radial deformation occurring in response to changes in effective stress due to changes in pressure due to removal of fluid via the central well. This scenario has an analytical solution against which to compare the numerical simulations, and which was additionally used to assign boundary conditions for pressure and radial displacement at a finite radial distance.

The second case involved production in the presence of hydrates, starting with a uniform distribution of gas hydrate. Fluid production at the central well drew down pressures within the domain, reducing pore pressures near the well to below the gas hydrate stability pressure, resulting in hydrate dissociation. Hydrate dissociation produced mobile water and methane, creating a gas phase comprised of methane and water vapor and an aqueous phase comprising liquid water and

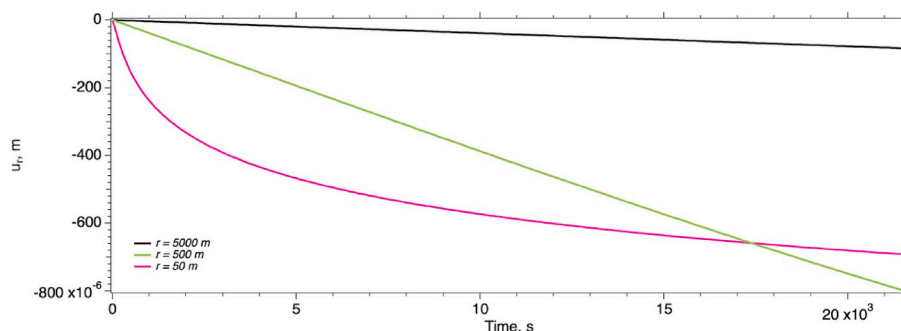


Fig. 35. Analytical solution for BP4 Case 1 (without gas hydrate) showing radial displacement versus time at 50, 500, and 5000 m.

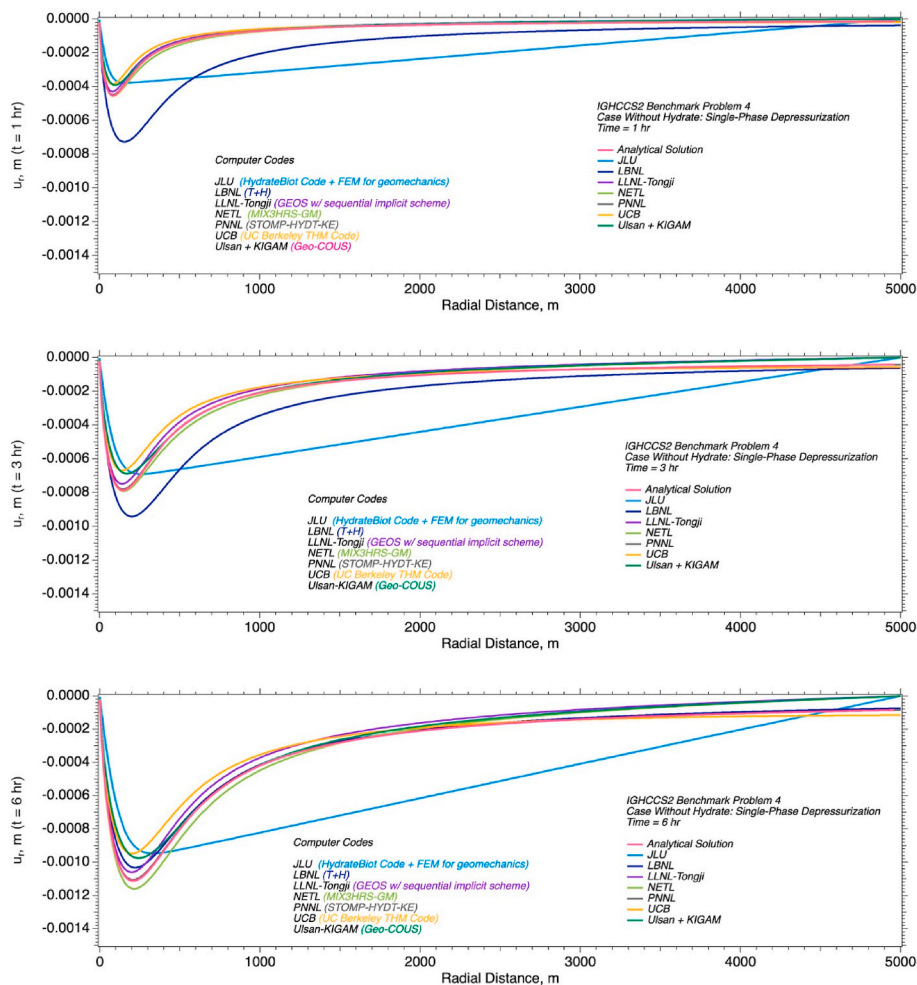


Fig. 36. Numerical simulations and analytical solution for BP4 Case 1 (without gas hydrate) showing radial displacement versus radial distance at 1, 3, and 6 h.

dissolved methane. The suite of numerical simulators was applied to both cases. The suite of simulators was distinguished by geomechanical coordinate systems and gas hydrate dissociation models.

For geomechanics, most, but not all, simulators had radial (axisymmetric) modeling capabilities. For those simulators, a simple one-dimensional computational domain could be used to solve the problem, but for those simulators without, a two-dimensional domain was required. Some simulators had radial capabilities for flow and transport, but non-radial capabilities for geomechanics, and the required coupling necessitated a two-dimensional domain to solve the problem.

For gas hydrate dissociation models, some simulators used equilibrium formulations, where the mobile fluids, the aqueous and gas phases, are assumed to be in thermodynamic equilibrium with the immobile phases, such as ice, hydrate and sediment. Conversely, some simulators had kinetic formulations; where disequilibrium was allowed between mobile and immobile phases.

The distinction between equilibrium and kinetic formulations is important. For example, depressurization problems generally yield sharp gas hydrate dissociation fronts, characterized by a temperature drop due to the endothermic cooling from gas hydrate dissociation. For simulators with equilibrium or fast kinetic formulations, gas hydrate lensing can occur near this dissociation front, with the localized increases in hydrate saturation resulting in effective permeability changes and changes in fluid flow through the dissociation front. Results from the JLU team at 10 days and LBNL team at 30 days show these characteristic regions of high/low hydrate saturations (Fig. 37). To illustrate where lensing can occur, Fig. 43 shows a plot of pressure, hydrate

saturation, and methane hydrate equilibrium pressure (a function of temperature) vs. radial distance for the LBNL team at 30 days. The hydrate equilibrium pressure is lowest in regions that have already experienced endothermic hydrate dissociation ($r < 6.5$ m) and are thus colder than the initial reservoir temperature.

In Fig. 43, we see localized depression of the hydrate equilibrium pressure curve due to the lower temperatures in the regions exhibiting lensing behavior. Where the equilibrium curve touches or drops below the modeled pressure curve, hydrate formation may occur, even downstream of the main dissociation front where gas hydrate is expected to have fully dissociated. Secondary hydrate formation and preservation of hydrate in regions between the well and the outer dissociation front due to the locally low temperatures create local decreases in effective permeability that, in extreme cases as in Fig. 37, may stop production. Hydrate formation may continue due to the flow of water and gas through these cooled regions. We would expect each lens to act like an additional dissociation front, with dissociation at the side facing the well, and with possible hydrate formation on the outer face. Narrow regions of decreased effective permeability can lead to Joule-Thompson cooling (for simulators that include such effects), creating a feedback loop in which the additional temperature reduction enhances local hydrate formation.

The kinetic delay in gas hydrate formation in some simulators prevents this secondary hydrate formation feedback loop, meaning no gas hydrate lensing occurs. In simulators with fast kinetics or equilibrium assumptions, however, secondary gas hydrate forms nearly instantaneously, resulting in lensing. The mesh size has also been shown to affect

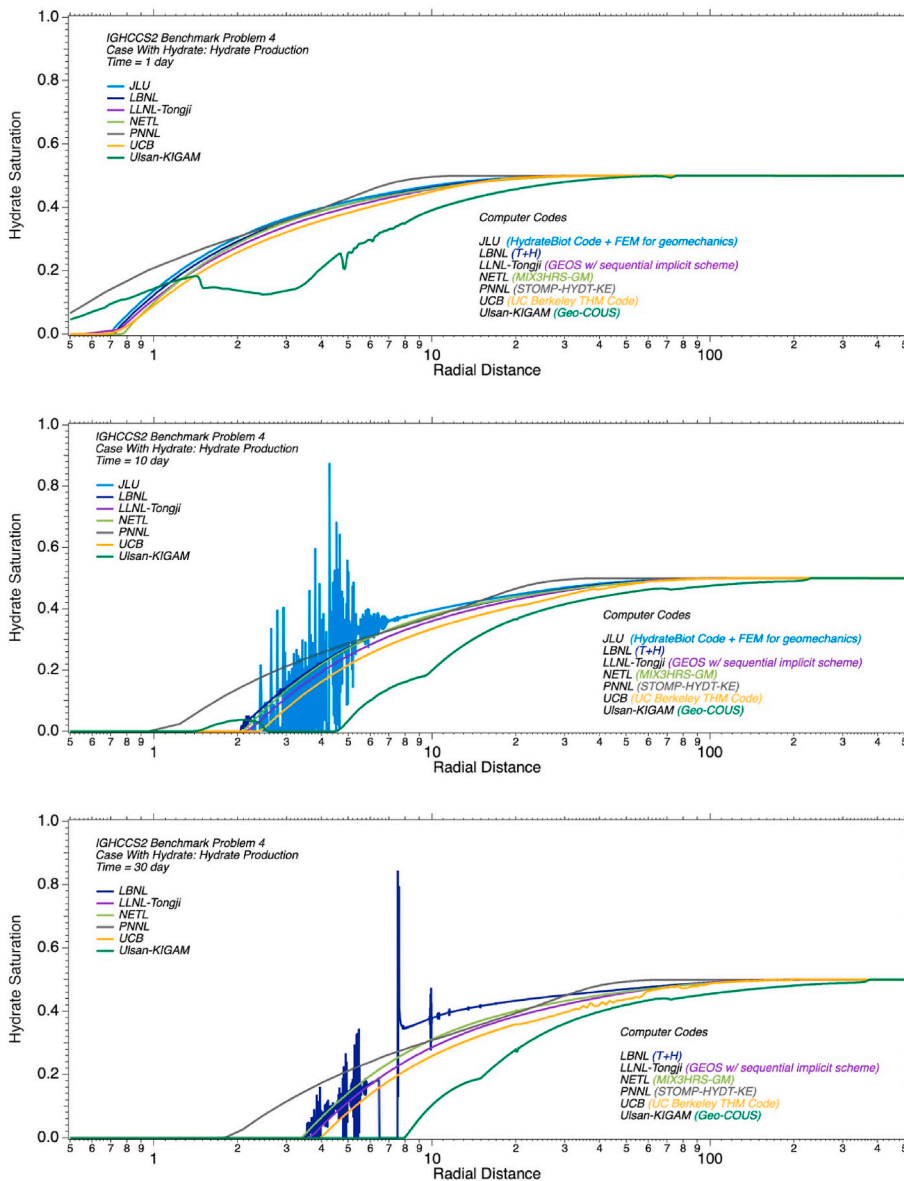


Fig. 37. Numerical simulations for BP4 Case 2 (with gas hydrate) showing gas hydrate saturation versus radial distance at 1, 10, and 30 days formulation. The Ulsan-KIGAM team shows deeper gas hydrate dissociation further into the reservoir compared with the other teams across all times. At $t = 10$ days, the JLU solution deviates from the other solutions as hydrate “lensing” occurs, in which regions of alternating high and low hydrate saturation form in response to strong depressurization combined with the endothermic cooling of the near-well hydrate zone due to dissociation. Localized regions of high hydrate saturation reduce local permeability and create locally steep pressure gradients, and thus the variations in saturation are magnified by localized Joule-Thomson cooling. This results in the JLU simulation terminating at 10.73 days. By $t = 30$ days, the LBNL simulation is additionally showing lensing behavior, resulting in a localized region depleted of hydrate (near $r = 6.0\text{--}7.5\text{ m}$) with higher gas hydrate saturation adjacent to it. The codes that display lensing behavior still produce gas hydrate saturation profiles that, on average, remain near or within the cluster of curves.

lensing behavior, with coarser meshes not resolving small-scale features like localized hydrate formation. Future studies are planned to study this behavior.

In general, the different computer codes showed good agreement in terms of pressure and radial displacements against the analytical solution for the scenario without gas hydrate. No significant differences were noted in results between codes with radial capabilities and those without, although the simulation times would have taken longer on the two-dimensional domains. The addition of gas hydrate to the problem resulted in two complexities that reduced agreement across the solutions. For two simulators, the dynamic nature of hydrate dissociation, and secondary hydrate formation, produced hydrate lenses, that altered the nature of water and methane production. Effective permeability is a function of hydrate saturation and the spread in water and methane production rates is a good indication of differences in effective permeability for problems where the pressure boundaries are well defined. The dependence of gas hydrate saturation on effective permeability has been implemented in numerical simulators, both via the intrinsic permeability parameter and the fluid relative permeability parameter. Careful attention is needed in the application of numerical simulators ensure the proper effective permeability model is applied, and not being accidentally

applied twice, as was noted and corrected for one simulation.

8. Benchmark problem 5 – Nankai Trough

BP5 Champion: Sayuri Kimoto, Kyoto University.

When producing methane from hydrates in marine sediments through schemes such as heating, depressurization, and inhibitor injection, it is necessary to consider the potential for seafloor and sub-surface deformations. BP5 considers the coupled chemo-thermo-mechanical response of a suboceanic methane hydrate deposit to depressurization via pumping from a single well in a setting modeled on the Nankai Trough. Methane hydrates occur in the Nankai Trough around Japan in deposits at water depths of about 1000 m (Kimoto et al., 2007).

The world’s first offshore production test of methane hydrates was conducted in March 2013 using the depressurization method off the Atsumi and Shima Peninsulas in Japan (Yamamoto et al., 2014, 2017). BP5 is largely based on this offshore test, and utilizes the specified geology, initial conditions, boundary conditions, and petrophysical parameters from the study of Akaki et al. (2016). Results from BP5 can be compared with a more thorough published analysis (Akaki et al., 2016;

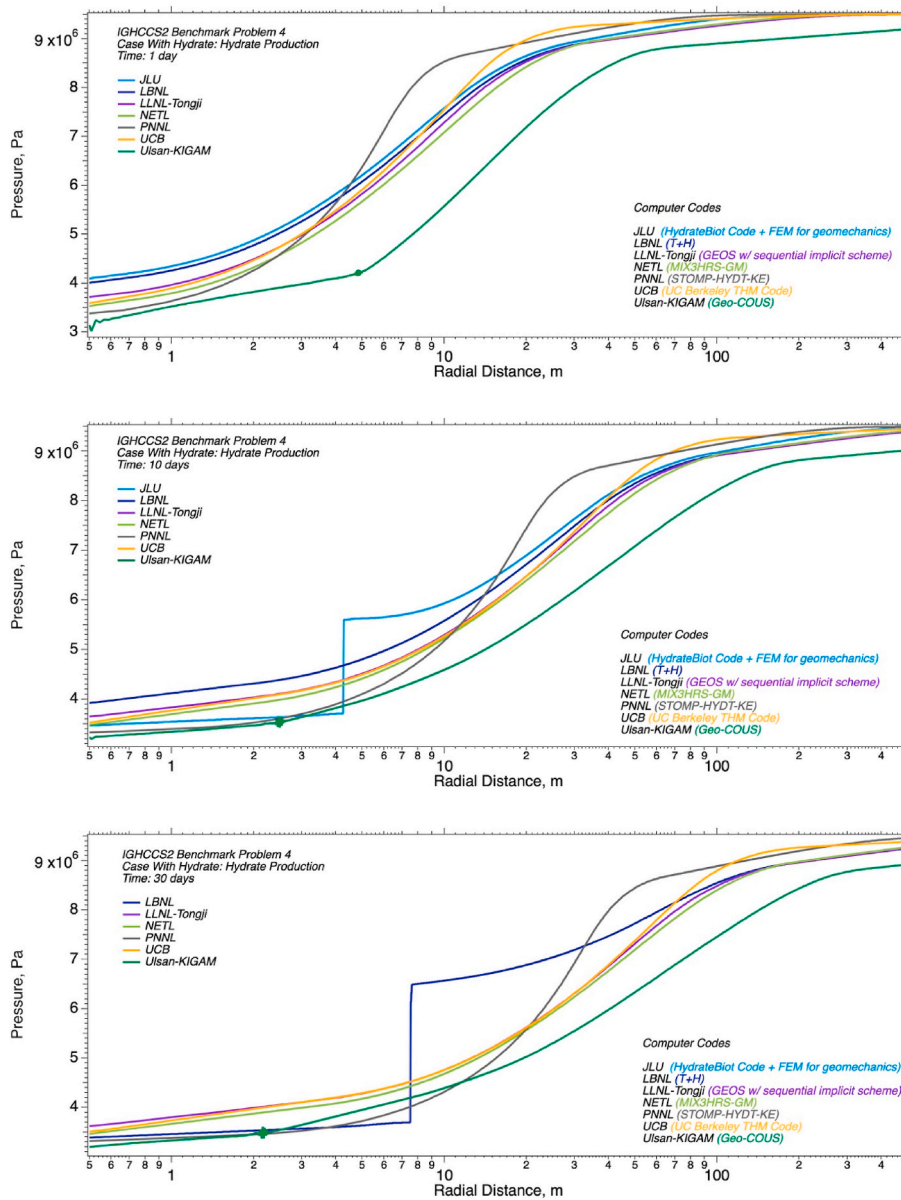


Fig. 38. Numerical simulations for BP4 Case 2 (with gas hydrate) showing pressure versus radial distance at 1, 10, and 30 days.

Kimoto et al., 2010), in which the authors conclude that seafloor and subsurface deformations during hydrate dissociation were induced by the generation and subsequent dissipation of water and gas, coupled with weakening of sediment mechanical strength as hydrate dissociated.

Modeling dissociation of methane hydrate in this problem requires an accurate representation of solid/liquid/gas phase transitions under partial saturation conditions. These transitions are strongly coupled through heat transfer and thermodynamics due to the endothermic nature of gas hydrate dissociation. The models must not only honor the temperature and pressure phase equilibria for methane hydrate stability, but must also account for the reduction in hydrate saturation which yields reductions in the mechanical strength of the suboceanic sediments. Solution of BP5 requires a numerical simulator with coupled chemo-thermo-mechanical process capabilities in which the chemo element principally involves hydrate dissociation/formation. A schematic of BP5 is shown in Fig. 44.

8.1. BP5 description

A two-dimensional axisymmetric computational domain is specified

with an outer radius of 1000 m and overall thickness of 500 m, with the upper boundary being the sea floor, at a water depth of 1000 m. The domain is divided into six horizontal layers, representing six sediment layers, with only the fifth layer from the top bearing methane hydrate. In the progression from sea floor to the bottom of the domain (Fig. 45), the uppermost two layers are characterized as over-consolidated mud, the third layer is a turbidite with alternating sand and mud intervals, and the fourth layer is the clay seal overlying the gas hydrate-bearing reservoir in layer 5; the sixth layer is clay, and the model domain is assumed to overlie a stiff soil.

The hydrate-bearing layer of this benchmark problem is an idealization of the actual concentrated hydrate zone of the field test, which comprised three distinct sublayers: 1) an upper zone with numerous thin turbidite sequences of sand-silt alternations (i.e., tens of centimeters in thickness) and high hydrate saturation (i.e. $s_h = 0.8$); 2) thicker alternations of silt and sand with lower hydrate saturations and greater dominance of silt; and 3) thicker (i.e., 1 m or more) channel turbidites (Yamamoto et al., 2017).

The system is initialized with hydrostatic pressure conditions, no free gas, a linear geothermal gradient, and linear vertical and horizontal

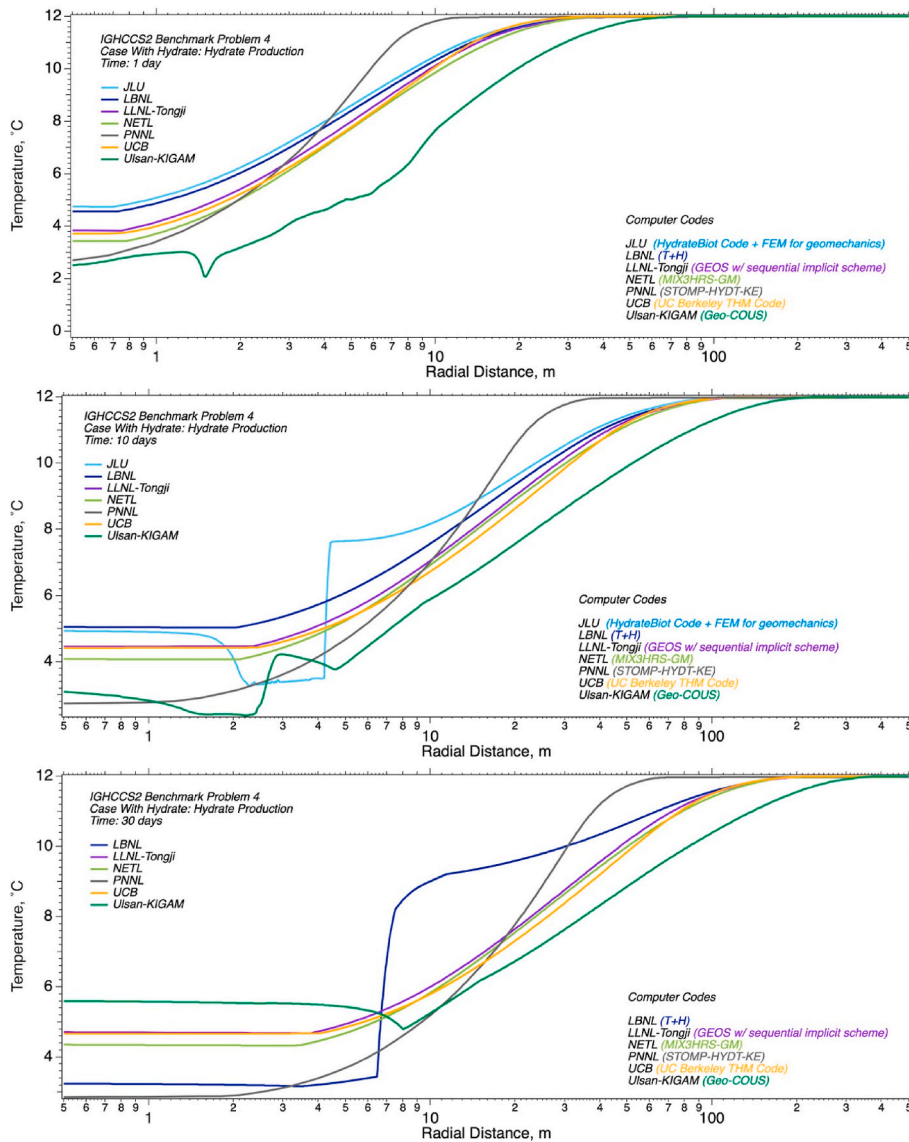


Fig. 39. Numerical simulations for BP4 Case 2 (with gas hydrate) showing temperature versus radial distance at 1, 10, and 30 days.

stress gradients. Boundary conditions on the upper, lower, and outer radial surfaces are maintained at the initial conditions, as shown in Fig. 46. The inner radial boundary surface is considered to be an axis of symmetry (i.e., an undrained, adiabatic boundary), except for a 20 m interval at the top of the hydrate-bearing layer. Along this boundary surface, a uniform pressure is applied that decreases to 4 MPa at a rate of 0.15 kPa/s from an initial pressure of 12 MPa (Fig. 47). This pressure reduction crosses the hydrate stability curve, yielding hydrate dissociation. Enthalpy associated with fluid flow across the inner radial boundary is considered, but otherwise the inner radial boundary is considered to be adiabatic. Specification details for the problem are provided below by categories: domain discretization, initial conditions, boundary conditions, geomechanical properties, hydraulic properties, and thermal properties.

8.1.1. Discretization

Discretization in the radial direction is variable, with the first 2 m being divided into 20 equally spaced, 0.1 m divisions. From 2 to 1000 m, 80 radial divisions were used with a logarithmic distribution of divisions, starting with 0.1 m. The nominal vertical division spacing is 5 m, with a minimum of three subdivisions within each sediment layer. A vertical division spacing of 0.5 m was used within the hydrate-bearing

sediment. Thicknesses of the six sediment layers are shown in Fig. 45, with an indication of the spatially-dependent model discretization.

8.1.2. Initial conditions

Hydrostatic conditions are specified for the pressure distribution, with a pressure of 14.6 MPa at the bottom of the domain and 9.8 MPa at the top (i.e., fresh water hydrostatic conditions). The initial salinity is 0.0, consistent with fresh water. A conventional geothermal gradient of 30 K/km (0.03 K/m) is specified, yielding a temperature of 292 K (18.85 °C) at the bottom of the domain, and 277 K (3.85 °C) at the top. A hydrate saturation of 0.4 is specified for sediment layer L5, otherwise the hydrate saturation is 0.0. Initial gas saturation is specified as 0.0 throughout the domain, yielding aqueous saturations of 0.6 within sediment layer L5, and 1.0 elsewhere. The vertical and horizontal stress gradients are computed assuming a uniform bulk density for the sediments of 1828.75 kg/m³, yielding a stress gradient of 17.94 kPa/m. With a hydraulic gradient of 9.6 kPa/m, the effective stress gradient is 8.34 kPa/m. Horizontal stress is specified as a fraction of the vertical stress. Vertical σ_v , horizontal σ_h , effective vertical σ'_v , and effective horizontal σ'_h stress are computed as linear functions of depth z from the seabed floor:

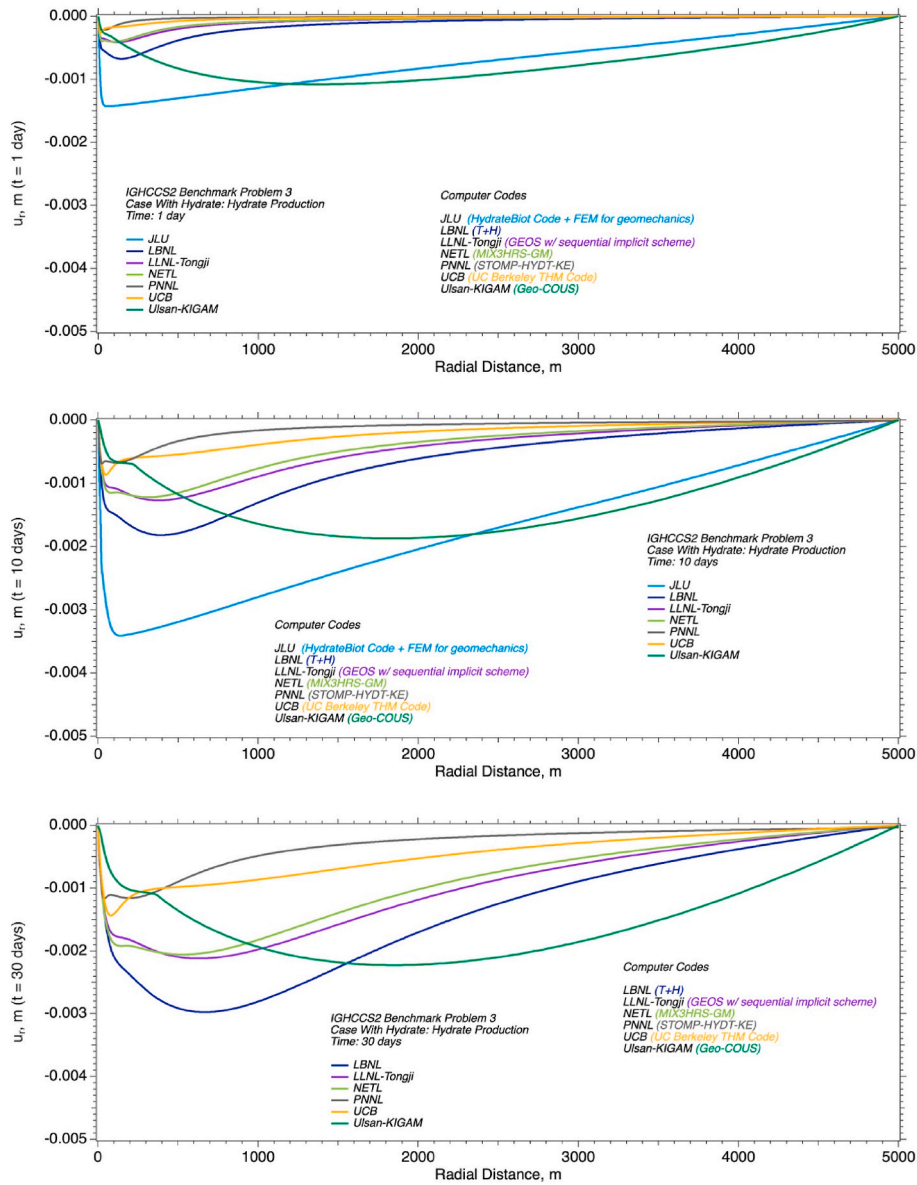


Fig. 40. Numerical simulations for BP4 Case 2 (with gas hydrate) showing radial displacement versus radial distance at 1, 10, and 30 days.

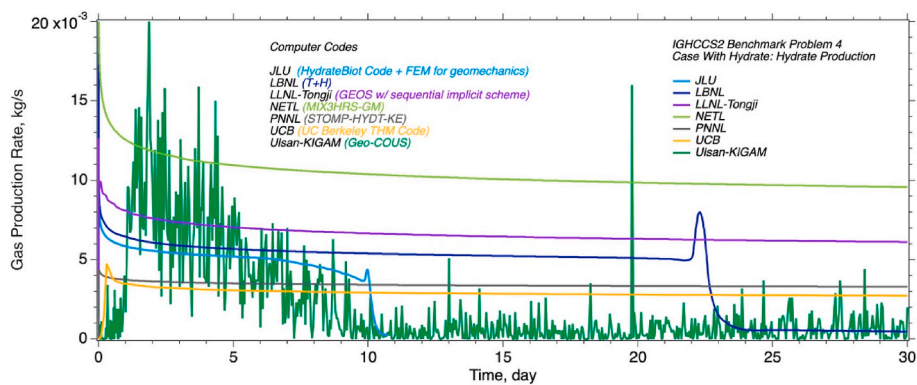


Fig. 41. Numerical simulations for BP4 Case 2 (with gas hydrate) showing gas production at the well versus time.

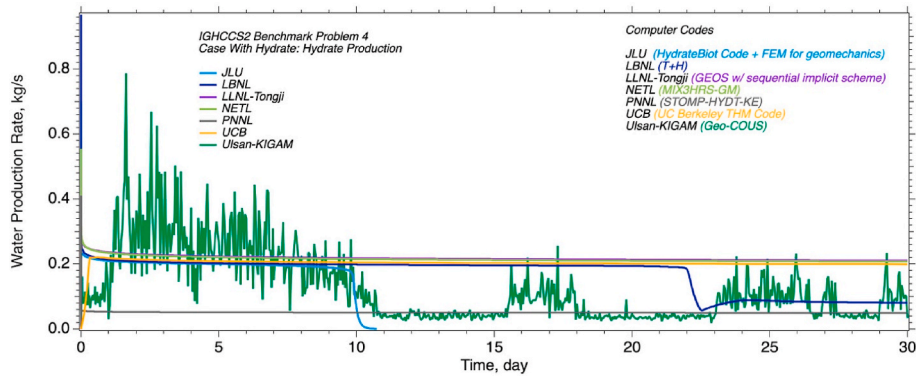


Fig. 42. Numerical simulations for BP4 Case 2 (with gas hydrate) showing water production at the well versus time.

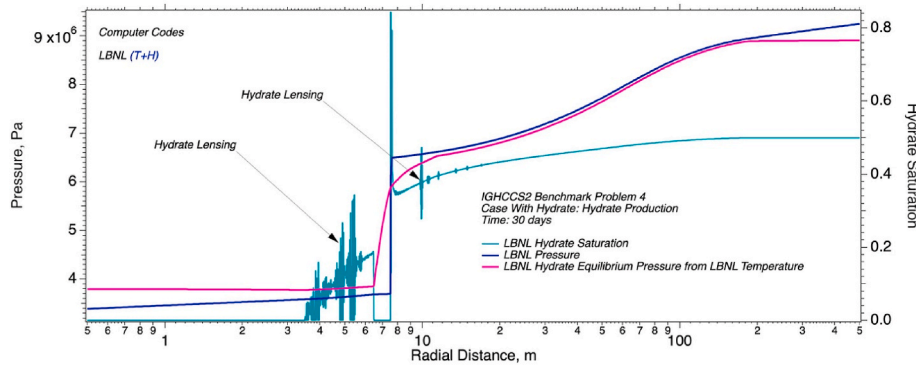


Fig. 43. Numerical simulations for BP4 Case 2 (with gas hydrate) showing pressure, hydrate saturation, and methane hydrate equilibrium pressure from the temperature profile for the LBNL simulation at 30 days.

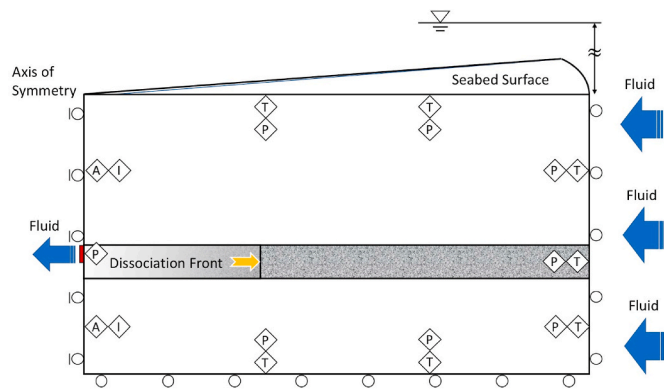


Fig. 44. Conceptual schematic of BP5, with circles indicating a roller boundary, T indicating a temperature boundary, P indicating a pressure boundary, I indicating an impermeable boundary, and A indicating an adiabatic boundary. Fluid flow (blue arrows) is toward the production well, which removes water only over the interval indicated by the red block contacting the upper portion of the hydrate-bearing reservoir (grey layer). Above and below the reservoir layer, the sediment is assumed to be primarily hydrate-free clay with limited permeability. Sea level is indicated by the vertical white arrow at the top of the figure. (For interpretation of the references to colour in this figure legend, the reader is referred to the Web version of this article.)

$$\sigma_v = \gamma z; \sigma_h = K_o \sigma_v; \dot{\sigma}_v = \dot{\gamma} z; \dot{\sigma}_h = K_o \dot{\sigma}_v \quad (35)$$

$$\gamma = 17.94 \frac{kPa}{m}; \dot{\gamma} = 8.34 \frac{kPa}{m}; K_o = 0.5 \quad (36)$$

A synopsis of the initial conditions is shown graphically in Fig. 46.

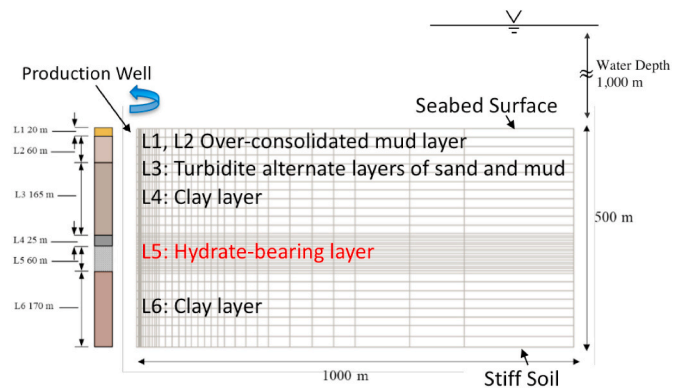


Fig. 45. BP5 computational domain showing the six layers (L1-L6), recognizing that only L5 contains gas hydrate. This idealized 60 m-thick layer extends from 270 to 330 mbsf and is assumed to have a gas hydrate saturation of $s_h = 0.4$.

8.1.3. Boundary conditions

Boundary conditions are imposed on the upper, lower, outer radial, and inner radial boundary surfaces. The upper surface is defined at the sea floor, and the lower surface is defined at the bottom of the computational domain, 500 m below the sea floor. At the upper and lower boundaries, pressure and temperature conditions are maintained at the initial conditions. The upper boundary is maintained at the initial stress state, and the lower boundary is considered to be a plane strain boundary (i.e., zero displacement). At the outer radial boundary, temperature, pressure, and stress conditions are maintained at the initial conditions. Two boundary conditions are applied over the inner radial boundary surface:

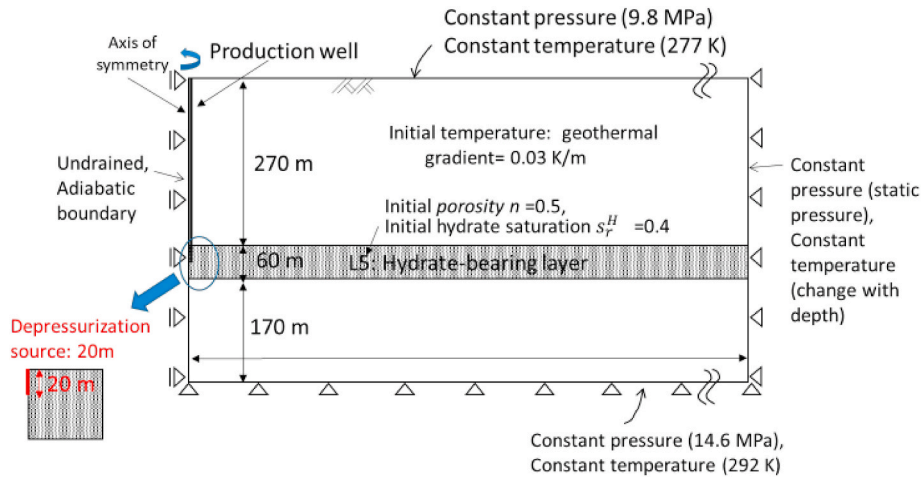


Fig. 46. Initial conditions for BP5.

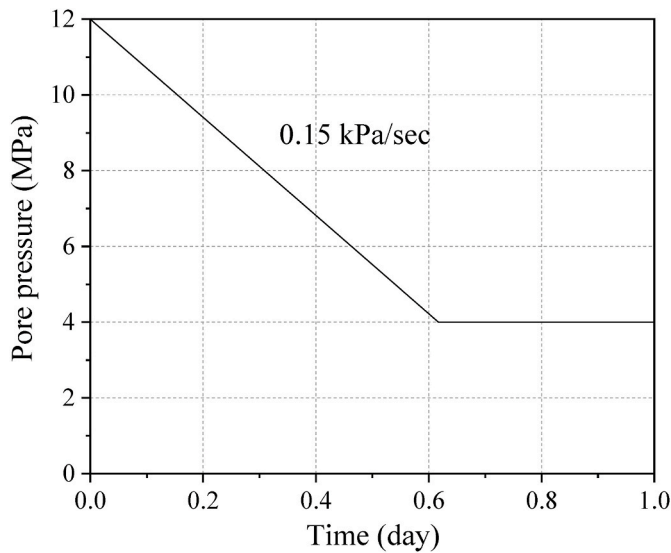


Fig. 47. Pressure versus time boundary conditions for BP5 applied at the well within the upper 20 m of the hydrate-bearing layer (red depressurization interval in Fig. 46 inset).

- 1) outside of the vertical extent of the hydrate-bearing layer, the inner radial boundary is specified as being adiabatic for energy transport, impervious for flow, and zero displacement for geomechanics;
- 2) within the 20 m-thick production interval within the hydrate-bearing layer (i.e., from 270 to 290 m below the seabed floor) the pressure is variable in time but constant over the vertical extent, starting at 12 MPa, decreasing to 4 MPa at a rate of -0.15 kPa/s and then remaining constant (Fig. 47). Additionally, zero displacement conditions are imposed for the hydrate bearing layer. Boundary conditions are shown graphically in Fig. 47.

8.1.4. Geomechanical properties

Geomechanical properties for were derived from studies of the dynamic behavior of methane hydrates during a potential earthquake in the Nankai Trough (Akaki et al., 2016). For BP5, the assumption of linear-elastic geomechanics is sufficient. For analyses, considering elasto-plastic or elasto-viscoplastic behavior, the reader is referred to the elastic-viscoplastic parameters reported by Akaki et al. (2016). Shear and bulk modulus are considered to be functions of the sediment layer and hydrate saturation. As sediment layer L5 is the only gas hydrate-bearing layer, its elastic moduli are the only hydrate saturation

dependent parameters, yielding values larger than the initial values. The initial elastic shear modulus is given by the linear distribution in each layer, based on the confining effective stress. The elastic property parameters are listed in Table 10. The dependence of shear and bulk modulus on hydrate saturation is defined via two parameters:

$$G = \left(1 + a^E \frac{s_h}{s_h^E}\right) G_o; K = \left(1 + a^E \frac{s_h}{s_h^E}\right) K_o \quad (37)$$

where a^E is a fitting parameter, s_h^E is the reference hydrate saturation, G is the shear modulus, G_o is the initial shear modulus, K is the bulk modulus, and K_o is the initial bulk modulus.

8.1.5. Hydraulic properties

The intrinsic permeability varies between sediment layers, but is homogeneous within a sediment layer. The effective permeability depends on the intrinsic permeability and the hydrate saturation. The gas and aqueous relative permeabilities are dependent on gas and aqueous saturation, following conventional equational forms. Akaki et al. (2016) specifies separate aqueous and gas hydraulic conductivities for each sediment layer, listed in Table 10. For BP5, these values were converted to a single intrinsic permeability for each sediment layer by considering the aqueous and pure methane density and viscosity at the mid-point depth of the layer, and using those values to convert aqueous and gas phase hydraulic permeabilities to intrinsic permeabilities. The averaged intrinsic permeabilities are listed in Table 10. Conversion between aqueous and gas phase hydraulic permeability and intrinsic permeability depends on the phase density and viscosity:

$$k = \frac{K_w^H \rho_w}{g \mu_w}; k = \frac{K_g^H \rho_g}{g \mu_g} \quad (38)$$

where; k is intrinsic permeability in m^2 , K_w^H is aqueous hydraulic conductivity in m/s , ρ_w is aqueous density in m^3/kg , g is acceleration of gravity in m/s^2 , μ_w is aqueous viscosity in $Pa \cdot s$, K_g^H is gas hydraulic conductivity in m/s , ρ_g is gas density in kg/m^3 and μ_g is gas viscosity in $Pa \cdot s$. The subscripts g and w refer to gas and aqueous phases, respectively. Effective permeability is computed as a function of the initial porosity, current porosity, and hydrate saturation:

$$k_{eff} = k \exp\left(\frac{\phi - \phi_o}{C_k}\right) (1 - s_h)^N \quad (39)$$

where k_{eff} is the effective permeability in m^2 , n is the porosity, n_o is the initial porosity, s_h is the hydrate saturation, and C_k and N are material parameters, defined in Table 10.

Table 10
Elastic and hydraulic property parameters for BP5.

Elastic Property Parameters						
Layer	L1	L2	L3	L4	L5	L6
Normalized initial shear modulus G_o / σ_m	1045	587	218	165	150	110
Initial mean effective stress σ_{mo} , kPa	56	278	904	1432	1668	2307
Initial shear modulus G_o , MPa	58	163	197	236	250	254
Initial bulk modulus K_o , MPa	125.67	353.17	426.83	511.33	541.67	550.33
Poisson's ratio	0.3	0.3	0.3	0.3	0.3	0.3
Reference hydrate saturation s_h^r					0.79	
Fitting parameter a^E					2.0	
Hydraulic Property Parameters						
Layer	L1	L2	L3	L4	L5	L6
Aqueous hydraulic conductivity, m/s	2.0×10^{-9}	7.5×10^{-10}	2.5×10^{-10}	2.0×10^{-10}	5.0×10^{-6}	2.0×10^{-10}
Gas hydraulic conductivity, m/s	2.0×10^{-8}	7.5×10^{-9}	2.5×10^{-9}	2.0×10^{-9}	5.0×10^{-5}	2.0×10^{-9}
Intrinsic Permeability, m^2	3.2×10^{-16}	1.2×10^{-16}	3.7×10^{-17}	2.8×10^{-17}	6.8×10^{-13}	3.2×10^{-17}
Initial bulk modulus K_o , MPa	125.67	353.17	426.83	511.33	541.67	550.33
Initial Porosity, ϕ_o	0.5	0.5	0.44	0.44	0.4	0.23
Porosity Parameter, C_k	0.3	0.3	0.3	0.18	0.23	0.18
Effective permeability exponent, N	4.0	4.0	4.0	4.0	4.0	4.0

8.1.6. Outputs

Temporally and spatially varying outputs were specified for the problem. Production outputs were requested for water and methane produced at the well. Water includes the initial pore water and water derived from hydrate breakdown. Methane produced at the well includes gas-phase methane and methane dissolved in the aqueous phase. The radial distributions of pressure, temperature and hydrate saturation at different elevations were requested at specified times, and the temporal evolution of vertical displacement at the well were requested at different elevations.

8.1.6.1. Production outputs.

1. Rate and cumulative release of methane via hydrate dissociation over time for the entire domain in units of m^3/day and m^3 , respectively at standard temperature and pressure (STP) conditions of $0^\circ C$ and 1 atm pressure.
2. Rate and cumulative production of methane at the well over time in units of m^3/day and m^3 , respectively, at standard temperature and pressure (STP) conditions of $0^\circ C$ and 1 atm pressure.
3. Rate and cumulative production of water at the well over time in units of m^3/day and m^3 , respectively, at standard temperature and pressure (STP) conditions of $0^\circ C$ and 1 atm pressure.

8.1.6.2. Status of the system outputs.

1. Pressure, temperature, and hydrate saturation along the r-axis at 0.3, 0.6, 1.0, 10.0, and 30.0 days in units of Pa, $^\circ K$, and %, respectively at
 - a. the top of the hydrate-bearing sediment (HBS)
 - b. the mid-point elevation of the HBS
 - c. the base of the HBS
2. Evolution of the vertical displacements at $r = 0.0$, m over time in units of m at
 - a. the ocean floor
 - b. the top of the HBS
 - c. the base of the HBS

8.2. BP5 simulation results and comparisons

Solutions were submitted against this problem by teams from Kyoto, LBNL, LLNL-Tongji, NETL, UCB, and Ulsan-KIGAM. In general, BP5 revealed greater differences in results compared with the other problems. BP5 offered the possibility of using either elastic, elasto-plastic, or elasto-viscoplastic modeling approaches. LBNL, and LLNL-Tongji used an elastic approach and the teams from Kyoto, NETL, UCB, and Ulsan-KIGAM used an elasto-viscoplastic approach.

8.2.1. Production

BP5 is initialized with methane hydrate occurrence within a single 60-m thick hydrate bearing layer. Production occurs by lowering the pressure within the upper 20-m of the hydrate-bearing layer over time from 12 to 4 MPa (Fig. 47). This pressure drop ends below the methane hydrate stability point for the formation temperature, yielding hydrate dissociation and production of liquid and gas at the well. The liquid is principally water with dissolved methane and the gas is principally methane with water vapor. A plot of the cumulative methane released via dissociation and produced at the well in different simulations is shown in Fig. 48. Methane produced at the well includes dissolved methane that was in equilibrium with the hydrate phase prior to dissociation.

Whereas there was broad agreement in methane dissociation and well production, there was considerable disagreement in the amount of water produced at the well, as shown in the plot of cumulative water production versus time (Fig. 49). Water production is controlled by the rate of hydrate dissociation, the well pressure, the outer radial pressure, and the resistance for aqueous flow through the hydrate-bearing layer, as well as through the over- and under-burden layers. The well pressure and outer radial boundary pressures were fixed, which suggests differences in water production arose from hydrate dissociation or water flow from the outer radial boundary to the well through the hydrate-bearing layer and the over- and under-burden layers. Absolute and aqueous relative permeability functions are specified in the problem description, but the absolute permeability depends on porosity, which changes in response to deformation of the layers. The relative permeability model is a novel formulation, and some teams opted to approximate the function with an existing code capability.

8.2.2. Status of the system

The distribution of hydrate saturation versus radial distance at the bottom, middle, and top of the hydrate-bearing layer at 30 days is shown

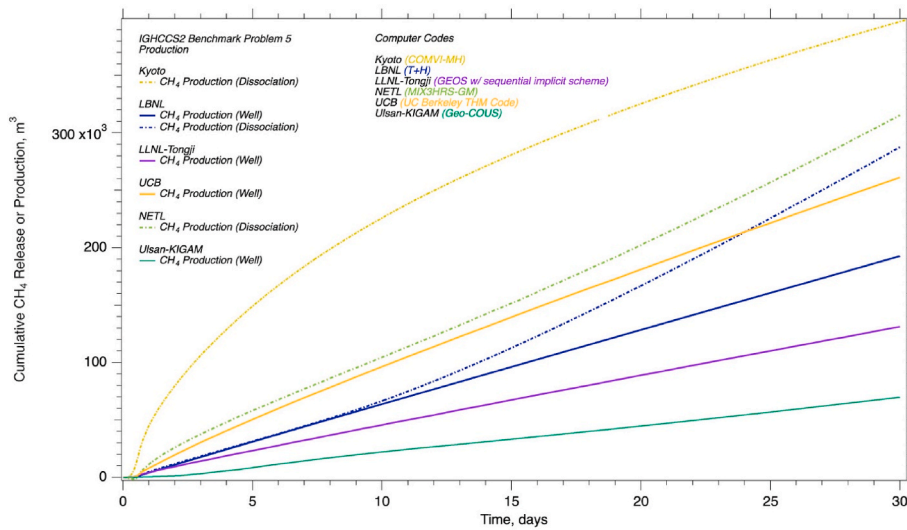


Fig. 48. BP5 (Nankai Trough) comparison of numerical simulations of cumulative methane released via dissociation or produced at the well versus time.

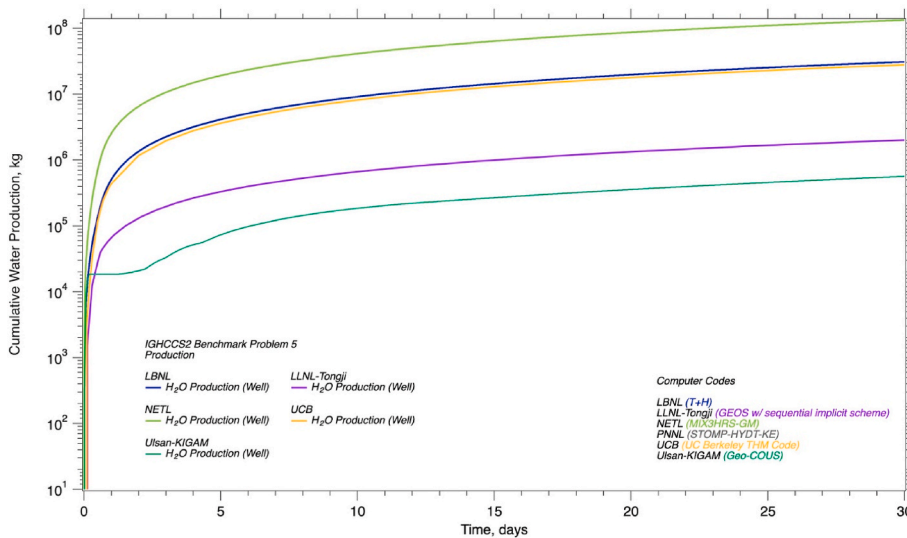


Fig. 49. BP5 (Nankai Trough) comparison of numerical simulations of cumulative water produced at the well versus time.

in Fig. 50. All simulations showed preferential hydrate dissociation along the top of the hydrate bearing layer, but the simulations from the Kyoto and UCB showed more gradual variations in hydrate saturation with depth and radial extent than the simulations from NETL, LLNL-Tongji and Ulsan-KIGAM. For these later simulations dissociation fronts were sharper in the radial direction and little to no hydrate dissociation occurred along the bottom of the hydrate-bearing layer. Hydrate saturation profiles from Ulsan-KIGAM additionally showed lensing with regions of variable hydrate saturation between the production front and production well. Radial profiles of temperature at the bottom, middle, and top of the hydrate-bearing layer at 30 days (Fig. 51), tend to agree with the hydrate saturation profiles, in that lower temperatures occur in regions with lower hydrate saturations, as would be expected during hydrate dissociation. The notable exception is the temperature profiles of the LLNL-Tongji simulation, which show higher temperatures near the center of the domain. Radial profiles of pressure within the hydrate-bearing layer at 30 days show reasonable comparisons among the simulations, as expected given that pressure is controlled at the inner and outer radial distances. Pressures lower in hydrate-bearing layer are generally higher (Fig. 52), also as expected

due to hydrostatics, the location of the production zone, and increased hydrate dissociation higher in the layer. The comparability of the pressure profiles, however, is in contrast to the produced water, which again suggests differences in the effective permeability and aqueous relative permeability calculations among the computer codes. Additional simulations were executed by Kyoto, which indicated improved agreement between the Kyoto results and others when the intrinsic permeability of the hydrate-bearing layer was lower by a factor of 100.

Production of methane from hydrate via depressurization reduces the strength of the hydrate-bearing layer due to the loss of hydrate and increases in effective stress from the pore pressure reduction. The combined processes cause deformation of the sediment layers. Deformations were reported as vertical displacements for three depths along the well: the sea floor, the top of the hydrate-bearing sediment (HBS), and bottom of the hydrate-bearing sediment, (Fig. 53). Overall, the simulations predict increasing vertical displacements over time, with smallest displacements occurring at the sea floor. In general, both the sea floor and the top of HBS settle downward, and the base of HBS (below the depressurization interval) shows uplift. This indicates compaction of the HBS reservoir. Three exceptions to this were: 1) the

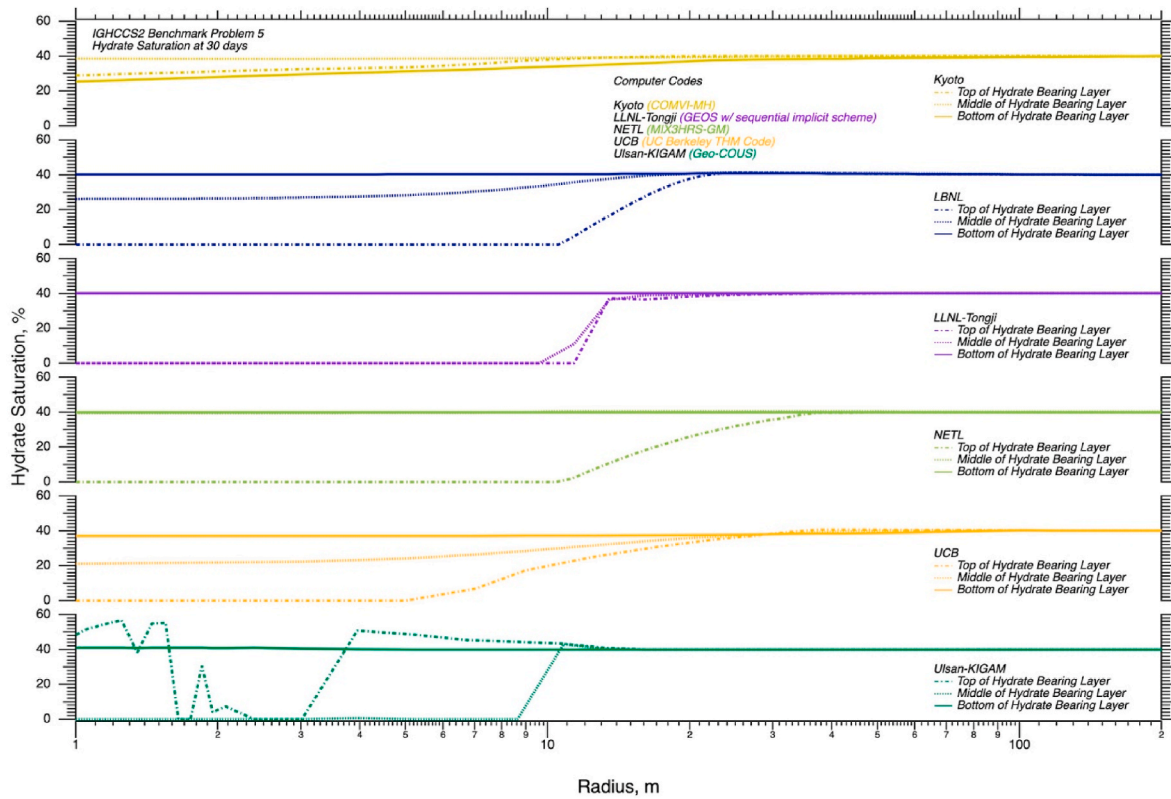


Fig. 50. BP5 (Nankai Trough) comparison of numerical simulations of hydrate saturation versus radial distance at the top, middle and bottom of the hydrate-bearing layer at 30 days.

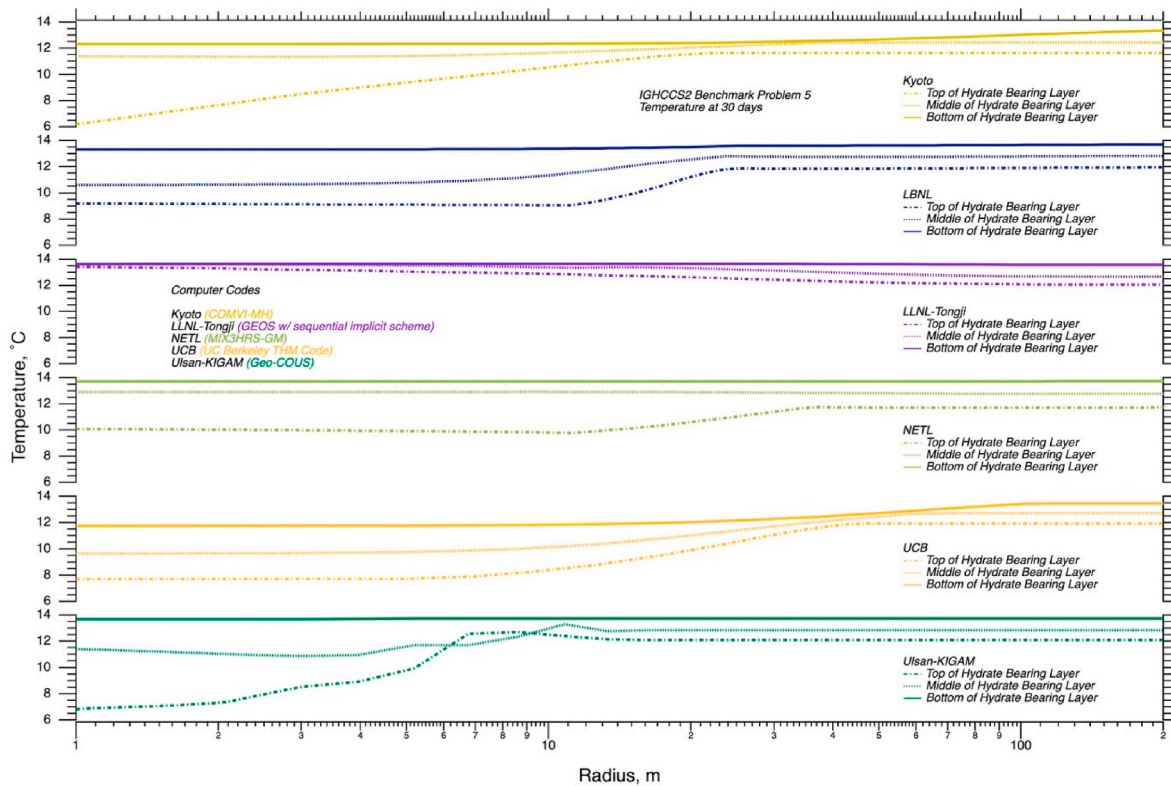


Fig. 51. BP5 (Nankai Trough) comparison of numerical simulations of temperature versus radial distance at the top, middle, and bottom of the hydrate-bearing layer at 30 days.

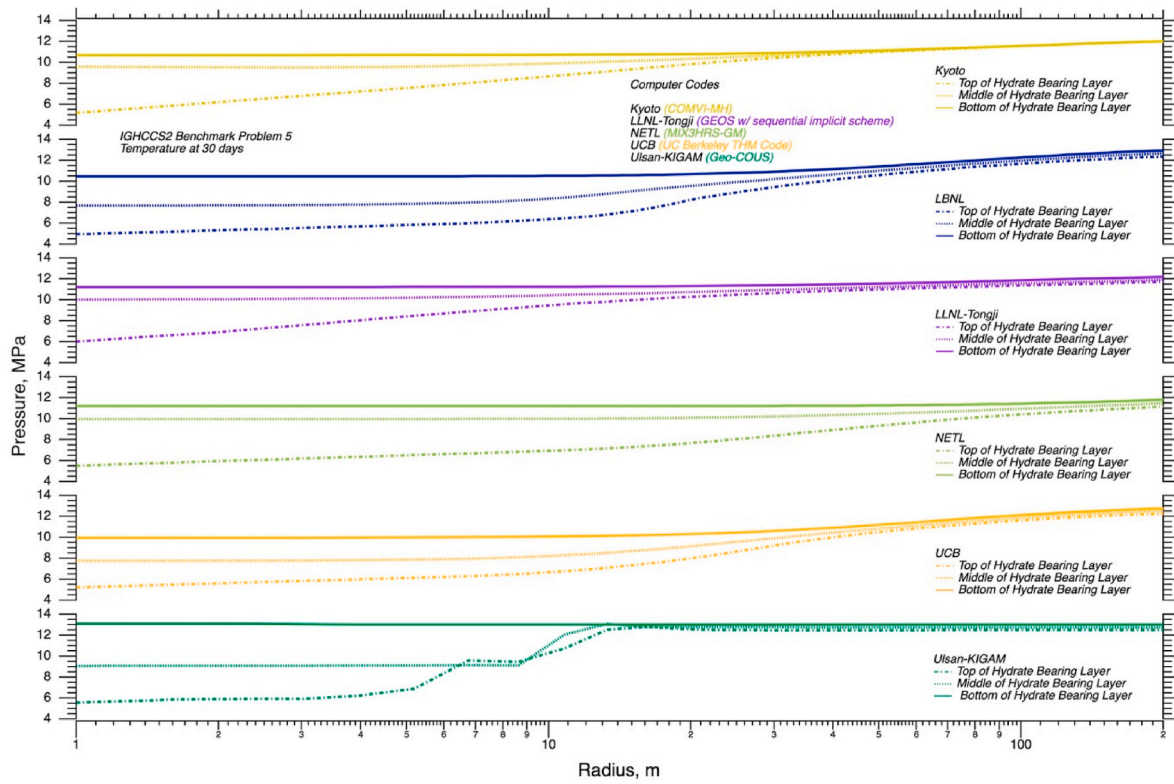


Fig. 52. BP5 (Nankai Trough) comparison of numerical simulations of pressure versus radial distance at the top, middle, and bottom of the hydrate-bearing layer at 30 days.

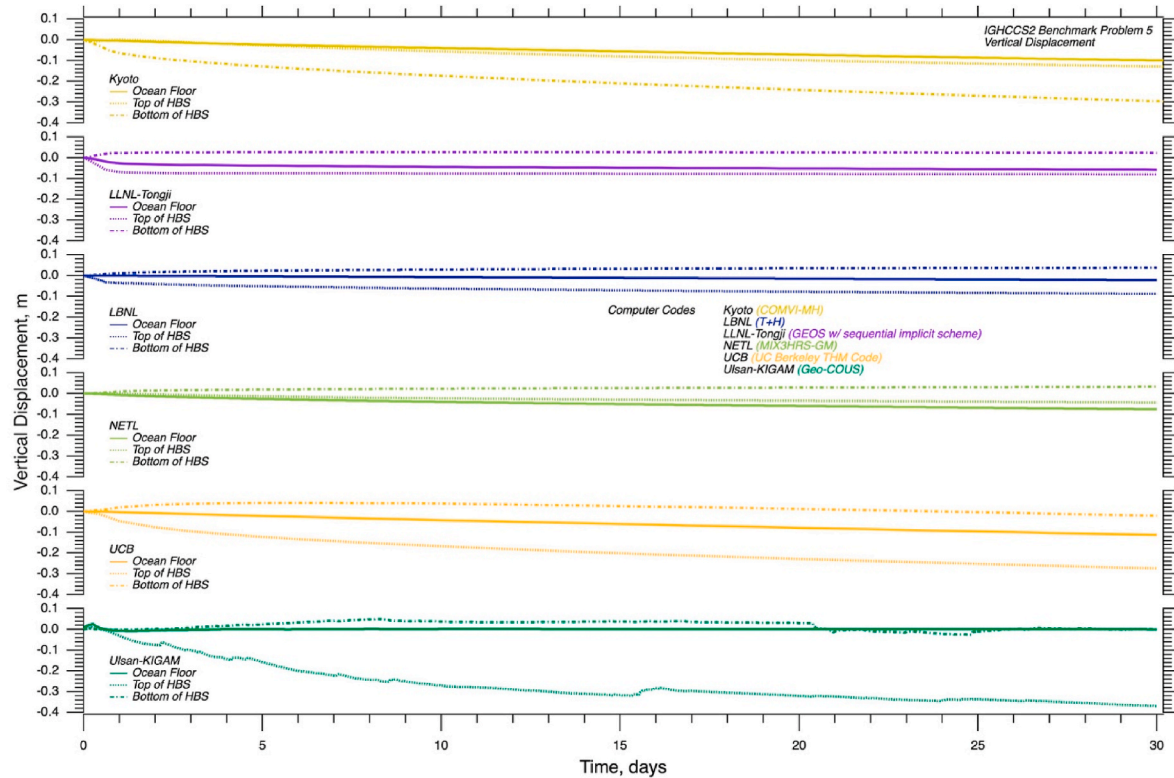


Fig. 53. BP5 (Nankai Trough) comparison of numerical simulations of vertical displacement at the ocean floor, top of the hydrate bearing sediment, and bottom of the hydrate bearing sediment at the well versus time. Teams using an elasto-viscoplastic modeling approach in their simulators were Kyoto, NETL, UCB, and Ulsan-KIGAM; and teams using an elastic modeling approach in their simulators were LLNL-Tongji, LBNL.

NETL simulation predicts the largest displacements occur at the sea floor; 2) the Ulsan-KIGAM simulation predicts the base of HBS oscillates between uplift and settlement over time; 3) the Kyoto simulation predicts settlement at all three depths, with the largest settlement at the base of HBS. Overall displacement levels were in agreement, in spite of differences in complexity of the geomechanical models, ranging from elastic to elasto-viscoplastic.

8.3. BP5 summary

BP5 was designed to model the response of the world's first production test attempt for marine gas hydrate deposits, which occurred in early 2013 in Eastern Nankai Trough, Japan (Yamamoto et al., 2017). During this six-day off-shore production test, using depressurization, 119,500 m³ (STP conditions) of methane gas were produced along with 1250 m³ of water. Maximum temperature changes observed in the production borehole and in a monitoring borehole, located 22 m away, were -5.0 and -0.6 °C, respectively. Sand production into the well forced production to terminate on the seventh day.

Although there are variations among the simulations, the production of gas calculated over the first six days are comparable to the field data (Yamamoto et al., 2017). The cumulative produced or released methane mass via dissociation after six days of pumping ranged from 11,500 to 167,260 m³ (STP) (Fig. 48), compared with the field value of 119,500 m³ (Yamamoto et al., 2017). The calculated production of water was significantly higher than that observed in the field data, and there was variation across the different simulations. It should be noted that the simulations assume that hydrates are homogeneously distributed in the hydrate-bearing layer with 40% hydrate saturation. In reality, hydrate-bearing layer 5 contains alternating silt and sand layers (Yamamoto et al., 2017).

9. Perspectives and future directions

As with petroleum reservoir simulators (Pedersen and Christensen, 2007), gas hydrate reservoir simulators (GHRS) have evolved over time in response to field and laboratory observations. At the time of the 2002 Mallik gas hydrate research program (Dallimore and Collett, 2005; Dallimore et al., 2005) GHRS were generally being applied to understand the coupled thermal-hydrologic responses of reservoirs for various classes of gas hydrate accumulations (Moridis et al., 2005; Moridis and Reagan, 2007a, b). The geomechanical response of a gas hydrate reservoir to depressurization was first addressed numerically for two known hydrate-bearing permafrost deposits: Mallik in the Northwest Territories of Canada, and Mount Elbert on the North Slope of Alaska, USA (Rutqvist et al., 2009). This numerical modeling capability was developed through the sequential coupling of the LBNL gas hydrate reservoir simulator TOUGH + HYDRATE (Moridis et al., 2005; Moridis and Reagan, 2007a, b) with FLAC3D, a commercial geomechanical code (Itasca, 2006). At about the same time, Kyoto University was developing fully coupled thermal-hydrologic-mechanical gas hydrate reservoir modeling capabilities to address depressurization in marine deposits (Kimoto et al., 2007). More recently, observation of sand production during depressurization and gas hydrate dissociation with the injection of nitrogen gas have spurred numerical simulation developments to allow modeling of these processes also. Each cycle of code developments in response to field or laboratory observations raises questions as to validity and accuracy of the updated GHRS.

IGHCCS2 specifically addresses the coupling of the thermal, thermodynamic, hydrologic, and geomechanical processes in GHRS, adding geomechanics to the coupled processes addressed in the IGHCCS1 (Anderson et al., 2011a, 2011b; Wilder et al., 2008). As with the IGHCCS1, differences between simulation results increased with increasing problem complexity, either geometric complexity or process model complexity. The greatest diversity of simulation results occurred with the Nankai Trough problem (BP5), which has a layered geology and

options for modeling the geomechanical system as either being elastic, plastic, or visco-plastic. It was interesting to note that produced water rather than produced methane yielded the greatest differences in simulation results for the Nankai Trough problem. In other problems there were good comparisons between produced water across the simulators and teams. User errors remain a strong possibility for the observed differences in simulation results because the codes are quite complicated, but there were also a variety modeling approaches adopted for the constitutive equations (i.e., equations used in the codes to complete the governing conservation equations). Overall, this study provides a basis for quantifying what levels of differences to expect in applying modern GHRS to production problems. IGHCCS2 has also succeeded in advancing capabilities, correcting code bugs, building an international scientific community of gas hydrate modelers, and leaving a legacy of challenging problems for the next generation of GHRS.

Several possible approaches for modeling the coupled thermo-hydro-geomechanical processes relevant to the evolution of gas hydrate-bearing systems were examined by the first and second IGHCCS. Considering the benchmark problems from both studies, certain conclusions can be drawn about the impact of different modeling approaches. In both studies, general-physics and built-for-purpose numerical simulators were applied. Except via simple empirical expressions, the general-physics simulators typically lack capabilities for modeling physical properties, such as density, viscosity, enthalpy, and solubility, yielding results that differ from those of the built-for-purpose simulators. Conversely, a fundamental understanding of the impacts of physical properties and underlying mathematics was more readily apparent in the general-physics simulators.

Hydrate dissociation and formation are modeled using either equilibrium or kinetic approaches, with some kinetic approaches allowing for nonequilibrium states between the mobile and immobile phases. A critical consequence of how simulators handle phase-change rates can be seen in the generation of hydrate lenses during production: equilibrium and fast kinetic models have the potential to create hydrate lensing through a feedback involving effective permeability reduction with increasing gas hydrate saturation.

Most of the GHRSs considered in IGHCCS2 added geomechanical capabilities only after the original development of the simulator. However, some simulators were built from the start to include geomechanical capabilities, and at least one code was principally a geomechanics computer code for which gas hydrate capabilities were added later. For codes that added geomechanics to an existing GHRS, sequential coupling was often used and commercial geomechanics capabilities were often also used. Geomechanical capabilities ranged from elastic, to elasto-plastic, to elasto-visco-plastic, with differences between these approaches becoming most apparent in BP5 (Nankai Trough). For codes that included geomechanics from the start, full coupling versus sequential coupling of the geomechanics and flow and transport processes was implemented. No significant differences in simulation results were noted between full coupling and sequential coupling of geomechanics and flow and transport, but execution times were not reported during this study.

Radial modeling capabilities for geomechanics, flow and transport offered clear advantages in modeling single-well problems. For those codes without radial modeling capabilities for both geomechanics and flow and transport, domains of a higher dimension were required to realize a solution. For example, BP4 (Radial Production with Geomechanics) was solved as a one-dimensional domain with radial capabilities, but as a two-dimensional domain without radial capabilities. For BP5 (Nankai Trough) radial capabilities allow a two-dimensional domain, but without this capability, a three dimensional domain is required. Increases in domain dimensionality directly increase time for execution.

Each of the benchmark problems of IGHCCS2 was designed to test certain aspects of modeling gas hydrate reservoirs, and each problem provided insights into the effect certain modeling approaches and

assumptions had on the predicted results. BP1 (Isotropic Consolidation with Hydrate Dissociation) eliminated computational domain effects through the use of a single grid cell, shifting the focus to the coupled thermal-hydraulic-geomechanical process. Whereas the coupling between geomechanical, flow and transport processes generally showed good agreement across the numerical simulators, BP1 demonstrates the importance of modeling effective permeability correctly to achieve good agreement with other simulators. BP2 (Extended Terzaghi Problem) was similar to BP1, but considered a multi-node domain, time varying boundary conditions, and mechanical properties that were dependent on gas hydrate saturation. Through the comparison of three controlling parameters extracted from a general-physics and two built-for-purpose computer codes, this problem demonstrates the importance of having all sub-models use computed key parameters, such as phase compressibility, hydrate surface area, and effective permeability. This problem emphasized the need to have correct expressions of the dependencies of constitutive equations to phase saturations, including phase pressures, phase relative permeabilities, and geomechanical properties to realize overall agreement in the more general simulation results.

BP3 (Gas Hydrate Dissociation in a One-Dimensional Radial Domain) was designed to be a link between the IGHCCS1 and 2 and to isolate differences in the non-geomechanical aspects of the computer codes. The similarity solution characteristic of this problem for both the thermal stimulation and depressurization cases is useful in identifying errors in the core formulation of flow and transport process in the simulators. In general, the different simulators showed consistent solutions in terms of the similitude variable, whether derived at one point in space over time, or one point in time over the domain space. This problem, however, has strong nonlinearities which must be resolved for achieving a solution. Moderate hydrate lensing occurred during this problem for some simulators.

BP4 (Radial Production with Geomechanics) was specifically developed to test a newly incorporated radial modeling capability for an existing and proven GHRS. Radial production capabilities reduced computational time for this problem, but other higher dimensional domains achieved accurate solutions. An analytical solution was available for the case without hydrate for this problem and the simulators showed good agreement with this solution, indicating proper modeling of hydrologic and geomechanical processes. The case with gas hydrate, however, yielded greater differences across the simulators and, for some simulators hydrate lensing halted the computation. Simulators with slower kinetics of hydrate dissociation and formation did not demonstrate gas hydrate lensing. The LBNL team is currently studying the differences between radial and Cartesian grids in relation to gas hydrate lensing.

BP5 (Nankai Trough) was developed as a simplified version of the published modeling completed on the depressurization gas hydrate production demonstration in the Nankai Trough. Whereas sand production played an important role in the actual field program, this process was not considered here, restricting the focus to coupled hydrologic, thermal, and geomechanical processes. This problem required either two- or three-dimensional domains, with vertical heterogeneity. The increased complexity of BP5 with respect to all aspects of modeling gas hydrate reservoirs yielded the greatest range of results among the five benchmark problems. This outcome is similar to that found during the IGHCCS1; where increased problem complexity equated to increased ranges in predicted results. Specifically, BP5 confirmed the BP2 and BP4 conclusions that how a GHRS handles the evolving effective (and relative) permeabilities exerts a dominant control on the predicted evolution of the reservoir.

10. Conclusions

IGHCCS2 brought together international experts to compare their numerical tools for providing best estimates of the geomechanical behavior of gas hydrate-bearing reservoirs. These tools were used to

evaluate simple and complex reservoir models whose behavior cannot be easily estimated or verified. Though these computer codes have become quite powerful in their predictive capabilities, the results of this study show that users must be aware that different approaches can provide different estimates of reservoir behavior. The users and developers in this study understand the functionality of their codes, the approximations, and the tradeoffs that must be accepted to attain the desired functionality. General users must also gain an appreciation for these code functionalities and be able to explain their results in terms of the strengths and weaknesses of the code being used. The study has yielded new collaborative research and publications between participants, and the benchmark problems have inspired experimental investigations based on the extended Terzaghi problem (i.e., BP2), and the isotropic consolidation with hydrate dissociation problem (i.e., BP1). While it is unlikely that any one model could be developed to effectively accommodate every aspect of a gas hydrate reservoir's long-term evolution, it is hoped this IGHCCS2 report provides the community with a set of insights and directions that help researchers develop and utilize models to more effectively and confidently address the specific needs of their work.

Although not part of this study, geophysics has shown us that many techniques can provide excellent results in the relative mode (comparing results from systems that differ only slightly, or from a single system for small changes in a given parameter) rather than in an absolute mode in which a "true" result is required for a novel situation. For example, X-ray computed tomography has been used to investigate gas hydrate dissociation in sediment cores collected from offshore India and onshore Alaska (Kneafsey and Moridis, 2014). Thus, where a single set of measurements may be very difficult to understand, comparing results measured before and after a stimulus may provide a better understanding of the system. Comparisons in this study are over drastic changes ($s_h = 0\%$, $s_h = 60\%$) so they do not meet the "small change" criteria. Because we are often unable to instantly cause such dramatic changes in natural systems at reservoir scales, it will be important to compare model results in a relative mode. It is possible that relative-mode differences between code results might be much smaller than the absolute-mode results in this study indicate, although future testing would be required to determine this. Any use of trade, firm or product name is for descriptive purposes only and does not imply endorsement by the U.S. Government.

Declaration of competing interest

The authors declare that they have no known competing financial interests or personal relationships that could have appeared to influence the work reported in this paper.

CRedit authorship contribution statement

M.D. White: Conceptualization, Software, Validation, Investigation, Data curation, Writing - original draft, Supervision. **T.J. Kneafsey:** Conceptualization, Investigation, Writing - original draft, Writing - review & editing, Supervision, Funding acquisition. **Y. Seol:** Conceptualization, Investigation, Resources, Writing - review & editing, Supervision, Project administration. **W.F. Waite:** Writing - original draft, Writing - review & editing. **S. Uchida:** Methodology, Investigation, Writing - original draft, Supervision. **J.S. Lin:** Conceptualization, Methodology, Software, Validation, Investigation. **E.M. Myshakin:** Methodology, Software, Validation, Investigation, Writing - review & editing. **X. Gai:** Software, Validation, Investigation, Writing - review & editing. **S. Gupta:** Conceptualization, Methodology, Software, Validation, Formal analysis, Investigation, Writing - original draft, Writing - review & editing, Visualization. **M.T. Reagan:** Conceptualization, Methodology, Software, Validation, Formal analysis, Investigation, Writing - original draft, Writing - review & editing, Visualization. **A.F. Queiruga:** Conceptualization, Methodology, Software, Validation,

Formal analysis, Investigation, Writing - original draft, Writing - review & editing, Visualization. **S. Kimoto:** Conceptualization, Methodology, Software, Validation, Investigation, Writing - original draft, Writing - review & editing, Visualization. **R.C. Baker:** Software, Validation, Investigation.

Acknowledgements

This material is based upon work supported by the U.S. Department of Energy, Office of Fossil Energy, Office of Natural Gas and Petroleum Technology, through the National Energy Technology Laboratory, under Award Number DE-AC02-05CH11231. Waite and Collett received support from U.S. Geological Survey's (USGS's) Coastal/Marine Hazards and Resources Program and Energy Resources Program. We also acknowledge the leadership and vision of the principal investigators, Dr. Joseph W. Wilder (University of Akron) and Dr. Brian J. Anderson (National Energy Technology Laboratory) of the 1st International Gas Hydrate Code Comparison Study, who guidance and excellence set the standards for this study.

References

- Akaki, T., Kimoto, S., Oka, F., 2016. Chemo-thermo-mechanically coupled seismic analysis of methane hydrate-bearing sediments during a predicted Nankai Trough Earthquake. *Int J Numer Anal Met* 40, 2207–2237.
- Anderson, B., Hancock, S., Wilson, S., Enger, C., Collett, T., Boswell, R., Hunter, R., 2011a. Formation pressure testing at the Mount Elbert gas hydrate stratigraphic test well, Alaska North Slope: operational summary, history matching, and interpretations. *Mar. Petrol. Geol.* 28, 478–492. <https://doi.org/10.1016/j.marpetgeo.2009.12.001>.
- Anderson, B.J., Kurihara, M., White, M.D., Moridis, G.J., Wilson, S.J., Pooladi-Darvish, M., Gaddipati, M., Masuda, Y., Collett, T.S., Hunter, R.B., Narita, H., Rose, K., Boswell, R., 2011b. Regional long-term production modeling from a single well test, Mount Elbert gas hydrate stratigraphic test well, Alaska North Slope. *Mar. Petrol. Geol.* 28, 493–501.
- Aziz, K., Settari, A., 1979. *Petroleum Reservoir Simulation*. Applied Science Publishers.
- Bishop, A.W., 1959. The principle of effective stress. *Tecnisk Ukeblad* 106, 859–863.
- Boswell, R., Collett, T.S., 2011. Current perspectives on gas hydrate resources. *Energy Environ. Sci.* 4, 1206–1215. <https://doi.org/10.1039/C0EE00203H>.
- Boswell, R., Collett, T.S., Frye, M., Shedd, W., McConnell, D.R., Shelander, D., 2012. Subsurface gas hydrates in the northern Gulf of Mexico. *Mar. Petrol. Geol.* 34, 4–30. <https://doi.org/10.1016/j.marpetgeo.2011.10.1003>.
- Boswell, R., Myshakin, E., Moridis, G., Konno, Y., Collett, T.S., Reagan, M., Ajayi, T., Seol, Y., 2019. India National Gas Hydrate Program Expedition 02 summary of scientific results: numerical simulation of reservoir response to depressurization. *Mar. Petrol. Geol.* <https://doi.org/10.1016/j.marpetgeo.2018.10.099>.
- Boswell, R., Schoderbek, D., Collett, T.S., Ohtsuki, S., White, M., Anderson, B.J., 2017. The ignik sikumi field experiment, Alaska North Slope: design, operations, and implications for CO₂-CH₄ Exchange in gas hydrate reservoirs. *Energy Fuels* 31, 140–153.
- Boswell, R., Yamamoto, K., Lee, S.-R., Collett, T., Kumar, P., Dallimore, S., 2014. Chapter 8 - methane hydrates. In: Letcher, T.M. (Ed.), *Future Energy*, second ed. Elsevier, Boston, pp. 159–178. <https://doi.org/10.1016/B978-0-08-099424-6.00008-9>.
- Briaud, J.L., Chaouch, A., 1997. Hydrate melting in soil around hot conductor. *J. Geotech. Geoenviron. Eng.* 123, 645–653. [https://doi.org/10.1061/\(ASCE\)1090-0241\(1997\)123:7\(645\)](https://doi.org/10.1061/(ASCE)1090-0241(1997)123:7(645)).
- Brooks, R.H., Corey, A.T., 1964. *Hydraulic Properties of Porous Media*, Hydrology Papers. Colorado State University, Hydrology Papers, p. 24.
- Cao, S.C., Jang, J.B., Jung, J.W., Waite, W.F., Collett, T.S., Kumar, P., 2019. 2D micromodel study of clogging behavior of fine-grained particles associated with gas hydrate production in NGHP-02 gas hydrate reservoir sediments. *Mar. Petrol. Geol.* 108, 714–730.
- Carman, P.C., 1937. Fluid flow through granular beds. *Transactions - Institute of Chemical Engineers* 15, 150–166.
- Civan, F., 2004. Scale Effect on Porosity and Permeability: Kinetics, Model and Correlation. *American Institute of Chemical Engineers Journal*, pp. 271–287.
- Dallimore, S.R., Collett, T.S., 2005. Summary and implications of the Mallik 2002 gas hydrate production research well program. In: Dallimore, S.R., Collett, T.S. (Eds.), *Scientific Results from the Mallik 2002 Gas Hydrate Production Research Well Program*, Mackenzie Delta, Northwest Territories, Canada, vol. 585. Geological Survey of Canada, Bulletin, pp. 1–36.
- Dallimore, S.R., Collett, T.S., Taylor, A.E., Uchida, T., Weber, M., Chandra, A., Mroz, T. H., Caddel, E.M., Inoue, T., 2005. Scientific results from the Mallik 2002 gas hydrate production research well program, Mackenzie Delta, northwest territories, Canada: Preface. *Bulletin of the Geological Survey of Canada*.
- Dallimore, S.R., Yamamoto, K., Wright, J.F., Bellefleur, G., 2012. Proof of concept for gas hydrate production using the depressurization technique, as established by the JOGMEC/NRCan/Aurora Mallik 2007–2008 Gas Hydrate Production Research Well Program. *Geol. Surv. Can. Bull.* 601, 1–15.
- Davies, J.P., Davies, D.K., 1999. Stress-dependent permeability: characterization and modeling. In: *SPE Annual Technical Conference and Exhibition*. Society of Petroleum Engineers, pp. 1–15.
- Deepak, M., Kumar, P., Singh, K., Yadav, U.S., 2019. Techno-economic forecasting of a hypothetical gas hydrate field in the offshore of India. *Mar. Petrol. Geol.* 108, 741–746.
- Doughty, C.A., Pruess, K., 1992. A similarity solution for two-phase water, air and heat flow near a linear heat source in a porous medium. *J. Geophys. Res.* 1821–1838.
- Flemings, P.B., Boswell, R., Collett, T.S., Cook, A.E., Divins, D., Frye, M., Guerin, G., Goldberg, D.S., Malinverno, A., Meazell, K., Morrison, J., Pettigrew, T., Phillips, S.C., Santra, M., Sawyer, D.E., Shedd, W., Thomas, C., You, K., 2017. GOM2: prospecting, drilling and sampling coarse-grained hydrate reservoirs in the deepwater Gulf of Mexico. In: *Proceedings of the 9th International Conference on Gas Hydrates (ICGH 9)*, Denver, CO, USA, June 25–30, 2017.
- Fujii, T., Suzuki, K., Takayama, T., Tamaki, M., Komatsu, Y., Konno, Y., Yoneda, J., Yamamoto, K., Nagao, J., 2015. Geological setting and characterization of a methane hydrate reservoir distributed at the first offshore production test site on the Daini-Atsumi Knoll in the eastern Nankai Trough, Japan. *Mar. Petrol. Geol.* 66, 310–322. <https://doi.org/10.1016/j.marpetgeo.2015.02.037>.
- Gupta, S., Helmig, R., Wohlmuth, B., 2015. Non-isothermal, multi-phase, multi-component flows through deformable methane hydrate reservoirs. *Comput. Geosci.* 19, 1063–1088.
- Gupta, S., Wohlmuth, B., Helmig, R., 2016. Multi-rate time stepping schemes for hydro-geomechanical model for subsurface methane hydrate reservoirs. *Adv. Water Resour.* 91, 78–87.
- Hadley, C., Peters, D., Vaughan, A., Bean, D., 2008. Gumusut-Kakap Project: Geohazard Characterisation and Impact on Field Development Plans (IPTC 12554), International Petroleum Technology Conference. Kuala Lumpur, Malaysia, p. 15. <https://doi.org/10.2523/IPTC-12554-MS>.
- Hancock, S., Boswell, R., Collett, T., 2019. Development of deepwater natural gas hydrates. In: *Offshore Technology Conference*, Houston, Texas, May 6–9, Paper OTC-29374-MS.
- Handa, Y.P., 1986. Compositions, enthalpies of dissociation, and heat capacities in the range 85 to 270 K for clathrate hydrates of methane, ethane, and propane, and enthalpy of dissociation of isobutane hydrate, as determined by a heat-flow calorimeter. *J. Chem. Thermodyn.* 18, 915–921. [https://doi.org/10.1016/0021-9614\(1986\)90149-9](https://doi.org/10.1016/0021-9614(1986)90149-9).
- Itasca, 2006. *FLAC3D Version 3.1-User's Guide*, third ed. Itasca Consulting Group, Inc., Minneapolis, MN, USA.
- Jang, J.B., Waite, W.F., Stern, L.A., Collett, T.S., Kumar, P., 2019. Physical property characteristics of gas hydrate-bearing reservoir and associated seal sediments collected during NGHP-02 in the Krishna-Godavari Basin, in the offshore of India. *Mar. Petrol. Geol.* 108, 249–271.
- Ju, X., Liu, F., Fu, P.C., White, M.D., Settigast, R.R., Morris, J.P., 2020. Gas production from hot water circulation through hydraulic fractures in methane hydrate-bearing sediments: THC-coupled simulation of production mechanisms. *Energy Fuels* 34, 4448–4465.
- Jung, J.W., Jang, J., Santamarina, J.C., Tsouris, C., Phelps, T.J., Rawn, C.J., 2012. Gas production from hydrate-bearing sediments: the role of fine particles. *Energy Fuels* 26, 480–487.
- Kim, H.C., Bishnoi, P.R., Heidemann, R.A., Rizvi, S.S.H., 1987. Kinetics of methane hydrate decomposition. *Chem. Eng. Sci.* 42, 1645–1653.
- Kimoto, S., Oka, F., Fushita, T., 2010. A chemo-thermo-mechanically coupled analysis of ground deformation induced by gas hydrate dissociation. *Int. J. Mech. Sci.* 52, 365–376.
- Kimoto, S., Oka, F., Fushita, T., Fujiwaki, M., 2007. A chemo-thermo-mechanically coupled numerical simulation of the subsurface ground deformations due to methane hydrate dissociation. *Comput. Geotech.* 34, 216–228.
- Kneafsey, T.J., Moridis, G.J., 2014. X-Ray computed tomography examination and comparison of gas hydrate dissociation in NGHP-01 expedition (India) and Mount Elbert (Alaska) sediment cores: experimental observations and numerical modeling. *Mar. Petrol. Geol.* 58, 526–539.
- Konno, Y., Fujii, T., Sato, A., Akamine, K., Naiki, M., Masuda, Y., Yamamoto, K., Nagao, J., 2017. Key findings of the world's first offshore methane hydrate production test off the coast of Japan: toward future commercial production. *Energy Fuels* 31, 2607–2616.
- Konno, Y., Kato, A., Yoneda, J., Oshima, M., Kida, M., Jin, Y., Nagao, J., Tenma, N., 2019. Numerical analysis of gas production potential from a gas-hydrate reservoir at Site NGHP-02-16, the Krishna-Godavari Basin, offshore India-Feasibility of depressurization method for ultra-deepwater environment. *Mar. Petrol. Geol.* <https://doi.org/10.1016/j.marpetgeo.2018.10.008>.
- Kozeny, J., 1927. Über kapillare leitung des wassers in boden. *Sitzungsber. Akad. Wiss. Wien* 136, 271–306.
- Kurihara, M., Sato, A., Funatsu, K., Ouchi, H., Masuda, Y., Narita, H., Collett, T.S., 2011. Analysis of formation pressure test results in the Mount Elbert methane hydrate reservoir through numerical simulation. *Mar. Petrol. Geol.* 28, 502–516. <https://doi.org/10.1016/j.marpetgeo.2010.10.1007>.
- Kvenvolden, K.A., 1993. Gas Hydrates - geological perspective and global change. *Rev. Geophys.* 31, 173–187. <https://doi.org/10.1029/1093RG00268>.
- Lafond, P.G., Olcott, K.A., Sloan, E.D., Koh, C.A., Sum, A.K., 2012. Measurements of methane hydrate equilibrium in systems inhibited with NaCl and methanol. *J. Chem. Thermodyn.* 48, 1–6.
- Lei, L., Seol, Y., Jarvis, K., 2018. Pore-scale visualization of methane hydrate-bearing sediments with micro-CT. *Geophys. Res. Lett.* 45, 5417–5426.
- Li, J.-f., Ye, J.-l., Qin, X.-w., Qiu, H.-j., Wu, N.-y., Lu, H.-l., Xie, W.-w., Lu, J.-a., Peng, F., Xu, Z.-q., Lu, C., Kuang, Z.-g., Wei, J.-g., Liang, Q.-y., Lu, H.-f., Kou, B.-b., 2018. The

- first offshore natural gas hydrate production test in South China Sea. *China Geology* 1, 5–16. <https://doi.org/10.31035/cg2018003>.
- Li, X.-S., Xu, C.-G., Zhang, Y., Ruan, X.-K., Li, G., Wang, Y., 2016. Investigation into gas production from natural gas hydrate: a review. *Appl. Energy* 172, 286–322. <https://doi.org/10.1016/j.apenergy.2016.1003.1101>.
- Masuda, Y., Naganawa, S., Ando, S., Sato, K., 1997. Numerical Calculation of Gas Production Performance from Reservoirs Containing Natural Gas Hydrates. SPE Annual Technical Conference, San Antonio, TX, USA.
- Max, M.D., Johnson, A.H., 2019. Energy Overview: Energy Options and Prospects for Natural Gas, Exploration and Production of Oceanic Natural Gas Hydrate: Critical Factors for Commercialization. Springer International Publishing, Switzerland, pp. 1–55.
- Moridis, G.J., Kowalsky, M.B., Pruess, K., 2005. Depressurization-induced gas production from class-1 hydrate deposits. *SPE-97266-PA* 10, 458–481.
- Moridis, G.J., Reagan, M.T., 2007a. Gas Production from Oceanic Class 2 Hydrate Accumulations. Offshore Technology Conference. SPE, Houston, TX, USA.
- Moridis, G.J., Reagan, M.T., 2007b. Strategies for Gas Production from Oceanic Class 3 Hydrate Accumulations. Offshore Technology Conference. SPE, Houston, TX, USA.
- Moridis, G.J., Reagan, M.T., Kim, S.-J., Seol, Y., Zhang, K., 2009. Evaluation of the gas production potential of marine hydrate deposits in the ulleung basin of the Korean east sea. *SPE-110859-PA* 14, 759–781.
- Moridis, G.J., Reagan, M.T., Queiruga, A.F., Kim, S.-J., 2019. System response to gas production from a heterogeneous hydrate accumulation at the UBGH2-6 site of the Ulleung basin in the Korean East Sea. *J. Petrol. Sci. Eng.* 178, 655–665. <https://doi.org/10.1016/j.petrol.2019.1003.1058>.
- Moridis, G.J., Queiruga, A.F., Reagan, M.T., 2019b. “Simulation of Gas Production from Multilayered Hydrate Bearing Media with Fully Coupled Flow, Thermal, Chemical and Geomechanical Processes using TOUGH+Millstone: Part 1: Numerical Modeling of Hydrates.” *Transport in Porous Media*, <https://doi.org/10.1007/s11242-019-01254-6>.
- Myshakin, E.M., Seol, Y., Lin, J.S., Uchida, S., Collett, T.S., Boswell, R., 2019. Numerical Simulations of Depressurization-Induced Gas Production from an Interbedded Turbidite Gas-Hydrate-Bearing Sedimentary Section in the Offshore of India: Site NGHP-02-16 (Area-B). *Marine and Petroleum Geology*. <https://doi.org/10.1016/j.marpetgeo.2018.10.047>.
- O’Sullivan, M.J., 1981. A similarity method for geothermal well test analysis. *Water Resour. Res.* 17, 390–398.
- Oyama, H., Abe, S., Yoshida, T., Sato, T., Nagao, J., Tenma, N., Narita, H., 2016. Experimental study of mud erosion at the interface of an artificial sand-mud alternate layer. *J. Nat. Gas Sci. Eng.* 34, 1106–1114. <https://doi.org/10.1016/j.jngse.2016.1107.1067>.
- Pedersen, K.S., Christensen, P.L., 2007. *Phase Behavior of Petroleum Reservoir Fluids*. CRC Press, Boca Raton, FL, USA.
- Queiruga, A.F., Moridis, G.J., Reagan, M.T., 2019. Simulation of Gas Production from Multilayered Hydrate Bearing Media with Fully Coupled Flow, Thermal, Chemical and Geomechanical Processes using TOUGH+Millstone: Part 2: Geomechanical Formulation and Numerical Coupling. *Transport in Porous Media*. <https://doi.org/10.1007/s11242-019-01242-w>.
- Rudnicki, J.W., 1986. Fluid mass sources and point forces in linear elastic diffusive solids. *Mech. Mater.* 5, 383–393.
- Ruppel, C., Kessler, J.D., 2017. The interaction of climate change and methane hydrates. *Rev. Geophys.* 55 <https://doi.org/10.1002/2016RG000534>.
- Rutqvist, J., Moridis, G.J., Grover, T., Collett, T., 2009. Geomechanical response of permafrost-associated hydrate deposits to depressurization-induced gas production. *J. Petrol. Sci. Eng.* 67, 1–12.
- Ryu, B.-J., Collett, T.S., Riedel, M., Kim, G.Y., Chun, J.-H., Bahk, J.-J., Lee, J.Y., Kim, J.-H., Yoo, D.-G., 2013. Scientific results of the second gas hydrate drilling expedition in the ulleung basin (UBGH2). *Mar. Petrol. Geol.* 47, 1–20. <https://doi.org/10.1016/j.marpetgeo.2013.1007.1007>.
- Settgast, R.R., Fu, P.C., Walsh, S.D.C., White, J.A., Annavarapu, C., Ryerson, F.J., 2017. A fully coupled method for massively parallel simulation of hydraulically driven fractures in 3-dimensions. *Int J Numer Anal Met* 41, 627–653.
- Sloan, E.D., Koh, C.A., 2007. *Clathrate Hydrates of Natural Gases*, third ed. CRC Press, Boca Raton.
- Stone, H.L., 1970. Probability model for estimating 3-phase relative permeability. *J. Petrol. Technol.* 22, 214–218.
- Terzaghi, K., 1943. *Theoretical Soil Mechanics*. John Wiley & Sons.
- Uchida, S., Lin, J.S., Myshakin, E.M., Seol, Y., Boswell, R., 2019. Numerical simulations of sand migration during gas production in hydrate-bearing sands interbedded with thin mud layers at site NGHP-02-16. *Mar. Petrol. Geol.* 108, 639–647.
- Uchida, S., Soga, K., Yamamoto, K., 2012. Critical state soil constitutive model for methane hydrate soil. *J Geophys Res-Sol Ea* 117, B03209.
- Valdes, J.R., Santamarina, J.C., 2007. Particle transport in a nonuniform flow field: retardation and clogging. *Appl. Phys. Lett.* 90, 244101. <https://doi.org/10.1063/1061.2748850>.
- van Genuchten, M.T., 1980. A closed-form equation for predicting the hydraulic conductivity of unsaturated soils. *Soil Sci. Soc. Am. J.* 44, 892–898. <https://doi.org/10.2136/sssaj1980.03615995004400050002x>.
- Verruijt, A., 2013. *Theory and Problems of Poroelasticity*. Delft University of Technology, Delft, Netherlands.
- Waite, W.F., Ruppel, C.D., Collett, T.S., Schultheiss, P., Holland, M., Shukla, K.M., Kumar, P., 2019. Multi-measurement approach for establishing the base of gas hydrate occurrence in the Krishna-Godavari Basin for sites cored during expedition NGHP-02 in the offshore of India. *Mar. Petrol. Geol.* 108, 296–320.
- Walsh, M.R., Hancock, S.H., Wilson, S.J., Patil, S.L., Moridis, G.J., Boswell, R., Collett, T.S., Koh, C.A., Sloan, E.D., 2009. Preliminary report on the commercial viability of gas production from natural gas hydrates. *Energy Econ.* 815–823. <https://doi.org/10.1016/j.eneco.2009.1003.1006>.
- Wang, H.F., 2000. *Theory of Linear Poroelasticity*. Princeton University Press, Princeton, NJ, USA.
- Wilder, J.W., Moridis, G.J., Wilson, S.J., Kurihara, M., White, M.D., Masuda, Y., Anderson, B.J., Collett, T.S., Hunter, R.B., Narita, H., Pooladi-Darvish, M., Rose, K., Boswell, R., 2008. An international effort to compare gas hydrate reservoir simulators. In: Englezos, P., Ripmeester, J. (Eds.), *Proceedings of the 6th International Conference on Gas Hydrates*, Vancouver, Canada, p. 12. Paper 5727.
- Wilson, S.J., Hunter, R.B., Collett, T.S., Hancock, S., Boswell, R., Anderson, B.J., 2011. Alaska North Slope regional gas hydrate production modeling forecasts. *Mar. Petrol. Geol.* 28, 460–477. <https://doi.org/10.1016/j.marpetgeo.2010.1003.1007>.
- Yamamoto, K., Kanno, T., Wang, X.X., Tamaki, M., Fujii, T., Chee, S.S., Wang, X.W., Pimenov, V., Shako, V., 2017. Thermal responses of a gas hydrate-bearing sediment to a depressurization operation. *RSC Adv.* 7, 5554–5577.
- Yamamoto, K., Suzuki, K., Wang, X., Matsunaga, T., Nishioka, I., Nakatsuka, Y., Yoneda, J., 2019. The second offshore production test of methane hydrates in the eastern Nankai Trough and site characterization efforts. Fire in the ice: department of energy, Office of Fossil energy, national energy Technology laboratory. *Methane Hydrate News Letter* 19 (1), 9–15.
- Yamamoto, K., Terao, Y., Fujii, T., Terumichi, I., Seki, M., Matsuzama, M., Kanno, T., 2014. Operational overview of the first offshore production test of methane hydrates in the Eastern Nankai Trough. In: Engineers, S.o.P. (Ed.), *Offshore Technology Conference*, May 5–8, 2014, Houston, TX, USA.
- Yoneda, J., Oshima, M., Kida, M., Kato, A., Konno, Y., Jin, Y., Jang, J.B., Waite, W.F., Kumar, P., Tenma, N., 2019a. Permeability variation and anisotropy of gas hydrate-bearing pressure-core sediments recovered from the Krishna-Godavari Basin, offshore India. *Mar. Petrol. Geol.* 108, 524–536.
- Yoneda, J., Oshima, M., Kida, M., Kato, A., Konno, Y., Jin, Y., Tenma, N., 2019b. Consolidation and hardening behavior of hydrate-bearing pressure-core sediments recovered from the Krishna-Godavari Basin, offshore India. *Mar. Petrol. Geol.* 108, 512–523.